Landslide size matters: a new spatial predictive paradigm

Luigi Lombardo[1*], Hakan Tanyas[1,2,3], Raphaël Huser[4], Fausto Guzzetti[5,6], Daniela Castro-Camilo[7]

Abstract

The standard definition of landslide hazard requires the estimation of where, when (or how frequently) and how large a given landslide event may be. The geomorphological community involved in statistical models has addressed the component pertaining to how large a landslide event may be by introducing the concept of landslide-event magnitude scale. This scale, which depends on the planimetric area of the given population of landslides, in analogy to the earthquake magnitude, has been expressed with a single value per landslide event. As a result, the geographic or spatially-distributed estimation of how large a population of landslide may be when considered at the slope scale, has been disregarded in statistically-based landslide hazard studies. Conversely, the estimation of the landslide extent has been commonly part of physically-based applications, though their implementation is often limited to very small regions.

In this work, we initially present a review of methods developed for landslide hazard assessment since its first conception decades ago. Subsequently, we introduce for the first time a statistically-based model able to estimate the planimetric area of landslides aggregated per slope units. More specifically, we implemented a Bayesian version of a Generalized Additive Model where the maximum landslide sizes per slope unit and the sum of all landslide sizes per slope unit are predicted via a Log-Gaussian model. These "max" and "sum" models capture the spatial distribution of landslide sizes. We tested these models on a global dataset expressing the distribution of co-seismic landslides due to 24 earthquakes across the globe. The two models we present are both evaluated on a suite of performance diagnostics that suggest our models suitably predict the aggregated landslide extent per slope unit. In addition to a complex procedure involving variable selection and a spatial uncertainty estimation, we built our model over slopes where landslides triggered in response to seismic

[1]University of Twente, Faculty of Geo-Information Science and Earth Observation (ITC), PO Box 217, Enschede, AE 7500, Netherlands

[2]Hydrological Sciences Laboratory, NASA Goddard Space Flight Center, Greenbelt, MD, United States

[3]USRA, Universities Space Research Association, Columbia, MD, United States

[4]King Abdullah University of Science and Technology (KAUST), Computer, Electrical and Mathematical Sciences and Engineering (CEMSE) Division, Thuwal 23955-6900, Saudi Arabia

[5]Consiglio Nazionale delle Ricerche (CNR), Istituto di Ricerca per la Protezione Idrogeologica (IRPI), via Madonna Alta 126, 06128 Perugia, Italy

[6]Presidenza del Consiglio dei Ministri, Dipartimento della Protezione Civile, via Vitorchiano 2, 00189 Roma, Italy

[7]School of Mathematics and Statistics, University of Glasgow, Glasgow, G12 8QQ, UK

shaking, and simulated the expected failing surface over slopes where the landslides did not occur in the past.

What we achieved is the first statistically-based model in the literature able to provide information about the extent of the failed surface across a given landscape. This information is vital in landslide hazard studies and should be combined with the estimation of landslide occurrence locations. This could ensure that governmental and territorial agencies have a complete probabilistic overview of how a population of landslides could behave in response to a specific trigger. The predictive models we present are currently valid only for the 24 cases we tested. Statistically estimating landslide extents is still at its infancy stage. Many more applications should be successfully validated before considering such models in an operational way. For instance, the validity of our models should still be verified at the regional or catchment scale, as much as it needs to be tested for different landslide types and triggers. However, we envision that this new spatial predictive paradigm could be a breakthrough in the literature and, in time, could even become part of official landslide risk assessment protocols.

Keywords: Integrated nested Laplace approximation (INLA); Landslide Hazard; Earthquake; Landslide Area Prediction; Slope unit partition; Bayesian spatial modelling;

Contents

1 Introduction

Landslides are common in the mountains, in the hills, and along high costs, where they can pose serious threats to the population, public and private properties, and the economy (Brabb and Harrod, 1989; Brabb, 1991; Kennedy et al., 2015; Nadim et al., 2006; Kirschbaum et al., 2010; Petley, 2012; Daniell et al., 2017; Broeckx et al., 2019). To cope with the landslide problem (Brabb, 1991; Nadim et al., 2006), and in an attempt to mitigate the landslide damaging effects through proper land planning (Kockelman, 1986; Brabb and Harrod, 1989; Guzzetti et al., 2000; Glade et al., 2005), investigators have long attempted to map landslides (Guzzetti et al., 2012), to quantify landslide susceptibility (Reichenbach et al., 2018), intensity (Lombardo et al., 2018b, 2019b, 2020a), and hazard (Varnes and the IAEG Commission on Landslides and Other Mass-Movements, 1984; Guzzetti et al., 1999, 2005a; Brenning, 2005; Fell et al., 2008; Lari et al., 2014), to evaluate the vulnerability to landslides of various elements at risk (Fuchs et al., 2007; Galli and Guzzetti, 2007; van Westen et al., 2008), including the population (Fell and Harford, 1997; Guzzetti, 2000; Dowling and Santi, 2014; Pereira et al., 2017; Salvati et al., 2018), and to ascertain landslide risk, qualitatively (Fell and Harford, 1997; Guzzetti et al., 2005b; Reichenbach et al., 2005; Fell and Harford, 1997; Glade et al., 2005) or quantitatively (Cruden and Fell, 1997a,b; Guzzetti, 2000; Salvati et al., 2010; Rossi et al., 2019).

A problem with many of these attempts has always been the inability (or at least the difficulty) to measure and predict the size—*i.e.*, depth, length, width, area, volume, and their multiple ratios and dependencies (Dai and Lee, 2001; Malamud et al., 2004b; Brunetti et al., 2009a; Guzzetti et al., 2009; Taylor et al., 2018a)—of the landslides, which are known to measure, control, or influence landslide magnitude (Keefer, 1984; Cardinali et al., 2002; Reichenbach et al., 2005; Fuchs et al., 2007), impact (Guzzetti et al., 2003; Lombardo et al., 2018a), and destructiveness (Fell and Harford, 1997; Cardinali et al., 2002; Guzzetti et al., 2005b; Reichenbach et al., 2005), which in turns depend on the landslide types (Hungr et al., 2014).

In this work, we propose an innovative approach to build statistical models capable of predicting the planimetric area of event-triggered landslides (Stark and Hovius, 2001; Malamud et al., 2004b; Guzzetti et al., 2012). To test the approach, we construct and validate two models that predict metrics related to the planimetric area of earthquake-induced landslides (EQILs) (Keefer, 1984, 2000, 2002, 2013). For the purpose, we exploit the information on the geographical location and planimetric area of 319,086 landslides shown in 25 EQIL inventories available from the global database collated by Schmitt et al. (2017) and Tanyaş et al. (2017)—currently the largest and most comprehensive repository of information on seismically-triggered slope failures, globally (Fan et al., 2019)—together with spatial morphometric and environmental variables in the areas covered by the 25 EQIL inventories, and on the seismic properties of the triggering earthquakes (Figure 1).

The manuscript is organized as follows. We begin by giving background information on the inherent difficulty to predict landslide sizes, including landslide area or other simple geometric measures of landslide size (Section 2). Next, we provide the theoretical background for our statistical models, and of the metrics that we selected to measure the performance of our models (Section 4). This is followed by a presentation of the data used to construct and validate our models, including the target and explanatory variables, and of the adopted terrain mapping unit (Section 3). Next, we compare the results of our modelling effort (Section 5) and we discuss the model outputs in view of their specific and general relevance, and we provide considerations on the impact of our approach for the modelling of landslide hazard (Section 6). We conclude summarizing the lessons learnt, with a perspective towards possible future research.

2 Background

Varnes and the IAEG Commission on Landslides and Other Mass-Movements (1984) were the first to define landslide hazard as "*the probability of occurrence within a specified period of time and within a given area of a potentially damaging landslide*" (Fell et al., 2008). The definition adapted to landslides the more general definition used by the United Nations Disaster Relief Organization (UNDRO) for all-natural hazards, which in turn was a generalization of the definition used for seismic hazard (National Research Council, 1991). Fifteen years later, Guzzetti et al. (1999) extended the definition to include the magnitude of the expected landslide, and landslide hazard became "*the probability of occurrence within a specified period of time and within a given area of a potentially damaging landslide of a given magnitude*". Today, this remains the most common and generally accepted definition of landslide hazard.

A problem with this definition is that, in contrast to other natural hazards—including, *e.g.*, earthquakes (Wood and Neumann, 1931; Gutenberg and Richter, 1936), volcanic eruptions (Newhall and Self, 1982), hurricanes (Saffir, 1973; Simpson, 1974), floods (Buchanan and Somers, 1976)—no unique measure or scale for landslide magnitude exists (Hungr, 1997a; Malamud et al., 2004b; Guzzetti, 2005). This complicates the practical application of the definition (Guzzetti, 2005). A further complication arises from the use of the same term "landslide" to address both the landslide deposit (*i.e.*, the failed mass) and the movement of slope materials or an existing landslide mass (Cruden, 1991; Guzzetti, 2005).

In the literature, different approaches and metrics were proposed to size or rank the "magnitude" of a single landslide, or a population of landslides—*i.e.*, a number of landslides in a given area resulting from a single event or multiple events in a period (Malamud et al., 2004b; Rossi et al., 2010). For single landslides, authors have proposed to measure landslide "magnitude" using the size (*e.g.*, area, depth, volume) (Fell, 1994; Cardinali et al., 2002; Reichenbach et al., 2005), velocity (UNESCO Working Party On World Landslide Inventory, 1995; Cruden and Varnes, 1996; Hungr et al., 2014), kinetic energy (Ksu, 1975; Sassa, 1988; Corominas and Mavrouli, 2011), or destructiveness (Hungr, 1997b; Reichenbach et al., 2005; Galli and Guzzetti, 2007) of the slope failure. Alternatively, Cardinali et al. (2002) and

Reichenbach et al. (2005) proposed to size landslide magnitude based on an empirical relation linking landslide volume and velocity, a proxy for momentum. Other possible metrics that can be used to measure the magnitude of a single landslide include, *e.g.*, the depth of the landslide mass, the total or the differential ground displacement caused by the landslide, the discharge per unit width (for landslides of the flow type), or the momentum of the failed mass.

For populations of landslides, Keefer (1984) proposed to use the total number of landslides—specifically, EQILs—caused by a single earthquake as a proxy for the landslide event magnitude. Using this scale, an event causing 10 to 100 landslides is assigned an event-magnitude of one, *i.e.*, $\mathbf{m}_L = \log_{10}(10) = 1$, and another event triggering 1000 to 10,000 landslides is given an event-magnitude $\mathbf{m}_L = \log_{10}(1000) = 3$. Malamud et al. (2004b) extended the approach to all possible landslide triggers—including, *e.g.*, earthquakes, rainfall events, snow melt events—and proposed to use the logarithm (base 10) of the total number of event landslides in an area to measure the landslide event magnitude, $\mathbf{m}_L = \log_{10} N_{LT}$, regardless of the size (area, volume) of the individual landslides, or of the total landslide area or volume. With this approach, Malamud et al. (2004b) assigned a $\mathbf{m}_L = 4.04$ to a population of $N_{LT} = 11,111$ EQIL caused by the 17 January 1994, Northridge, California, USA, earthquake (Harp and Jibson, 1995, 1996), a $\mathbf{m}_L = 3.98$ to a population of $N_{LT} = 9,594$ rainfall-induced landslides caused by Hurricane Mitch in late October/early November 1998 in Guatemala (Bucknam et al., 2001), and a $\mathbf{m}_L = 3.63$ to a population of $N_{LT} = 4,233$ landslides caused by a rapid snow melt event in January 1997, in Umbria, Italy (Cardinali et al., 2000). In the same paper, Malamud et al. (2004b) proposed an alternative approach to estimate landslide magnitude based on the total area of landslides associated with a landslide event, A_{LT}. Assuming their empirical Inverse Gamma distribution provided an accurate representation of the probability density of landslide area $p(A_L)$, they estimated the event landslide magnitude as $\mathbf{m}_L = \log_{10} A_{LT} + 2.51$. Based in this simple equation, they attributed the following magnitudes to the three mentioned inventories, $\mathbf{m}_L = 3.89$ for the EQIL caused by the Northridge earthquake, $\mathbf{m}_L = 3.98$ for the rainfall-induced landslides in Guatemala, and $\mathbf{m}_L = 3.61$ for the snowmelt induced landslides in Umbria. Comparison of the two different measures of landslide event magnitude reveals differences smaller than 4%, compatible with the inherent inaccuracy to landslide mapping (Guzzetti et al., 2012; Santangelo et al., 2015).

A few authors have established empirical probability distributions of landslide size (or measures thereof) including, *e.g.*, area (Stark and Hovius, 2001; Guzzetti et al., 2002; Malamud et al., 2004b; Korup et al., 2011; Chen et al., 2017; Jacobs et al., 2017), volume (Martin et al., 2002; Dussauge et al., 2003; Malamud et al., 2004b; Brunetti et al., 2009b), area-to-volume (Guzzetti et al., 2009; Larsen et al., 2010; Tang et al., 2019), and width-to-length (Parise and Jibson, 2000; Rickli et al., 2009; Taylor et al., 2018b) ratios. Moreover, a few authors have examined the factors controlling these distributions (*e.g.*, Pelletier et al., 1997; Guthrie and Evans, 2004; Stark and Guzzetti, 2009; Frattini and Crosta, 2013; Korup et al., 2012; Williams et al., 2018; Tanyaş et al., 2019b; Jeandet et al., 2019). Some of the established distributions were used to estimate landslide magnitude for hazard assessment at the catchment scale, where the probability of landslide area $p(A_L)$, was taken to represent landslide magnitude, *e.g.*, by Guzzetti et al. (2005a, 2006). However, the use of empirical probability distributions of measures of landslide size has several problems. First, to establish reliable distributions of, *e.g.*, landslide area or volume, one needs large numbers of empirical data, which can only be obtained from large and accurate landslide event inventory maps. These data are not common and difficult, time-consuming, and costly to prepare (Malamud et al., 2004b; Guzzetti et al., 2012). Second, although Malamud et al. (2004b) and Malamud et al. (2004a) have argued that their Inverse Gamma distribution, and other similar distributions (Stark and Hovius, 2001; Hovius et al., 1997), are general ("universal"), and do not depend on the local terrain or the triggering conditions, the hypothesis was challenged by, *e.g.*, Korup et al. (2011) and Tanyaş et al. (2018). It is not clear the extent to which a single distribution holds outside the geographical area where it was defined. Third, even the availability of reliable empirical distributions of landslide area or volume does not guarantee that the estimates obtained from the distribution are accurate in all parts of the study area where it was defined, and specifically in all slopes and sections of a complex landscape. Fourth, lack of standard methods and tools to properly model the probability distributions of landslide sizes hampers the possibility to confront empirical distributions obtained for different areas or the same area at different times (Rossi et al., 2012).

To the best of our knowledge, no model able to capture and predict the spatial distribution of landslide sizes (or measures thereof) has been proposed in the literature. However, for co-seismic landslides, few examples do exist where scholars have at least tried to estimate the controlling factors of landslide size. The most common observation points out to a possible relation between distance to rupture zone and landslide size (*e.g.*, Keefer and Manson, 1998; Khazai and Sitar, 2004; Massey et al., 2018; Valagussa et al., 2019). This implies that larger landslides are expected to be closer to the fault zone where the influence of ground motion is more intense. In fact, Medwedeff et al. (2020) indicated that the contribution of ground motion has a limited control on size of the landslides, compared to hillslope relief. Another common observation suggests that extremely large landslides can be generally associated with structural features (*e.g.*, Chigira and Yagi, 2006; Catani et al., 2016). Such features cannot be taken into account in regional multivariate analysis because of limited data regarding the discontinuity surfaces (Fan et al., 2019). Other investigators emphasise the control of ground-motion characteristics (*e.g.*, frequency content, duration) on landslide size (*e.g.*, Bourdeau et al., 2004; Jibson et al., 2004, 2020; Kramer, 1996; Valagussa et al., 2019). For example, Jibson and Tanyaş (2020) demonstrated a positive correlation between between landslide size and magnitude, ground motion duration, and mean period. These hypotheses require further analyses which need strong-motion records gathered from a very dense accelerometer monitoring network. Nevertheless, we lack such spatial detail to examine available earthquake-triggered landslide events. This may be the reason why even just explanatory models for landslide sizes are so limited in numbers.

Typical, statistically-based, spatially-distributed landslide predictive models attempt to identify "where" landslides may occur in a given region based on a set of environmental characteristics known to control, or condition landslide occurrence, or their lack of occurrence (Reichenbach et al., 2018). These susceptibility models explain the discrete, presence/absence of landslides in any given terrain mapping unit, be it, *e.g.*, a grid cell, a unique condition unit, a slope unit (SU), or any other terrain subdivision. For this purpose, the models exploit the Bernoulli probability distribution to describe the presence/absence (0/1) of landslides (Reichenbach et al., 2018). Therefore, in this context, the size of the landslides in each terrain mapping unit is irrelevant.

Recently, Lombardo et al. (2018b) have proposed to estimate the landslide intensity, an alternative measure complementary to landslide susceptibility, describing the expected number of landslides in any given terrain mapping unit. To estimate this intensity measure spatially over large and very large areas, the authors built statistically-based, spatially-distributed predictive models that adopt the Poisson probability distribution to explain the discrete number $(0, 1, 2, 3, \dots)$ of landslides in any given terrain mapping unit. Moreover, Lombardo et al. (2020a) have shown that the landslide intensity is positively correlated with the landslide area, explaining a large portion of its variability within slope units. Nevertheless, as for susceptibility models, the actual size of the landslides in each mapping unit is irrelevant for the implementation of intensity models, and such models cannot predict the size (*e.g.*, the area or volume) of the landslides.

In this work, we extend the traditional approaches used to estimate landslide susceptibility, and the more recent approach proposed to estimate landslide intensity, to model the size (area) of the landslides in any given terrain mapping unit in a landscape. For this purpose, we build statistically-based, spatially-distributed predictive models that adopt the log-Gaussian probability distribution to explain characteristics related to the area of landslides in each mapping unit, namely

- A_{Lmax}, the largest landslide in the considered terrain mapping unit; and
- A_{Lsum}, the sum of all landslide areas in the considered terrain mapping unit.

Further details on how A_{Lmax} and A_{Lsum} have been extracted from our dataset is provided in Sections 3.1 and 3.4, whereas a description of how these have been modelled is provided in Section 4.

3 Data

To test our modelling framework, we used information on *(i)* the location and the planimetric area of a large number of landslides caused by earthquakes of different magnitudes in various parts of the world; *(ii)* the morphometric and environmental settings in the same areas where the EQILs were triggered; and *(iii)* on the ground shaking conditions caused by the earthquakes that triggered the EQILs. In addition, we selected a type of terrain subdivision into mapping units known to be suited to model and predict landslides spatially.

3.1 Earthquake-induced landslide data

We obtained information on EQILs searching the largest collection (link here) of seismically-induced landslide event inventories currently available (Schmitt et al., 2017; Tanyaş et al., 2017). At the time of the search (March 2019), this unique source contained cartographic and thematic information on 64 EQIL inventories caused by 46 earthquakes that occurred between 1971 and 2016 globally, counting $554,333$ landslides (Figure 1). To select the inventories best suited for the scope of our work, we adopted two criteria. First, an inventory must have contained information on the (planimetric) area of each of the mapped landslides. Second, the landslides shown in the inventory must have been associated with an earthquake for which ground motion data were available from the U.S. Geological Survey (USGS) ShakeMap system (Worden and Wald, 2016). Applying the two criteria, we selected 25 EQIL inventories in the 40-year period between 1976 and 2016, which collectively encompass 319,086 landslides in 25 study areas in 13 nations, in all continents, except Oceania and Antarctica, and in a broad range of morphological, geological, tectonic, seismic, and climate settings (Figure 1 and Table 1).

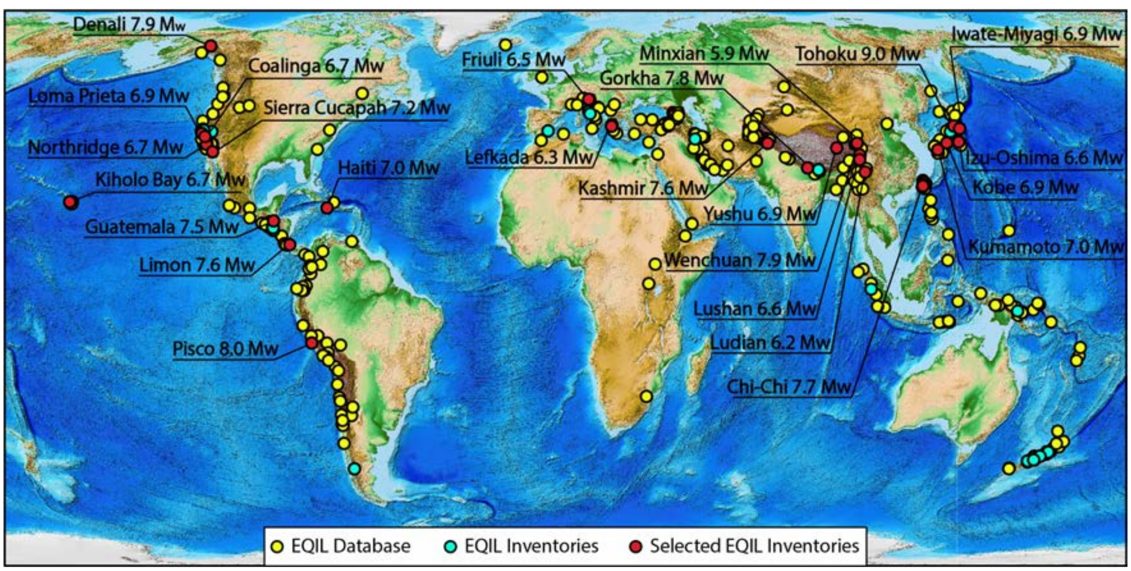

Figure 1: Map shows locations (yellow dots) of all the earthquakes known to have triggered landslides and reported in the co-seismic landslide database collated by Schmitt et al. (2017) and Tanyaş et al. (2017) publicly available (link here). The cyan dots show all the earthquakes for which the database above includes one or more corresponding landslide inventories, out of which, the red dots represent the inventories used in this study. Map uses Equal Earth map projection (EPSG:2018.048, Šavrič et al., 2019).

With the exception of the 2007 Pisco, Peru, inventory (see Figure 1 and ID 14 in Table 1), prepared using a combination of automated classification and manual adjustment techniques (Lacroix et al., 2013), all the selected inventories were obtained through the systematic, visual interpretation of satellite images and/or aerial photography (Tanyaş et al., 2017). For 23 out of the 25 EQIL inventories, showing a total of 303,269 landslides (95.0% of the total number of landslides), landslides were mapped as polygons, and the planimetric area of each landslide, A_L, in m^2, was calculated in a GIS. For 22 of these inventories, the polygon showing an individual landslide typically encompasses (*i.e.*, it does not separate) the landslide source and deposition areas. Only for the 2015 Gorkha, Nepal, inventory (see Figure 1 and ID 24 in Table 1) the source and deposition areas of each landslide were shown separately (Roback et al., 2017). For this inventory, to obtain the landslide area A_L we merged the landslide source and deposition areas. In the 2007 Pisco, Peru (Lacroix et al., 2013) (271 landslides, 0.09%), and the 2013 Lushan, China (Xu et al., 2015) (see Figure 1 and ID 21 in Table 1) (15,546 landslides, 4.0%), inventories, landslides were shown as points, corresponding to the known, inferred, or assumed location of the landslide initiation point, with the landslide area listed in a joint, attribute table.

It is known that uncertainty exists in the measurement of landslide area from event inventory maps (Ardizzone et al., 2002; Guzzetti et al., 2012; Santangelo et al., 2015). The causes of the uncertainty in EQIL inventories are several, and they include: *(i)* the amalgamation effect known to occur during and immediately after an earthquake-triggered landslide event due to local slope adjustments and chained instabilities, resulting in a fewer number of larger mapped landslides (Marc and Hovius, 2015; Tanyaş et al., 2019b); *(ii)* the retrogressive effect that enlarges—chiefly up-slope and less commonly laterally—a landslide, mainly in the source area, also resulting in a fewer number of larger landslides; *(iii)* the cartographic accuracy of the landslide inventory map, which depends on multiple factors including, *e.g.*, the scale of the map, the extent of the area covered, the number and complexity of the landslides, the scale and quality of the aerial or satellite imagery and of the base maps used to prepare the inventory, the accuracy of the remote sensing and GIS algorithms and procedures used to detect and map the landslides (Guzzetti et al., 2012); and *(iv)* the skills, experience, and number of the landslide investigators who prepared the landslide inventory (Guzzetti et al., 2012; Tanyaş and Lombardo, 2019). We acknowledge that the uncertainty in the EQIL inventories may have biased the obtained size statistics (Guzzetti et al., 2012; Tanyaş et al., 2019b). We maintain this cannot be avoided, and our modelling will ultimately be affected by this uncertainty. However, we are convinced that we selected for our study the landslide inventories from the best global repository of EQIL inventories currently available globally (Schmitt et al., 2017; Tanyaş et al., 2017).

3.2 Terrain mapping unit

Among the several possible terrain mapping units used for spatial landslide modelling (Hansen, 1984; Soeters and van Westen, 1996; Guzzetti et al., 1999; Reichenbach et al., 2018), we selected the "slope units" (SUs), which are geomorphological and hydrological ter-

Table 1: Main characteristics of the 25 earthquake-induced landslide (EQIL) data sets used in this work. Legend: ID, inventory number. See Figure 1 for location of the study areas. N, nation; ISO 3166-1, Alpha-2 country code. EQ, earthquake name. m, earthquake magnitude. Date, date of earthquake. E, extent of the study area. SU, number of slope units. SU_L, SUs with landslides. Area SU_L, total area of slope units with landslides. EQIL, number of earthquake induced landslides. A_{LT}, A_{Lmin}, A_{Lavg}, A_{Lmax} total, minimum, average, maximum landslide area. T, tectonic environment: Co, compressive; Ex, extentional; Tr, transcurrent. C, climate: Tr, tropical; Ar, arid; Te, temperate; Co, cold; Po, polar. Resolution of imagery used for mapping (Res.). References given for event ID: 1, Harp et al. (1981); 2, Govi (1977); 3, Suziki (1979); 4, Harp and Keefer (1990); 5, McCrink (2001); 6, Marc et al. (2016); 7, Harp and Jibson (1995, 1996); 8, Uchida et al. (2004); 9, Liao and Lee (2000); 10, Gorum et al. (2014); 11, Papathanassiou et al. (2013); 12, Sato et al. (2007); 13, Harp et al. (2014); 14, Lacroix et al. (2013); 15, Xu et al. (2014b); 16, Yagi et al. (2009); 17, Harp et al. (2016); 18, Barlow et al. (2015); 19, Xu et al. (2013); 20, Wartman et al. (2013); 21, Xu et al. (2015); 22, Xu et al. (2014a); 23, Ying-ying et al. (2015); 24, Roback et al. (2018); 25, NIED (2016).

ID	N	EQ	m	Date dd/mm/yy	E km^2	SU #	SU_L #	Area SU_L km^2	EQIL #	A_{LT} km^2	A_{Lmin} m^2	A_{Lavg} m^2	A_{Lmax} km^2	T	C	Res. m
1	Guatemala	Guatemala	7.5	04/02/76	6039	6114	1573	1817	6224	60.8	12	9765	1.26	Tr	Te	1
2	Italy	Friuli	6.5	06/05/76	542	362	158	372	1007	1.1	388	3931	0.07	Co	Te	-
3	Japan	Izu Oshima	6.6	14/11/78	867	766	157	279	659	1.5	155	2234	0.05	Tr	Te	5-25
4	USA	Coalinga	6.7	02/05/83	1853	1937	585	729	3980	4.8	9	1195	0.05	Co	Te	1
5	USA	Loma Prieta	6.9	18/10/89	107	60	27	73	138	0.4	173	2559	0.02	Co	Te	30
6	Costa Rica	Limon	7.6	22/04/91	2189	1206	239	564	1643	8.2	255	4966	0.09	Co	Tr	30
7	USA	Northridge	6.7	17/01/94	4029	4083	1307	1623	11111	23.8	1	2144	0.26	Co	Te	1-2
8	Japan	Kobe	6.7	17/01/94	213	133	83	179	2353	0.5	12	211	0.01	Co	Te	4
9	Taiwan	Chi-Chi	7.7	20/09/99	29804	24300	1358	3694	9272	127.5	68	13756	5.52	Co	Te	12.5
10	USA	Denali	7.9	03/11/02	8382	7019	592	1738	1579	121.2	890	76833	8.99	Tr	Po	1-30
11	Greece	Lefkada	6.3	14/08/03	180	116	54	100	274	2.9	130	10765	0.13	Tr	Te	<15
12	India-Pakistan	Kashmir	7.6	08/10/05	2656	1283	287	985	2424	10.4	2	4286	0.14	Co	Te	2.5
13	USA	Kiholo Bay	6.7	15/10/06	192	85	47	145	383	2.8	18	7314	0.19	Ex	Te	3
14	Peru	Pisco	8.0	15/08/07	23195	12576	153	1477	271	1.1	1000	39340	0.08	Co	Ar-Po	5
15	China	Wenchuan	7.9	12/05/08	75028	36852	8775	28979	197481	1160	31	5874	6.97	Co	Te	1-19.5
16	Japan	Iwate-Miyagi	6.0	13/06/08	685	634	388	480	4211	14.4	38	3396	1.01	Co	Te	5-10
17	Haiti	Haiti	7.0	12/01/10	3652	2690	1177	2188	23567	24.85	1	1060	0.23	Tr	Tr	0.6
18	Mexico	Sierra Cucapah	7.2	04/04/10	894	890	98	198	453	0.7	53	1549	0.01	Tr	Ar	2.5
19	China	Yushu	6.9	13/04/10	1346	654	304	901	2036	1.2	16	593	0.01	Tr	Po	0.2-10
20	Japan	Tohoku	9.1	11/03/11	16781	21377	1434	1732	3475	4.4	6	1252	0.11	Co	Te	0.5-2.5
21	China	Lushan	6.6	20/04/13	5586	3281	1558	3600	15546	18.5	100	1190	0.12	Co	Te	0.2-5.8
22	China	Minxian	5.9	21/07/13	421	341	126	187	2330	0.8	5	328	0.05	Co	Po	0.5-2
23	China	Ludian	6.2	03/08/14	343	156	89	271	1024	5.2	101	5070	0.41	Tr	Te	2-10
24	Nepal	Gorkha	7.8	25/04/15	29053	12193	1395	9810	24903	86.5	1	473	0.18	Co	Te-Po	0.2-0.5
25	Japan	Kumamoto	7.0	15/04/16	4973	5647	395	673	2742	8.2	17	3198	0.45	Tr	Te	-

rain subdivisions bounded by drainage and divide lines (Carrara, 1988; Alvioli et al., 2016). SUs represent a good geometric description of natural slopes, where most landslides occur. For our work, we exploited the same sets of SUs used previously by Tanyaş et al. (2019a) to model landslide susceptibility, and to predict the spatial occurrence of landslides, in the same 25 study areas. Tanyaş et al. (2019a) generated the SUs terrain subdivisions for the study areas (Figure 1 using *r.slopeunits*, an open source software for GRASS GIS (GRASS Development Team, 2017) developed by Alvioli et al. (2016) for the automatic partitioning of a landscape into SUs. Table 1 lists the main geometric characteristics of the $144,724$ SUs in the 25 study areas, which collectively cover 219,010 km^2.

In consolidated methods to estimate the landslide susceptibility, intensity, and hazard (Reichenbach et al., 2018; Lombardo et al., 2018a; Guzzetti et al., 2005a), binary datasets are built by assigning to each mapping unit a label indicating the presence/absence of landslides or their count. In this process, mapping units containing the information of slope failures are as important as mapping units where the instability has not been observed. As a result, a balanced (Marjanović et al., 2011) or unbalanced (Frattini et al., 2010; Lombardo and Mai, 2018) dichotomous dataset constitute the basic information upon which any following model is regressed. In our case, since we do not have to classify the SUs, but rather build a model on the basis of the landslide planimetric area, we are only interested in the SUs with mapped landslides, where the extent per mapping unit can be computed.

For this reason, from the initial set of $144,724$ SUs—representing all the mapping units combined across the 25 study areas, we extracted a sub-set of $23,343$ SUs (16.1%, for a total area of about $62,794$ km^2) where EQILs have been mapped reporting their planimetric extent. This subset represents the dataset upon which we will build our modelling protocol. As for the complementary sub-set made of $121,661$ SUs without known landslides—83.9%, for a total area of about $156,216$ km^2– we separately store this information for it will enter the whole procedure only as the prediction target (as explained in Section 4.4).

3.3 Morphometric, environmental, and seismic data

For our modelling, we used an initial set of morphometric, environmental, and ground shaking (seismic) data obtained from a variety of digital cartographic sources. The data we used can be grouped into three main classes, namely:

- terrain morphometric properties, which we obtained from the 1 $arcsec \times 1$ $arcsec$ (approximately, 30 $m \times 30$ m, at the equator) SRTM Digital Elevation Model (DEM) (Farr et al., 2007);
- soil properties, derived from SoilGrids, at about 250 $m \times 250$ m resolution (Hengl et al., 2017); and
- ground motion properties, derived at about 1 $km \times 1$ km resolution from the U.S. Geological Survey (USGS) ShakeMap system (Worden and Wald, 2016).

Overall, we initially select 19 covariates, here listed in Table 2. From the SRTM DEM, we obtained nine covariates representing terrain morphometric properties known to be related to the presence or absence of landslides, and specifically EQILs. We computed the Terrain Slope, because steepness is known to balance the retaining and the destabilising forces (Taylor, 1948). Planar and Profile Curvatures influence convergence and divergence of shallow gravitational processes and overland flows (Ohlmacher, 2007). The Vector Ruggedness Measure (Sappington et al., 2007) is a proxy for terrain roughness (Amatulli et al., 2018) whereas Topographic Wetness Index is a function of the local slope and of the upstream contributing area that quantifies the topographic control on hydrological processes (Grabs et al., 2009). We computed three possible realizations of the Terrain Relief namely intensity, range, and variance (Stepinski and Jasiewicz, 2011). These topographic representations are meant to carry the signal of gravitational potential energy across the landscape. The idea is that, taking aside the role of other predisposing factors, a location with a higher relief than another also has a higher potential energy. As a result, the same potential energy is converted into kinetic energy if a landslide occurs, hence the resulting runout should be larger than the theoretical runout of a landslide failed with a lowere relief. The relief intensity is computed as the average difference between the elevation of a grid-cell and those included in a neighbourhood that we chose within a diameter of 1 km. Conversely, the relief range is expressed as the difference between the minimum and maximum elevations within the same circle. And, the relief variance expressed the variability of the elevation values within the same circle.

We also calculate the distance to streams as the Euclidean distance from each 30 $m \times$ 30 m grid cell to the closest streamline. We note here that the parameterization used to extract the river network has been kept consistent across each of the 25 study areas. The last covariate we obtained from the DEM consists of Landforms (or Landform Classes). These are represented by five landforms, from L1 to L5, representing flat topographies in L1, foot slope and valley in L2, spur and hollow in L3, slope, ridge, shoulder in L4 and summit in L5.

In addition to the mentioned morphometric covariates, we selected four additional covariates describing the geometric properties of our landscape partitioning into SUs, namely: the slope unit area, A_{SU}; the maximum distance between any given pairs of points within a SU, a measure of the SU elongation, D_{SU}. From these two geometrical properties, we compute two shape indices both indicating the elongation or circularity (these measures are reciprocal) of the given SU. The first of the two indices is computed as the maximum distance divided by the SU Area (D_{SU}/A_{SU}); and the second corresponds to ratio of the maximum distance divided and the root square of the SU Area ($D_{SU}/\sqrt{A_{SU}}$).

Due to the global nature of our study, we initially considered also Soil physico-chemical parameters derived from SoilGrids, (Hengl et al., 2017). We considered the bulk density the weight of the soil draping over the underlying rock controls the failure mechanism (Adams and Sidle, 1987; Cheng et al., 2012). Similarly, the soil depth to the bedrock expressed the

Table 2: Summary of our initial covariate set.

Covariate	Acronym	Reference	Unit
Terrain Slope	Slope	Zevenbergen and Thorne (1987)	*deg*
Planar Curvature	PLC	Heerdegen and Beran (1982)	$1/m$
Profile Curvature	PRC	Heerdegen and Beran (1982)	$1/m$
Vector Ruggedness Measure	VRM	Sappington et al. (2007)	*unitless*
Topographic Wetness Index	TWI	Beven and Kirkby (1979)	*unitless*
Terrain Relief Intensity	Relief Int	Jasiewicz and Stepinski (2013)	m
Terrain Relief Range	Relief Range	Jasiewicz and Stepinski (2013)	m
Terrain Relief Variance	Relief Var	Jasiewicz and Stepinski (2013)	m
Distance to Stream	D.stream	*e.g.*, Samia et al. (2020)	m
Landform Classification	LC	MacMillan and Shary (2009)	*unitless*
Slope Unit Area	A_{SU}	Lombardo et al. (2020b)	m^2
Slope Unit Maximum Distance	D_{SU}	Castro Camilo et al. (2017)	m
Slope Unit Elongation Index 1	D/A	Castro Camilo et al. (2017)	*unitless*
Slope Unit Elongation Index 2	$D/\sqrt{A}$	Castro Camilo et al. (2017)	*unitless*
Bulk Density	BD	Hengl et al. (2019)	$kg\ m^{-3}$
Depth to Bedrock	DB	Shangguan et al. (2017)	m
Clay Fraction Concentration	CFC	Wan and Wang (2018)	g/g$\times$100
Peak Ground Acceleration	PGA	Wald et al. (1999)	g_{n}
Microseismic Intensity	I_M	Wald et al. (2012)	*unitless*

thickness of material that can potentially fail, where the thicker the failed soil column the larger the landslide is expected to be (Lombardo et al., 2016; Lagomarsino et al., 2017). As for the soil clay content, this property should carry the signal of potentially swelling soils (Khaldoun et al., 2009).

Two seismically-related covariates provide spatially-distributed ground shaking characteristics for the 25 earthquakes that caused the EQILs in our study areas, namely, the microseismic intensity, I_M (Wald et al., 2012); and the peak ground acceleration (PGA), expressed in units of gravity (g) at 1 km $\times$ 1 km resolution (PGA, Wald et al., 1999).These deterministic estimates of the ground motion represent the severity of ground shaking contributes to the destabilising forces (*e.g.*, Nowicki et al., 2014; Kritikos et al., 2015; Meunier et al., 2007).

We remind here that the properties listed above are computed for grid cells. As we opt for a different mapping unit (see Section 3.2), each property is pre-processed to aggregate the lattice information to the chosen units (see Section 3.4). Also, we chose a large set of properties to incorporate as much information as possible. Nevertheless, our modelling protocol will feature a variable selection step aimed at removing non-informative or redundant properties (see Section 4).

3.4 Pre-processing strategy

As mentioned above, we used landslide area as our dependent (target) variable, and we measured the size of each landslide as the planimetric area of the polygon encompassing it, *i.e.*, $landslide\ size = A_L$. This information was then aggregated per SU and expressed on the natural logarithmic scale, *i.e.*, $\log(A_L)$. Specifically, we prepared two landslide datasets, which we used to construct two different models. For our first model (*"Max model"*), we computed the maximum area of all the landslides included in each slope unit, A_{Lmax}. For our second model (*"Sum model"*), we selected the sum of the areas of all the landslides per slope unit, A_{Lsum}.

We provide a graphical sketch of our aggregation scheme in Figure 2. When a single landslide polygon is contained in a SU, we assigned to the SU the same value of A_{Lmax} and A_{Lsum} (*e.g.*, SU5 and SU6). When two or more landslide polygons fall inside a SU, the overall areal value assigned to the mapping unit is obtained as the maximum out of all cases for A_{Lmax} and as the cumulative value for A_{Lsum} (*e.g.*, SU1 and SU7). Moreover, when no landslides occured within a SU, we assigned a not-a-number (NaN) to both A_{Lmax} and A_{Lsum} for we would like to estimate what would be the expected landslide size in those cases. Notably, the SUs with A_{Lmax} and A_{Lsum} equal to NaN will not enter the model in its calibration step and as mentioned above, they will represent the prediction target once the model is built.

In addition to the preparatory steps for the target variable, the set of properties we described in Section 3.3 has also been pre-processed. For each morphometric, soil and seismic property, we computed the mean and standard deviation of all the grid cells contained in a SU. Conversely, we assigned to each slope unit the signal of the Landform class with the largest extent. We stress here that this step may smooth out the signal of less present Landform classes although they may still contribute to the failure initiation.

In Figure 3 we show the distribution of few covariates we computed, for each of the 25 study areas. Notably, most of them are distributed differently among study sites. Therefore, to respect the unity of each site, in our modelling scheme we introduced an additional covariate expressing the given earthquake. In doing so, we assigned an earthquake ID to each slope unit. Further details on how this covariate is used in our model are provided in Section 4.

4 Modelling and inference

In this section, we present the statistical models assumed to be capable of fitting and predicting the spatial distribution of observed A_{Lmax} and A_{Lsum}, which will also be used to predict unobserved landslide sizes (*i.e.*, A_{Lmax} and A_{Lsum} for a SU with no landslide). Below we provide details in terms of the theoretical (Bayesian) framework, the model structure and components, as well as the computational aspects of the inference approach.

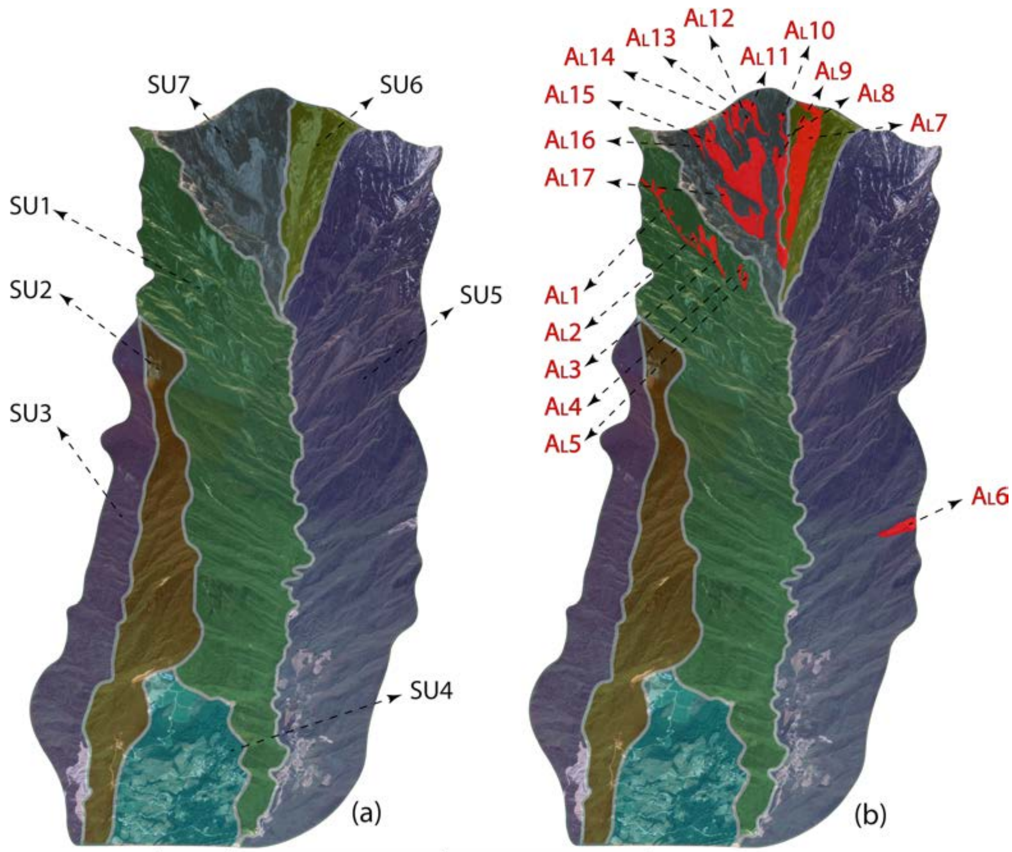

SU-ID	ALmax	ALsum
SU1	max(AL1:AL5)	sum(AL1:AL5)
SU2	NaN	NaN
SU3	NaN	NaN
SU4	NaN	NaN
SU5	AL6	AL6
SU6	AL7	AL7
SU7	max(AL8:AL17)	sum(AL8:AL17)

(c)

Figure 2: Graphical example of a slope unit partition (a), shown for seven slope units (from SU1 to SU7). Graphical example of a small landslide population (b), shown for 17 landslides as red polygons (from A_{L_1} to $A_{L_{17}}$). The table (c), gives an overview of how we calculated the *max* and *sum* of all landslide areas per slope unit. For instance, SU2, SU3 and SU4 have A_{Lmax} and A_{Lsum} set to zero because no landslide exists within these mapping units. As for SU5 and SU6, A_{Lmax} and A_{Lsum} values are the same because only one landslide falls within these mapping units. And, SU1 and SU7, have different A_{Lmax} and A_{Lsum} values after the aggregation step because multiple landslides are associated with these two slope units.

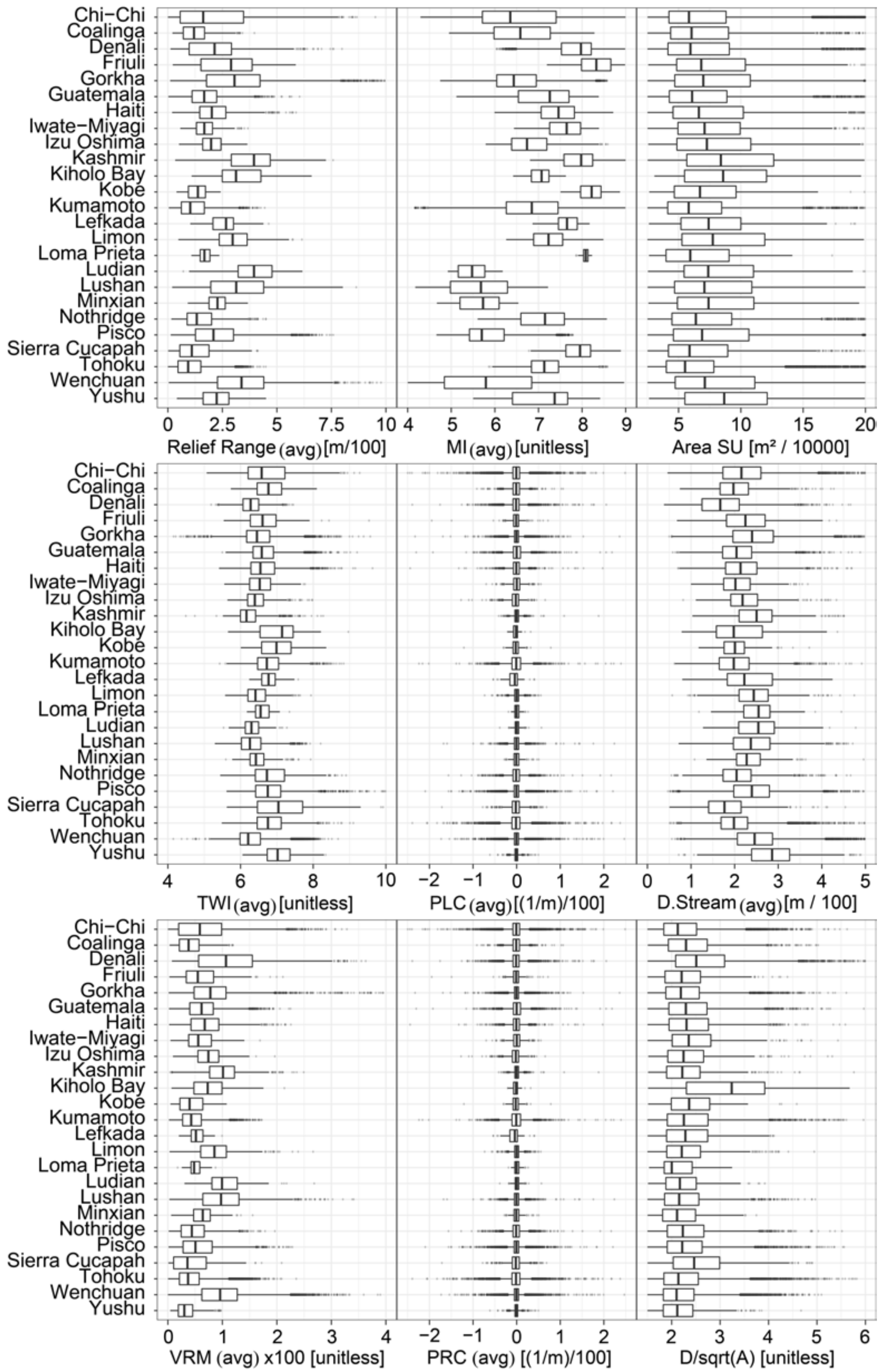

Figure 3: Distribution summary of nine example covariates, for each of the earthquakes under consideration. Notably, the units along the abscissas have been transformed into integers for pure graphical purposes.

4.1 Statistical modelling

Here, we describe our modelling framework, which we adopt to understand the (possibly non-linear) effect of the explanatory variables over the landslide size. We assume that landslide sizes in the considered terrain mapping unit $\mathbf{s}$, follow a log-Gaussian distribution with an additive structure in the mean and a site-specific variance. The mean is our main object of interest, and we would like to describe it accurately. We mathematically formalise our previous assumption as follows: let $A_L(\mathbf{s})$ be the landslide size at slope unit $\mathbf{s} \in \mathcal{S}$, where $\mathcal{S}$ represents all the study area. $A_L(\mathbf{s})$ can be either the largest possible landslide (A_{Lmax}) or the sum of landslide sizes (A_{Lsum}) over the considered mapping unit. Then,

$$\log\{A_L(\mathbf{s})\} \sim \mathcal{N}\left(\mu(\mathbf{s}), \tau\right),$$
$$\mu(\mathbf{s}) = \alpha + \sum_{m=1}^{M} \beta_m x_m(\mathbf{s}) + \sum_{l=1}^{L} f_l(\mathbf{z}_l(\mathbf{s})), \tag{1}$$

where:

- $\tau = 1/\sigma > 0$ is the precision parameter (reciprocal of the variance) that measures the concentration of all values $\log\{A_L(\mathbf{s})\}$, $\mathbf{s} \in \mathcal{S}$, around their mean $\mu(\mathbf{s})$. As mentioned before, our main focus is on the mean of the landslide sizes rather than their variances. Therefore, we assume a reference prior distribution for τ, which means that the prior is guaranteed to play a minimal role in the posterior distribution (Gelman et al., 2013). Specifically, we consider a flat prior by assuming that $\tau \sim \text{Gamma}(1, 5 \times 10^{-5})$ *a priori*, so that the precision is centered at 20,000 and has a huge variance of 4×10^8.

- α is a global intercept,

- the coefficients $(\beta_1, \ldots, \beta_M)^T$ quantify the fixed effects of the chosen linear covariates $\{x_1(\mathbf{s}), \ldots, x_M(\mathbf{s})\}$ on the mean response, and

- $\{f_1(\cdot), \ldots, f_L(\cdot)\}$ is a collection of functions that characterize non-linear effects defined in terms of a set of bins $\{\mathbf{z}_1, \ldots, \mathbf{z}_L\}$. These are explained more in depth below.

We adopt a Bayesian approach, and therefore assume that the model coefficients β_m and $f_l(\cdot)$, ($m = 1, \ldots, M$, $l = 1, \ldots, L$) are unknown and random, with a joint Gaussian distribution *a priori*. This modelling approach corresponds to the class of latent Gaussian models, which includes a wide variety of commonly applied statistical models (Rue et al., 2017; Hrafnkelsson et al., 2020; Jóhannesson et al., 2020). To identify the covariates that may enter to the $\log(A_{Lmax})$ or $\log(A_{Lsum})$ models in the form of linear or non-linear predictors, we conducted a model selection. The selection was based on the Watanabe-Akaike information criterion (WAIC; Watanabe, 2010, 2013) and the Deviance information criterion (DIC; Spiegelhalter et al., 2002), which measure a model's goodness-of-fit, while penalizing its complexity, in order to favour parsimonious models and prevent overfitting. Lower values

Table 3: Summary of selected covariates for both models. In the second column, RW1 refers to random walks of order 1, while RI refers to random intercepts.

Fixed effects	Random effects
Area SU, D/$\sqrt{\text{A}}$, Relief range (mean and sd), Distance to streams (mean and sd), Sd of slope, VRM (mean and sd), Plan cur. (mean and sd), Prof cur. (mean and sd), TWI (mean and sd), MI (mean and sd)	RW1: Mean slope RI: Landform and Earthquake inventories

of these criteria lead to better models. For each covariate that was linearly included in the models, we tested whether a non-linear random effect for the covariate would significantly improve the model. For both response variables, the final models include the same linear and non-linear random effects. The latter ones take the form of random intercepts and random walks of order 1 (see Table 3). Random walks of order 1 (RW1) can be defined as follows: for any continuous covariate $x_l = x_l(\mathbf{s})$, let $\mathbf{z}_l = (z_{l,1}, \ldots, z_{l,K_l})^T$ be a discretisation of x_l into K_l equidistant bins. If we assume that the random non-linear effect $f_l(\cdot)$, defined on $\mathbf{z}_l$, satisfies

$$\Delta_{l,j} = f_l(z_{l,j}) - f_l(z_{l,j-1}) \sim \mathcal{N}(0, 1/\kappa_l),$$

then $f_l(\cdot)$ is a normal random walk of order 1 with precision parameter $\kappa_l > 0$, which controls the "smoothness" of the random walk. Note that since $f_l(z_{l,j}) = f_l(z_{l,j-1}) + \Delta_{l,j}$, at each covariate level j, then $f_l(z_{l,j})$ is obtained as a displacement of random length and direction from the previous value $f_l(z_{l,j-1})$. The dependence induced by this type of construction is particularly useful when few values of the original covariate x_l are contained in a particular bin.

Random intercept or independent and identically distributed Gaussian random effect models (iid models) are one of the simplest way to account for unstructured variability in the data. For every slope unit $\mathbf{s} \in \mathcal{S}$, the precision matrix of iid random effects is $\gamma(\mathbf{s})\mathbb{I}$ where $\mathbb{I}$ denotes the identity matrix and $\gamma(\mathbf{s}) \sim \text{Gamma}(1, 10^{-5})$ *a priori*. As shown in Table 3, we used iid models for Landform and Earthquake inventory.

4.2 Uncertainty quantification and the Bootstrap

The modelling approach described in Section 4.1 describes landslide sizes through a set of covariates at each specific slope unit, without taking into account possible spatial dependence between slope units in the same event. A proper spatial model should include interactions between slope units, which in statistical terms implies defining a covariance structure for all the 22,343 non-missing slope units. Although it is possible to define such structures using a neighbouring approach where only close-by slope units will interact, and therefore the associated covariance matrix might be less dense, the high-dimensionality of our data prohibits us from fitting such a model. Alternatively, we could have separate models for each of the 25 inventories and define the covariance structure locally. However, model comparison would be challenging, as not all covariates might have the same effect over all the events.

In terms of statistical estimation, not addressing the spatial dependence between slope units mainly affects the uncertainty of the estimates, *i.e.*, the credible intervals. Pointwise estimates remain unchanged. To assess the uncertainty of parameter estimates, we here use a parametric bootstrap procedure accounting for spatial dependence in the model residuals. The Bootstrap is a resampling method that can be used to assign measures of accuracy to estimates. Our parametric Bootstrap is constructed as follows: for any of the two models, we compute the model residuals (*i.e.*, we subtract to the observed values the fitted values, $\log(A_L)(\mathbf{s}) - \hat{\mu}(\mathbf{s})$). Then, we fit a spatial model to the residuals of each inventory separately (*i.e.*, treating inventories as independent). We then generate 300 residual Bootstrap samples using the fitted spatial model. To express these samples in the scale of the data, we add back the fitted values $\hat{\mu}(\mathbf{s})$, given rise to 300 Bootstrap samples of landslide sizes. Finally, we fit the model in (1) to each one of these samples, for both models. The spatial model fitted to the residuals corresponds to a stationary isotropic Gaussian process with an exponential covariance function (see, *e.g.*, Cressie, 2015, Section 2.3). The Bootstrap is essential for accurate quantification of the uncertainty, as, without it, uncertainty estimates might be too optimistic, *i.e.*, parameter credible intervals might be too narrow in both models.

4.3 Bayesian inference with R-INLA

Bayesian inference is typically performed using computationally expensive approaches such as Markov chain Monte Carlo (MCMC). Here, we overcome these computational costs using the integrated nested Laplace approximation (INLA; Rue et al., 2009). When exploiting INLA, the posterior distribution of the parameters of interest are approximated using numerical methods, which makes it possible to compute the required quantities in a reasonable amount of time. The INLA methodology is conveniently implemented in the R-INLA package (Bivand and Piras, 2015) and we use it to obtain an accurate approximation of posterior marginal densities of interest, such as those for $\mu(\mathbf{s})$ and the parameters introduced in Section 4.1.

4.4 Landslide area simulation

The R-INLA package offers built-in functions to compute posterior samples even at locations where we do not have observations. In other words, using the model fitted to the complete dataset, we can infer the distribution of each missing landslide size. Internally, R-INLA treats missing values as values that we need to predict. Therefore, if we provide the set of explanatory variables accompanying the missing landslide areas, R-INLA will use the fitted model to predict (or fill in) the missing values. In practice, R-INLA performs model fitting and prediction at the same time, producing all the required results in a short amount of time. Here, we generated 5000 posterior samples for each missing landslide area. These posterior distributions are summarized in term of their mean and 95% credible intervals.

To put it simply, in a Bayesian framework, the estimation of the posterior regression coefficients consists of a distribution of possible values. Therefore, by sampling at random each distribution for the effect of each covariate, it is possible to statistically simulate a given process. Here, we simulated 5000 predictive functions to estimate the mean behaviour as well as the uncertainty in the landslide area prediction for each SU. This is a crucial step because those SUs encompassing one or more landslides provide enough information to assess the whole spectrum of possible landslide areas (mean and 95% CI for both the Max and Sum models). However, the SUs where no landslides have been recorded require the simulation step to recover analogous information.

4.5 Goodness-of-fit and predictive performance assessment

We here describe numerical and graphical methods to assess the goodness-of-fit and the predictive performance of our models.

- **Probability integral transform (PIT):** PIT values are useful leave-one-out goodness-of-fit measures. They are computed as follows

$$P_i = F_{-i}(y_i), \quad i \in \{1, \ldots, |\mathcal{S}|\},$$

  where F_{-i} is the cumulative distribution of a model fitted using all the available data except the i-th observation, y_i, $\mathcal{S}$ contains all the slope units $\mathbf{s}$, and $|\mathcal{S}|$ is the cardinality of $\mathcal{S}$, *i.e.*, the number of slope units. A model with a perfect predictive ability should have PIT values closely distributed according to a standard uniform distribution. Indeed, assuming that F_{-i} is continuous (which is the case here) the distribution of P_i, $i = 1, \ldots, |\mathcal{S}|$, can be written as

$$\Pr(P_i \leq u) = \Pr(F_{-i}(y_i) \leq u) = \Pr(y_i \leq F_{-i}^{-1}(u)), \qquad u \in (0, 1).$$

  The model F_{-i} has a perfect prediction ability if it is able to generate y_i (the value that was left out). This means that F_{-i} is a perfect prediction if $y_i \sim F_{-i}$ which, in turns, implies that

$$\Pr(y_i \leq F_{-i}^{-1}(u)) = F_{-i}(F_{-i}^{-1}(u)) = u.$$

  The above equation implies that the distribution of the PIT values $\{P_1, \ldots, P_{|\mathcal{S}|}\}$ should be uniformly distributed in $(0, 1)$. The uniformity of the PIT values is a necessary condition for the prediction to be perfect (Gneiting et al., 2007) and any deviation from uniformity, implies a decrease in performance.

- **Plot of observed vs. fitted values:** In such a plot, we can see how much the fitted values deviate from the actual observed landslide areas. A model with a reasonable performance should produce values aligned with the main diagonal (*i.e.*, the 45° line).

- **Probability coverage:** given a probability $\alpha \in (0, 1)$, we compute the proportion of times a $(1 - \alpha)100\%$ credible interval contains the observed data. If the underlying model is adequate, then the computed proportion (usually called sample coverage) should be close to $(1 - \alpha)100\%$ (the nominal coverage). In practice, the Bayesian methodology allows us to simulate from the posterior distribution in order to compute as many credible intervals as desired.

  For a readership who is unacquainted with the coverage concept, below we provide a brief and simple explanation. Using posterior simulations, we construct 5000 estimates for each observed A_L value. Then, for each A_L, we compute sample p-quantiles, with $p = \{0.025, 0.05, 0.075, \ldots, 0.950, 0.975\}$ (a sequence from 0.025 to 0.975 with steps of size 0.025). These sample quantiles allow us to construct credible intervals of sizes $(1 - \alpha)100\% = \{10\%, 15\% \ldots, 90\%, 95\%\}$. Then, we count how many times the observed A_L values fell within these intervals. If the model is adequate, for a credible interval of size $(1 - \alpha)100\%$ the number of times the observed A_L is contained should be close to $(1 - \alpha)100\%$. For instance, a 95% credible interval should contain 95% of the observed A_L values. Therefore, if we plot the nominal coverage versus the sample one, a reasonable model will show points aligned with the 45° line.

5 Results

In this section we present a summary of the model performance for each landslide size models, $\log(A_{Lmax})$ and $\log(A_{Lsum})$. We then provide an overview of the inferred covariate effects and conclude presenting a graphical translation of the model's output into map form.

5.1 Predictive Performance

Figure 4 shows an overview of the model performance presented in agreement with the three metrics we explored, namely, probability integral transform (PIT) plots, observed versus fitted values and coverage probabilities. The top row shows the performance for the Max model, while the bottom row shows the performance for the Sum model. The collection of probabilities detailed in Section 4.5, computed using all the training data, gives rise to the histogram in Figures 4a,d. We can see that both models capture the bulk of the distribution (bars close to the dashed line) reasonably well, but they do not seem to appropriately capture the tails of the landslide size distribution (bars far from the dashed line). The latter is expected since the normal and log-normal distributions have light tails, which implies that the model will give fairly low probabilities (*i.e.*, very close to 0) to extreme landslide sizes. We recall here that for a model to be optimal, the PIT plot should exhibit a uniform distribution. Here, we can see some moderate departure from the uniform distribution in both cases, but this is expected for such a large dataset combining various heterogeneous EQIL inventories.

Overall, the Max model seems to be better calibrated than the Sum model. Observed versus fitted values look similar for both models (Figures 4b,e), although the Max model exhibits pair of points slightly better aligned and equally spread along the 45° line. As for the coverage probabilities (Figures 4c,f), both models appear to be surprisingly excellent with most of the nominal to sample coverage pairs very well aligned with the 45° line and the bulk of the distribution showing a negligible deviation from it.

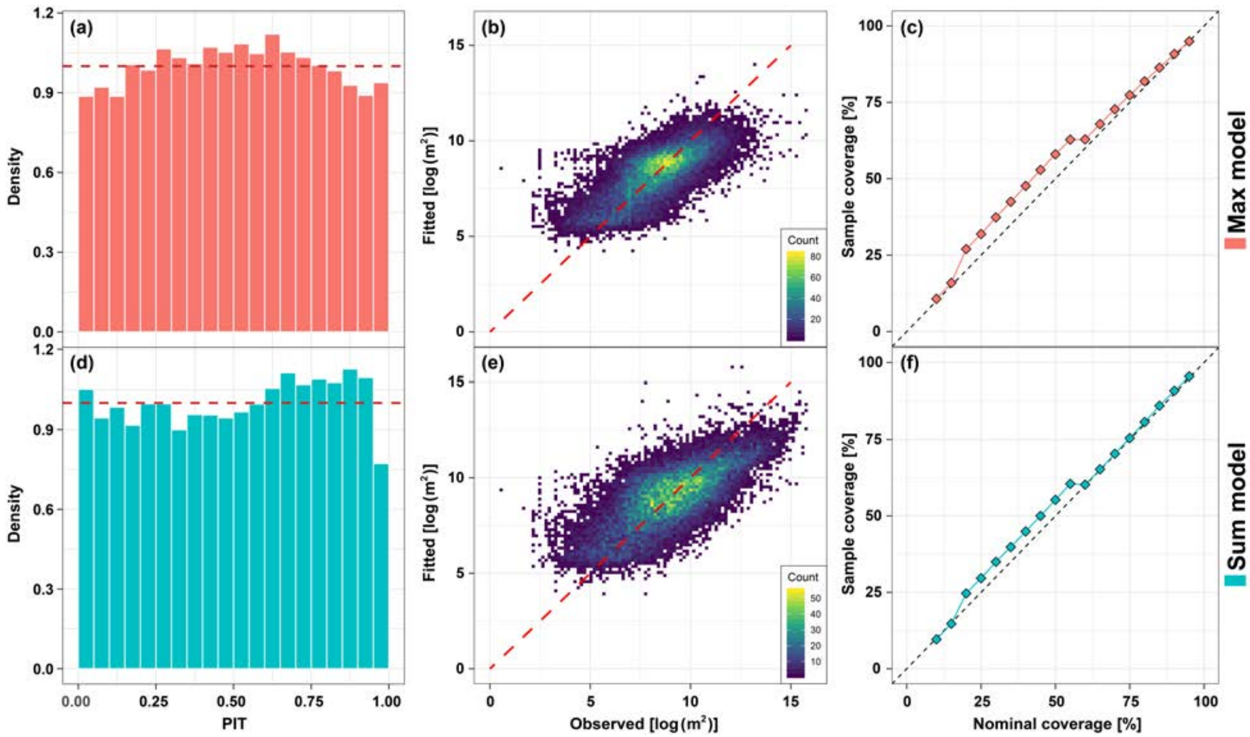

Figure 4: Left to right: Probability integral transform (PIT) plots, fitted versus observed plots (in log-scale), and coverage probabilities for the Max (top) and Sum (bottom) models.

As mentioned in Section 4.5, the coverage plots are computed by simulating 5000 samples from each model and counting the proportion of times the observed data are within a $(1-\alpha)100\%$ simulated-based credible interval, with $\alpha = \{0.05, 0.10, \ldots, 0.90\}$ (the nominal coverage). A model with a reasonable coverage should give a proportion close to $\alpha 100\%$. We can see that our models succeed in recovering the nominal coverage for extreme nominal coverage values, but they are a bit off for central nominal coverage values. Overall, the Sum model performs slightly better than the Max model.

5.2 Linear Covariate Effects

Figure 5 shows the estimated coefficients of linear (or fixed) effects (except for the intercept) for the Max and Sum models. Notably, we plot the 95% credible intervals originated from the Bootstrap rather than directly from INLA, which incorrectly assumes conditional independence for model fitting. We recall here that because of this, INLA may largely underestimate the uncertainty compared to Bootstrap, which more realistically accounts for spatial dependence at the data level. In light of this, here we only report the Bootstrap uncertainty and do not show the uncertainty directly estimated with INLA.

The selected covariates, that have been rescaled to have mean 0 and variance 1, show relatively strong positive and negative influences on landslide sizes. More specifically, out of 17 covariates used linearly only 7 appeared to be significant for the Max model, and 8 for the Sum model. Non-significance does not necessarily imply that the model is not influenced by these covariates. Significance indicates that the model is 95% certain of the role (either positive or negative) of the given covariate with respect to the landslide size. Moreover, the extent to which a covariate—significant or not—contributes to the model is summarized by the absolute value of the posterior mean regression coefficient.

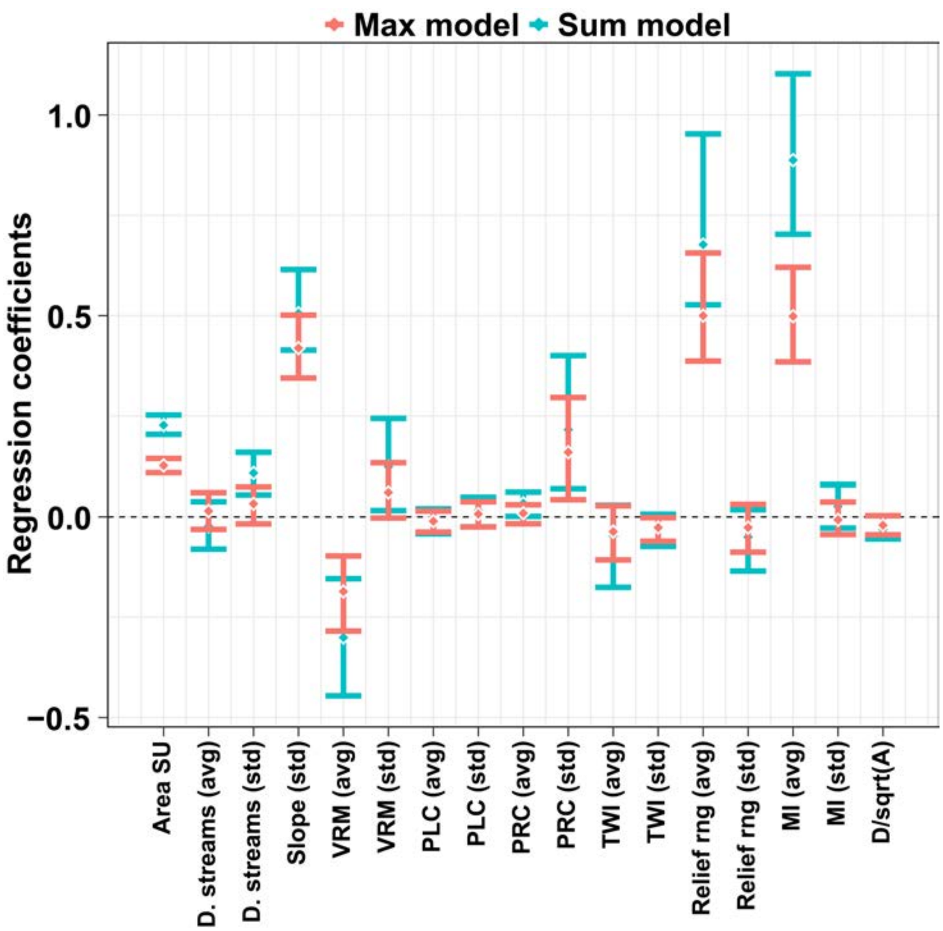

Figure 5: Posterior means (dots) of fixed linear effects (except the intercept) with Bootstrap-based 95% credible intervals (vertical segments) for the Max and Sum models. The horizontal black dashed line indicates no contribution to the landslide sizes.

In this sense, the largest linear contributors for the Max model are *MI (avg)* and *Relief rng (avg)*, both with an absolute mean regression coefficient of 0.50. Besides, *Slope (std)*, *VRM (avg)*, Prof Cur (std) and Area SU contribute with absolute posterior mean coefficients of 0.42, 0.18, 0.16 and 0.13, respectively. From these ranks, the contribution becomes less prominent and it decays down to the least contributor represented by *MI (sd)* with $|\hat{\beta}| = 0.0007$.

The covariates appeared to be ranked with a primary control on the estimated landslide size exerted by the relief, a proxy for gravitational potential energy and by the MI, a proxy for the ground motion stress. The role of the slope steepness is also well represented in the model as well as the dimension of the mapping unit itself. Specifically, these covariates present a significant and positive posterior distribution which contributes to increase the expected landslide size (*e.g.*, Medwedeff et al., 2020; Valagussa et al., 2019). Conversely, a negative regression coefficient, *e.g.*, for *VRM (avg)*, implies that larger landslide sizes for the Max model are expected for smaller *VRM (avg)* values. The negative contribution of the *VRM (avg)* is also consistent with the current literature. For instance, Tanyaş et al. (2017) show that frequency of EQILs are higher for low VRM (avg) values and the same frequency decreases for higher *VRM (avg)* values. The authors opened an interesting discussion on this topic. They assumed that *VRM (avg)* may be a close proxy for the strength of hillslope material. In fact, rocky landscapes tend to be much more topographic rough than gentle landscapes which are often dominated by thick soil covers or deposits, which in turn are usually associated with lower geotechnical strength. These are surely some reasonable considerations but we note here that an equally valid interpretation could still be made. In fact, the negative contribution of the *VRM (avg)* could be explained as a confounding effect between covariates that may convey a similar information to the model. In such cases, one of the two covariates may be estimated with a large regression coefficient and the second one would be estimated with a lower and opposite regression coefficient. For instance, this could be the case for covariates such as *VRM (avg)* and *PRC (std)* or *Slope (std)*, as they could express rough topographies.

For the Sum model, the dominant fixed effect appears to be the *MI (avg)*, with an absolute mean regression coefficient of 0.89. This is followed by *Relief rng (avg)* with $|\hat{\beta}| = 0.68$, *Slope (std)* with $|\hat{\beta}| = 0.51$, *VRM (avg)* with $|\hat{\beta}| = 0.30$, *Area SU* with $|\hat{\beta}| = 0.23$, *Prof Cur (std)* with $|\hat{\beta}| = 0.22$ and *VRM (std)* with $|\hat{\beta}| = 0.12$.

Similar to the max case, for the Sum model the rank and sign of the fixed effects can be easily read from a geomorphological standpoint, with the exception of *VRM (avg)*.

5.3 Non-linear Covariate Effects

Figure 6 displays all the non–linear (or random) covariates' effects featured in our model, by plotting the estimated coefficients in terms of posterior mean and Bootstrap-based 95% credible intervals. Two panels (top row and bottom left) report covariates that have been used in a purely categorical form, *i.e.*, with class effects being mutually independent *a priori*. The remaining panel (bottom right) shows the covariate *Slope (avg)* being used as an ordinal variable with an adjacent inter-class dependency driven by a random walk (see Section 4.1).

The *Earthquake Inventories* multiple intercepts (Figure 6a) show a complex and varying behavior. To interpret this panel, the regression constants are site–specific indices of differences in landslide area response to the ground motion. In other words, with respect to the mean landslide area across the whole dataset we used, the values reported here lead to variations in landslide size typical of specific landscapes. For instance, at a preliminary visual examination, the Gorkha earthquake clearly stands out with the smallest mean regression constant out of the 25 cases; the largest posterior mean is associated to the Guatemala earthquake. Finally, few earthquakes inventories are aligned along the zero line. In other words, they display no positive nor negative anomaly with respect to the average landslide size of all 25 cases combined. More details and an extensive interpretation of these results will be provided in Section 6.

A much simpler situation prevails for the Landforms (Figure 6b). In fact, no landform class appears to be significant in our case and they all lay along the zero line, indicating a negligible effect onto the final model. We will discuss this in Section 6.

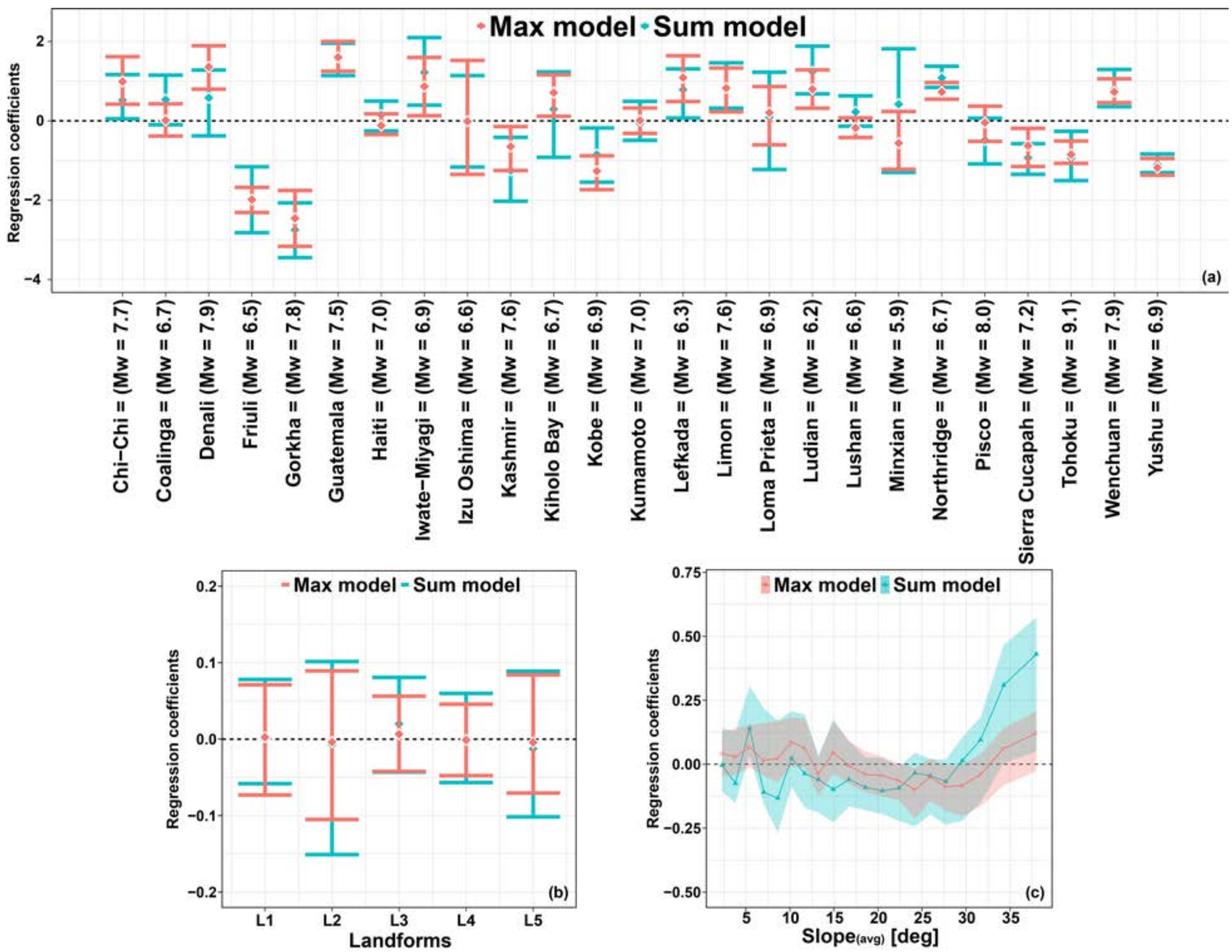

Figure 6: Random effects for the Max and Sum models: earthquake inventories (top), landform classes (bottom left), and *mean slope* (Slp, bottom right). For the earthquake inventories and landform classes, the dots show the posterior mean, while the segments correspond to the Bootstrap-based 95% credible intervals. For *mean slope*, the curves show the posterior mean, while the shadowed polygons correspond to the Boostrap-based 95% credible intervals. In all the plots, the black horizontal dashed line indicates zero (*i.e.*, no contribution to the landslide sizes).

The *Slope (avg)* panel (Figure 6c) shows a clear nonlinear behavior both in the Max and Sum models. SUs with an average steepness up to approximately 25 degrees do not contribute to vary the estimated landslide size. From this threshold to larger steepness values, the Max model shows a mild increase in the *Slope (avg)* regression coefficients, whereas the Sum model also increases but with a much steeper trend.

5.4 Landslide Area Results

In this section we briefly report the posterior estimates of the mean predicted landslide areas (for both Max and Sum models) with respect to the uncertainty computed without accounting for potential spatial dependencies and via a spatial Bootstrap where the uncertainty is more realistically estimated. This is shown in Figure 7 where our simpler implementation in INLA largely underestimates the uncertainty around the mean landslide sizes, both in the case of the Max and Sum models.

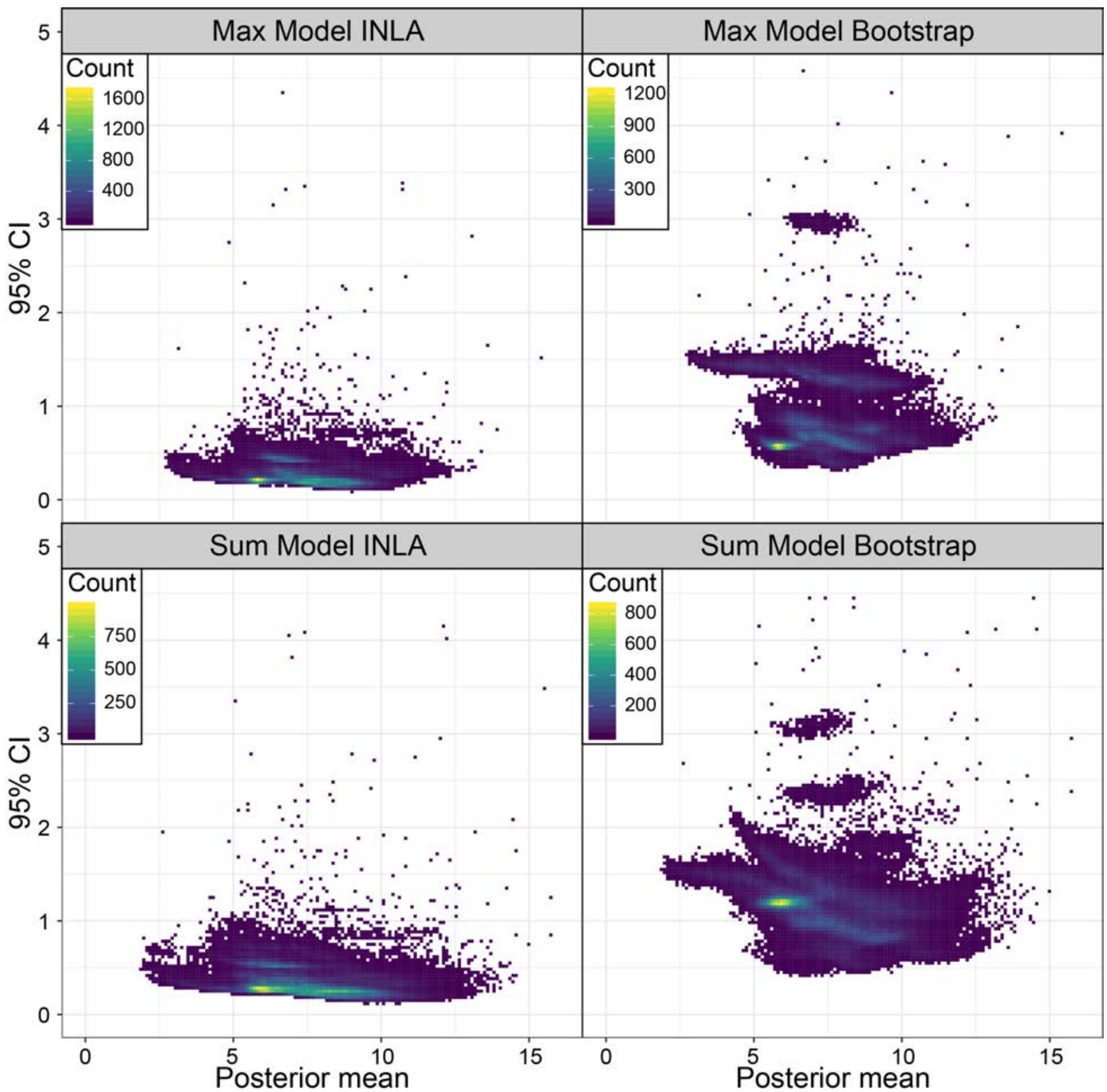

Figure 7: Two-dimensional histogram of the posterior mean landslide $\log(A_L)$ plotted against its 95% credible interval. The uncertainty values computed with INLA (left) and with the spatial Bootstrap (right) are shown both for the Max (top) and Sum (bottom) models.

5.5 Landslide Area Classification

We opt to translate the model results in map form following two approaches. The first one is simply to display the $\log(A_L)$ observations and estimates in their original continuous scale. The second approach introduces a classification step in our mapping procedure which is graphically summarized in Figure 8. Specifically, we start by computing the best fit line in a two-dimensional space defined between observed and predicted landslide areas. From the observed cases we compute four quantiles at specific intervals ($\tau = 0.05$, 0.25, 0.75 and 0.95). The observed landslide area (be it Max or Sum) values associated with each of the quantiles are then projected to the predicted landslide areas by intersecting the best fit line. As a result we are able to also show a common classification scheme for Very Small (VS), Small (S), Medium (M), Large (L) and Very Large (VL).

It is important to note that there were several options. For instance, any GIS environment generally offers the option to visualize spatial data by cutting off values above and below a certain standard deviation. This could have helped us to improve the visual agreement between observed and predicted landslide sizes. In fact, our model tends to overestimate the left tail of the $\log(A_L)$'s distribution and underestimate its right tail. However, we chose to keep the data intact to highlight strengths and weaknesses. The opposite situation could have taken place if we would have classified according to two separate boxplots, one for each axis. This would have maximized the differences driven by the log-Gaussian approximation. Therefore, we chose an intermediate option which we believe to be fair and representative enough of the model performance converted into map form.

5.6 Landslide Size Predictive Mapping

In this section we geographically translate and report the outcome of our modelling framework. However, because we modelled 25 EQIL inventories, showing each corresponding figure would have overly lengthened the manuscript. Therefore, we chose to provide two examples where our Max and Sum models performed well (Haiti and Wenchuan), two examples where our Max and Sum models produced acceptable performance (Lushan and Northridge), and two examples where we find a poor agreement between observed and predicted Max and Sum landslide sizes (Gorkha and Chi–Chi). The remaining 19 cases are separately provided in the Supplementary Material for clarity, both for the Max and Sum models.

Each of the six figures introduced above contains the following information:

1. Observed landslide area map using continuous values.
2. Predicted landslide area map using continuous values.
3. Observed landslide area map using the classification explained in Section 5.5.
4. Predicted landslide area map using the classification explained in Section 5.5.

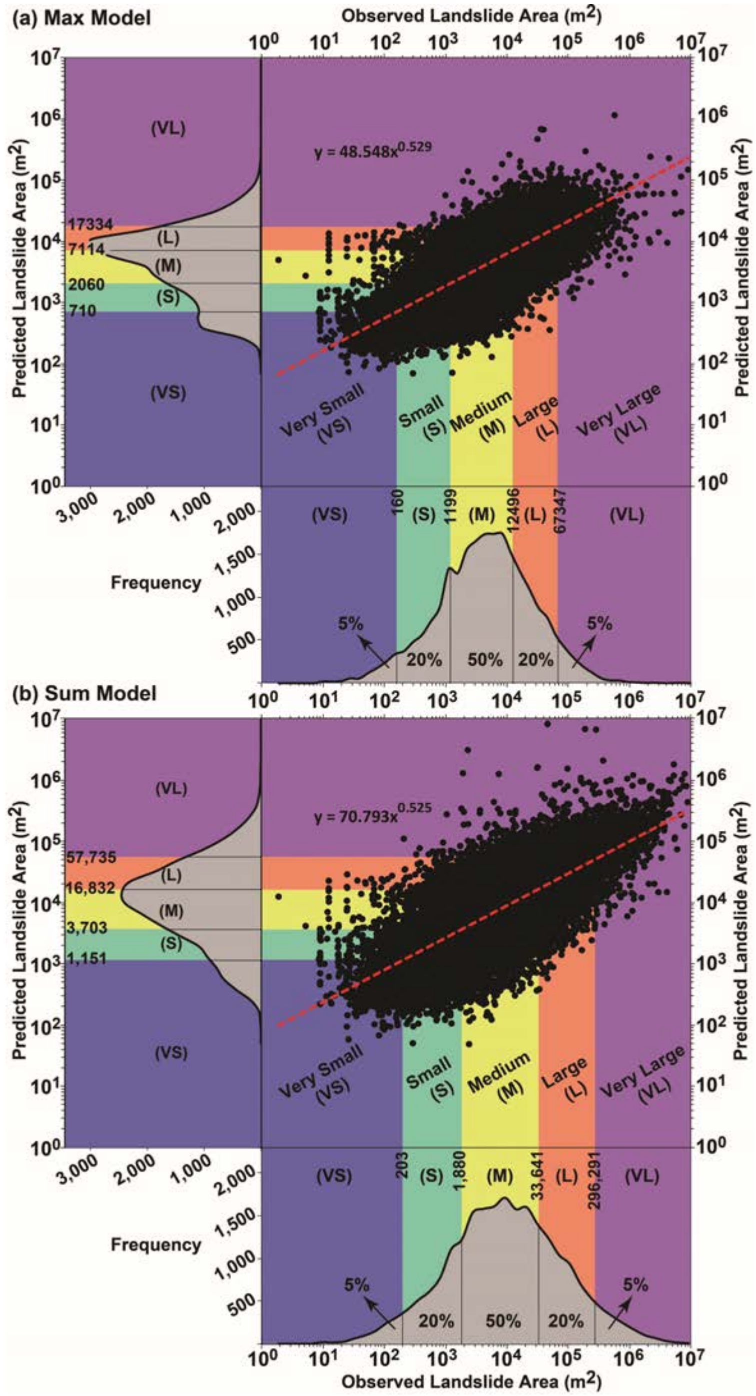

Figure 8: Observed vs. predicted landslide areas shown together with the classification scheme implemented to create a suitable colorbar for mapping. The density plots show the common classification for Observed vs. predicted landslide areas.

5. 95% credible interval measured by subtracting the SU-wise 97.5 and the 2.5 percentiles obtained with INLA (see Section 4.4).

6. 95% credible interval measured by subtracting the SU-wise 97.5 and the 2.5 percentiles obtained via Bootstrap (see Section 4.2).

In summary, Figures 9 and 10 show our proposed mapping procedure for Haiti, for Max and Sum models, respectively. In both cases, panels a and b show a strong agreement overall, with the exception of the NW sector where predicted landslide sizes are underestimated with respect to the observed counterpart. Our classification (panels c and d) produces a better match between the two maps. Furthermore, the uncertainty around the prediction (panels e and f), which is realistically higher in the bootstrap case, is relatively low with the exception of a few number of large SUs.

Similarly, Figures 11 and 12 correspond to the Wenchuan case. The pattern of the predicted landslide sizes (both for Max and Sum models) is extremely close to the pattern shown for the corresponding observed cases, this being valid both on the continuous scale (panels a and b) and in the classified maps. This is a quite remarkable agreement between observed and predicted cases although the latter tends to slightly overestimate the former. Both for Max and Sum models, the 95% credible intervals show quite reasonable bootstrapped values both in spatial distribution and amplitude with respect to the original scale.

Landslide sizes predicted for the Lushan case are shown in Figures 13 and 14. Here our model slightly underestimates the observed landslide area per SU, both for the Max and Sum models, although the overall pattern is generally respected. The underestimation mainly affects the right tail of the max and sum $\log(A_L)$ distributions whereas a minor overestimation affect small landslide sizes concentrated in the left tail. This is associated with relatively high uncertainty bootstrap levels.

Northridge, shown in Figures 15 and 16, depicts an analogous situation over space between the observation and our prediction, with very few SUs singled out because of a mismatch (generally an overestimation). However, despite the mismatch between observed and predicted values for the tails, the main bulk of the distribution is modelled correctly.

Figures 17 and 18 display the estimated landslide size over space for Chi–Chi. The island of Taiwan has a rough topography, thus the prediction covers the whole island showing a reasonable pattern both for the Max and Sum models. However, the comparison between the classified landslide sizes shows a situation where the model tends to slightly overestimate the original size class. Notably, this is much more evident for the Max model rather than its Sum counterpart. The estimation is generally larger by one class or, in other words, where the original data shows medium landslide extents the model predict a large counterpart and where the observed landslide is large our model assigns a very large landslide class. This relatively low performance is reflected in the bootstrapped uncertainty levels where the size of the 95% credible interval is generally larger than the corresponding observed landslide size.

The worst case among the 25 we examined corresponds to the Gorkha earthquake (see Figures 19 and 20). Here the Max and Sum models produce different performances where the Max one tends to generally underestimate the observed landslide size. As for the Sum model, here the bulk of the observed landslide size distribution is well represented, although the left tail is overestimated and the right tail is underestimated. Therefore, the general spatial pattern is similar between observed and predicted cases, with an upward or downward shift in the predicted classes due to under/overestimation issues. Here the bootstrapped uncertainty range is again relatively high with slightly higher 95% credible interval compared to the corresponding observed landslide size.

A deeper interpretation is provided in Section 6.

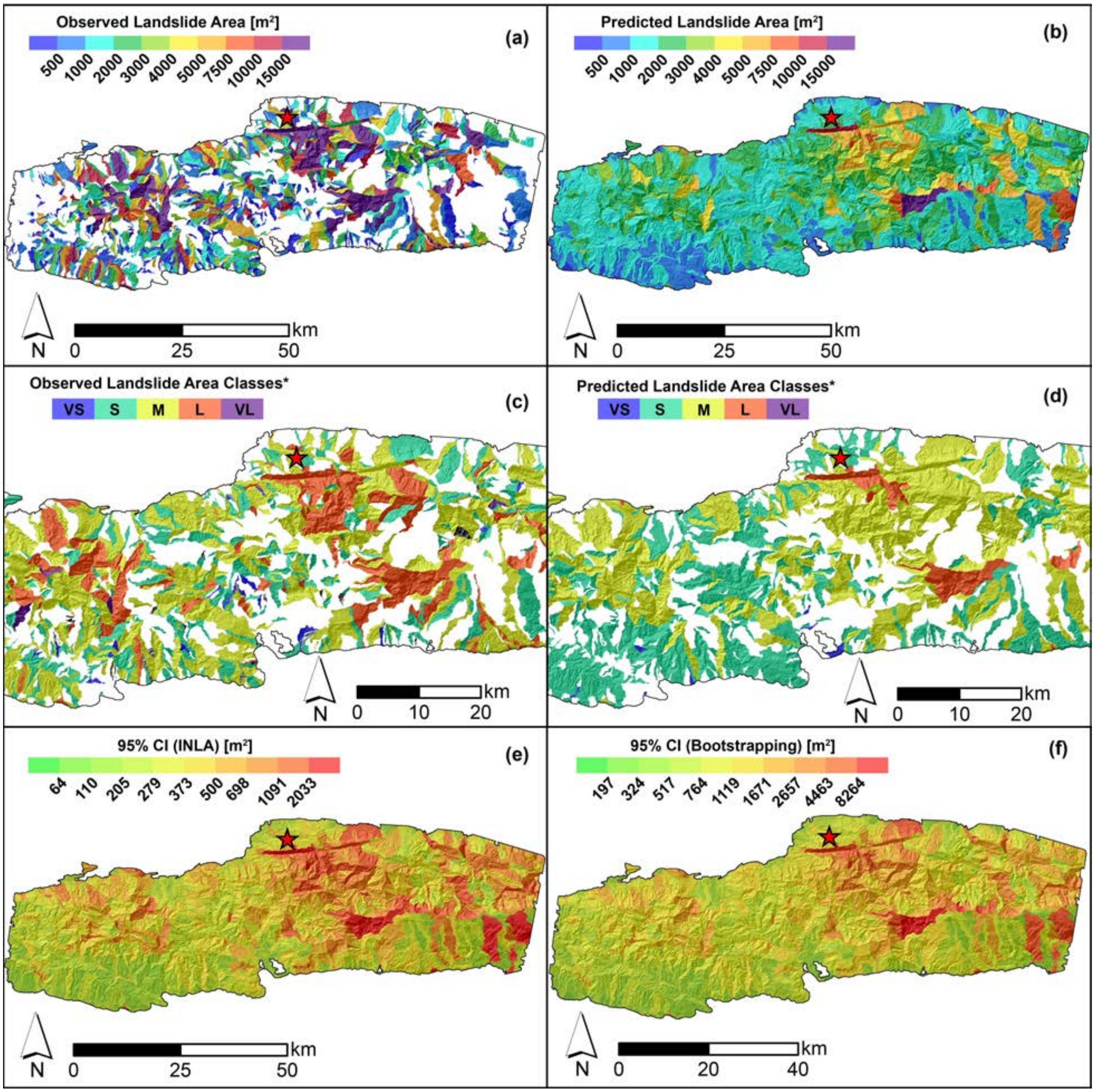

Figure 9: Excellent agreement example for Haiti Max maps: (a) Observed maximum landslide area per SU. (b) Predicted maximum landslide area per SU. (c) Classified observed maximum landslide area per SU. (d) Classified predicted maximum landslide area per SU. (d) 95% credible interval estimated with INLA. (e) 95% credible interval estimated via bootstrap.

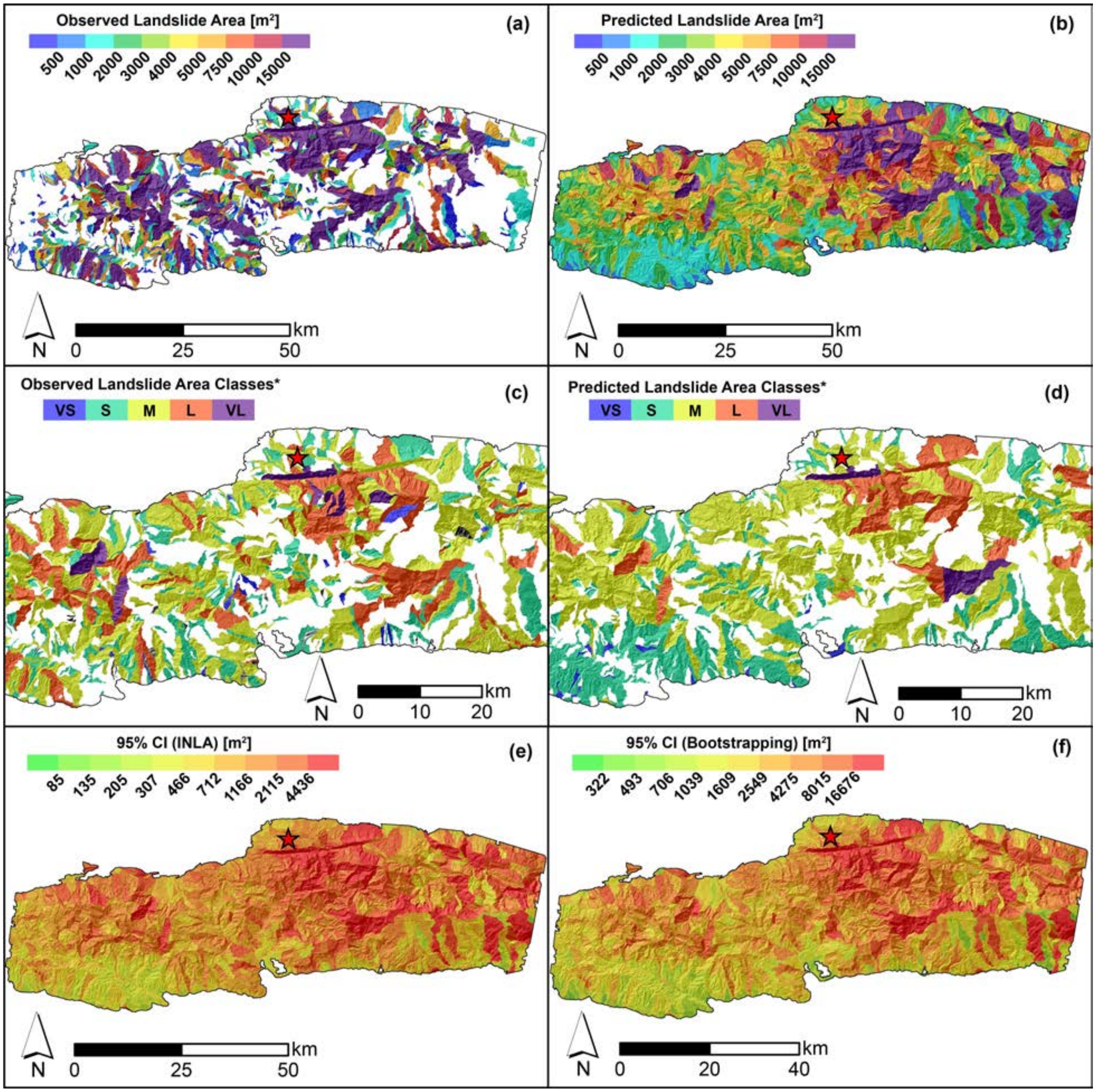

Figure 10: Excellent agreement example for Haiti Sum maps: (a) Observed summed landslide area per SU. (b) Predicted mean of summed landslide area per SU. (c) Classified observed sum of landslide area per SU. (d) Classified predicted mean of summed landslide area per SU. (d) 95% credible interval estimated with INLA. (e) 95% credible interval estimated via bootstrap.

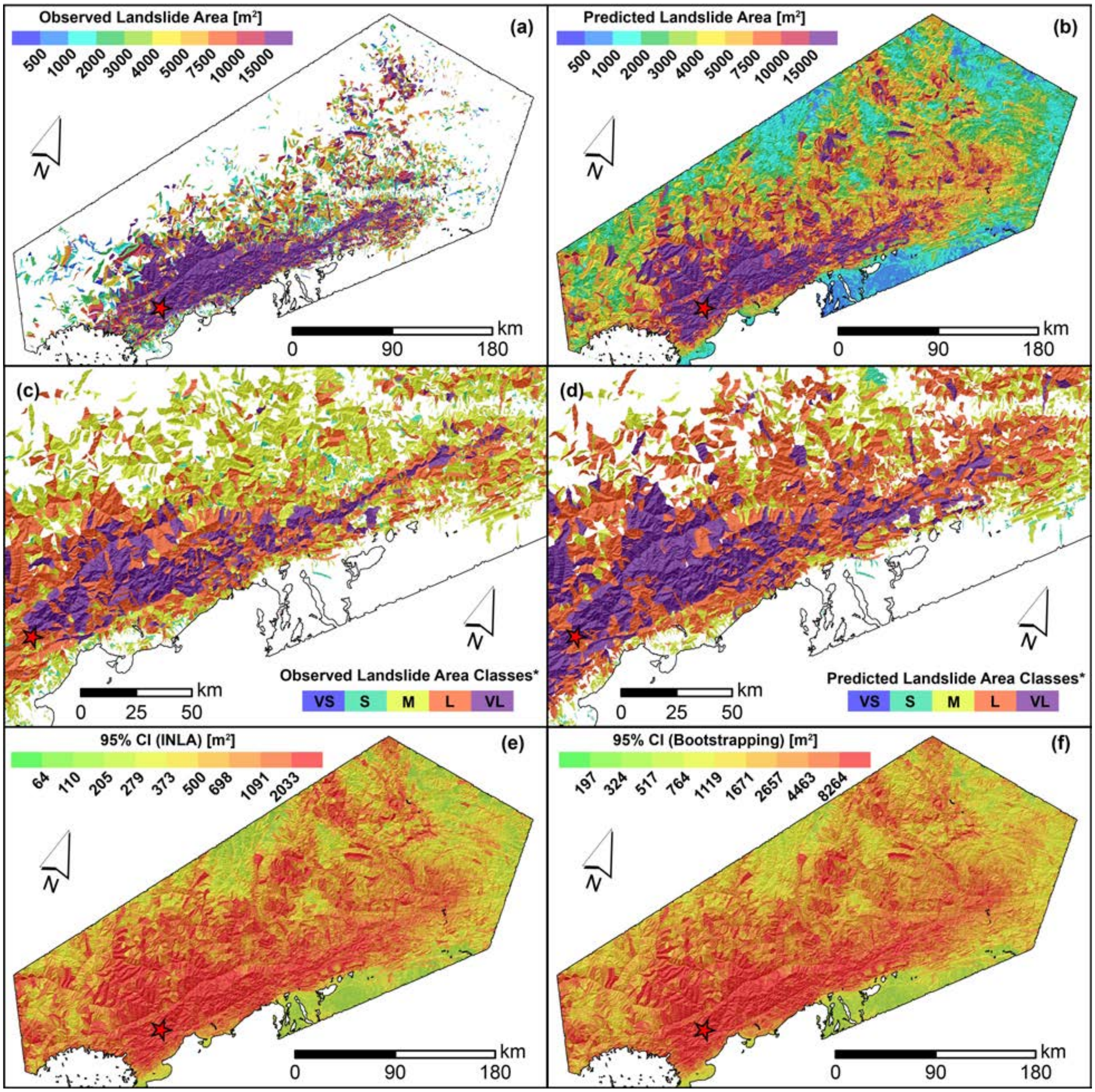

Figure 11: Excellent agreement example for Wenchuan Max maps: (a) Observed maximum landslide area per SU. (b) Predicted maximum landslide area per SU. (c) Classified observed maximum landslide area per SU. (d) Classified predicted maximum landslide area per SU. (d) 95% credible interval estimated with INLA. (e) 95% credible interval estimated via bootstrap.

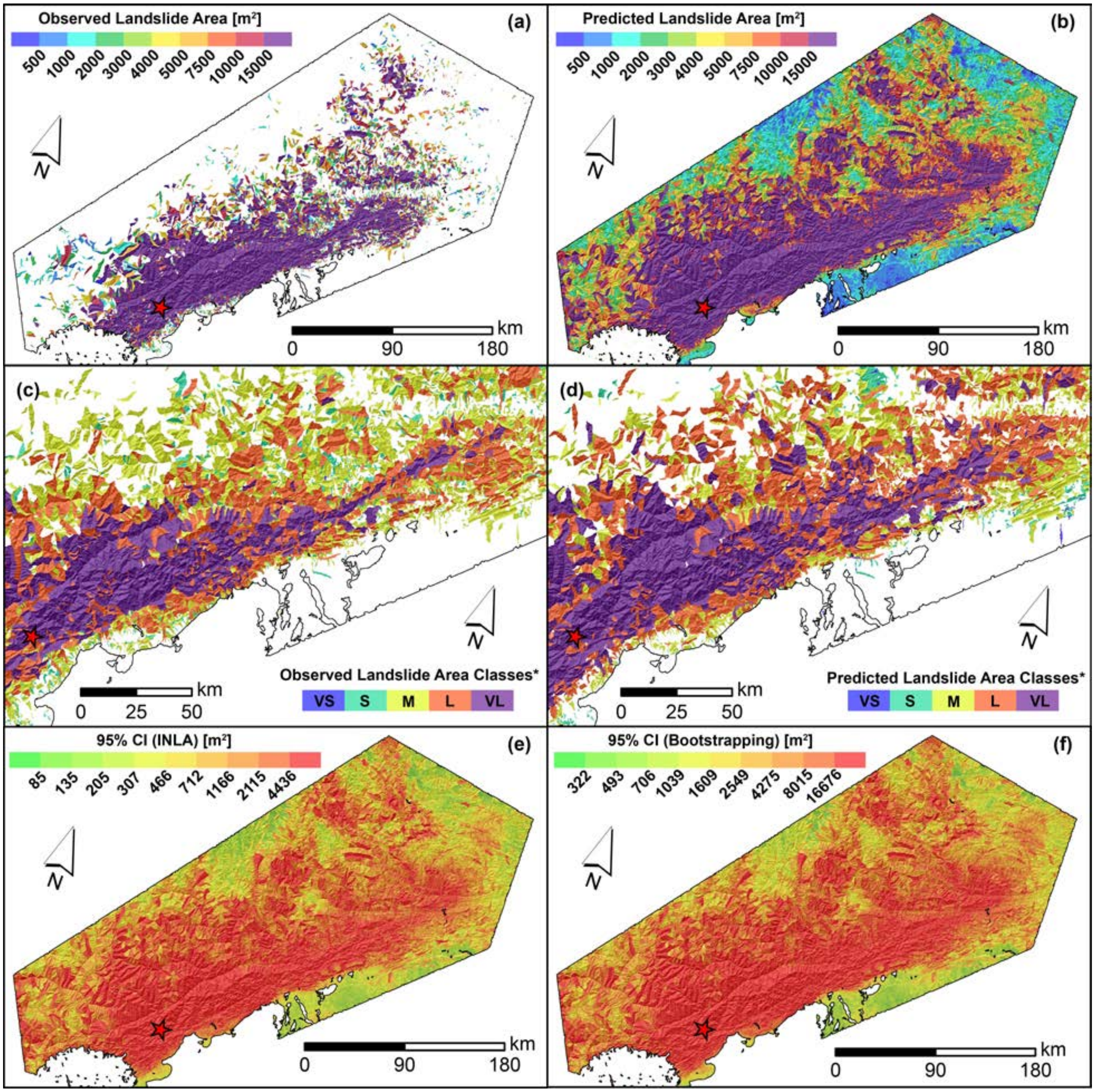

Figure 12: Excellent agreement example for Wenchuan Sum maps: (a) Observed summed landslide area per SU. (b) Predicted mean of summed landslide area per SU. (c) Classified observed sum of landslide area per SU. (d) Classified predicted mean of summed landslide area per SU. (d) 95% credible interval estimated with INLA. (e) 95% credible interval estimated via bootstrap.

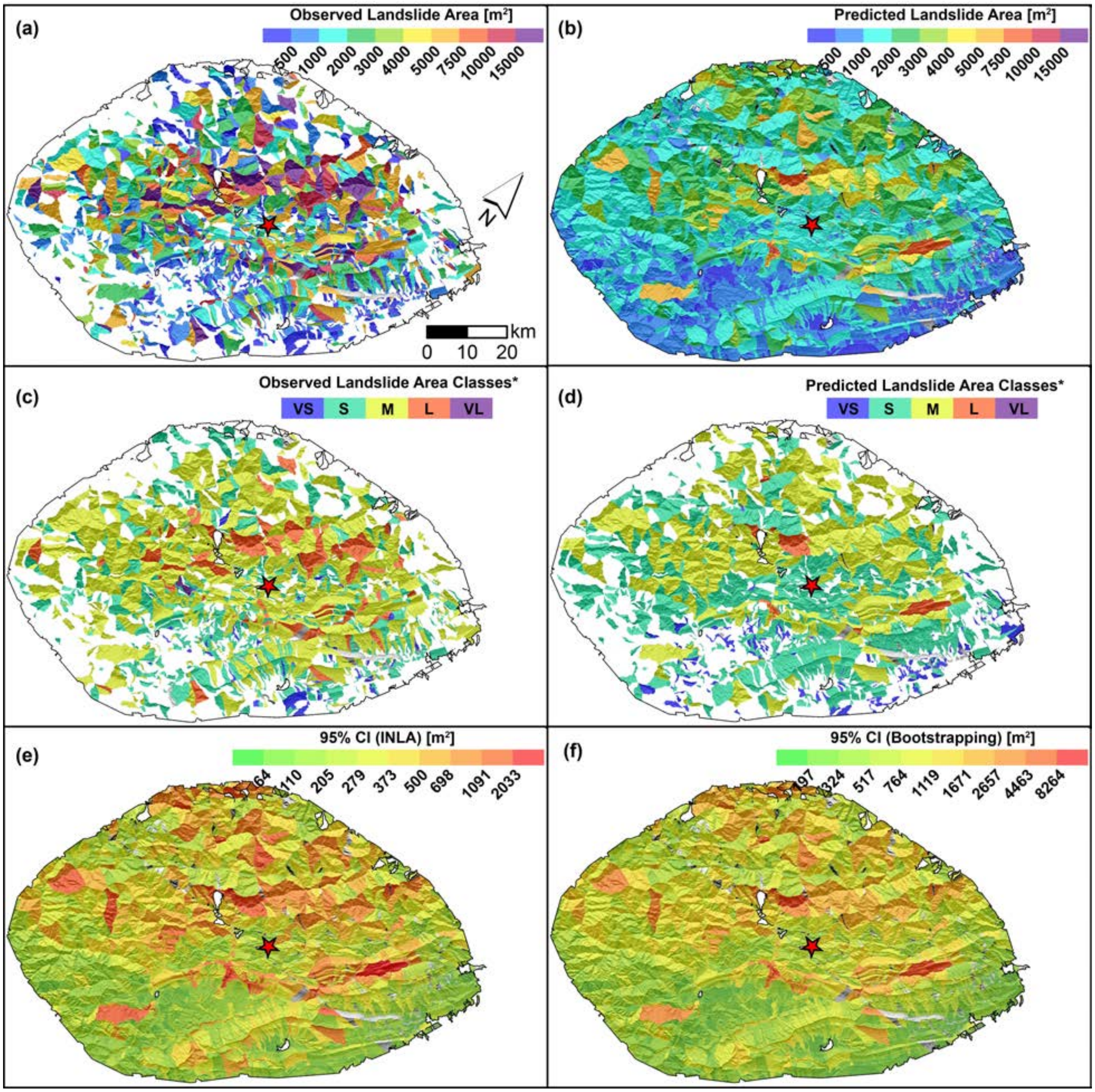

Figure 13: Good agreement example for Lushan Max maps: (a) Observed maximum landslide area per SU. (b) Predicted maximum landslide area per SU. (c) Classified observed maximum landslide area per SU. (d) Classified predicted maximum landslide area per SU. (d) 95% credible interval estimated with INLA. (e) 95% credible interval estimated via bootstrap.

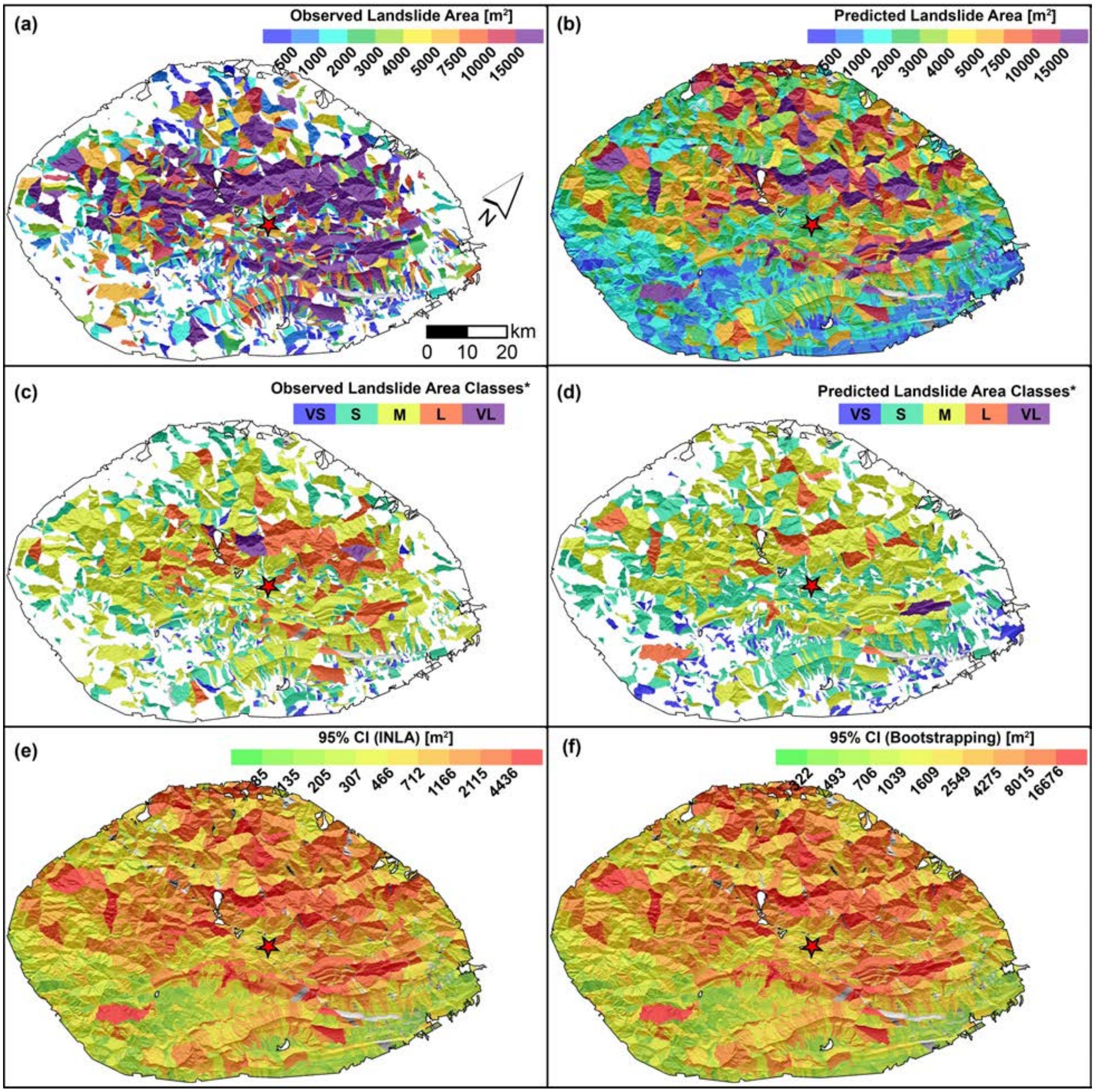

Figure 14: Good agreement example for Lushan Sum maps: (a) Observed summed landslide area per SU. (b) Predicted mean of summed landslide area per SU. (c) Classified observed sum of landslide area per SU. (d) Classified predicted mean of summed landslide area per SU. (d) 95% credible interval estimated with INLA. (e) 95% credible interval estimated via bootstrap.

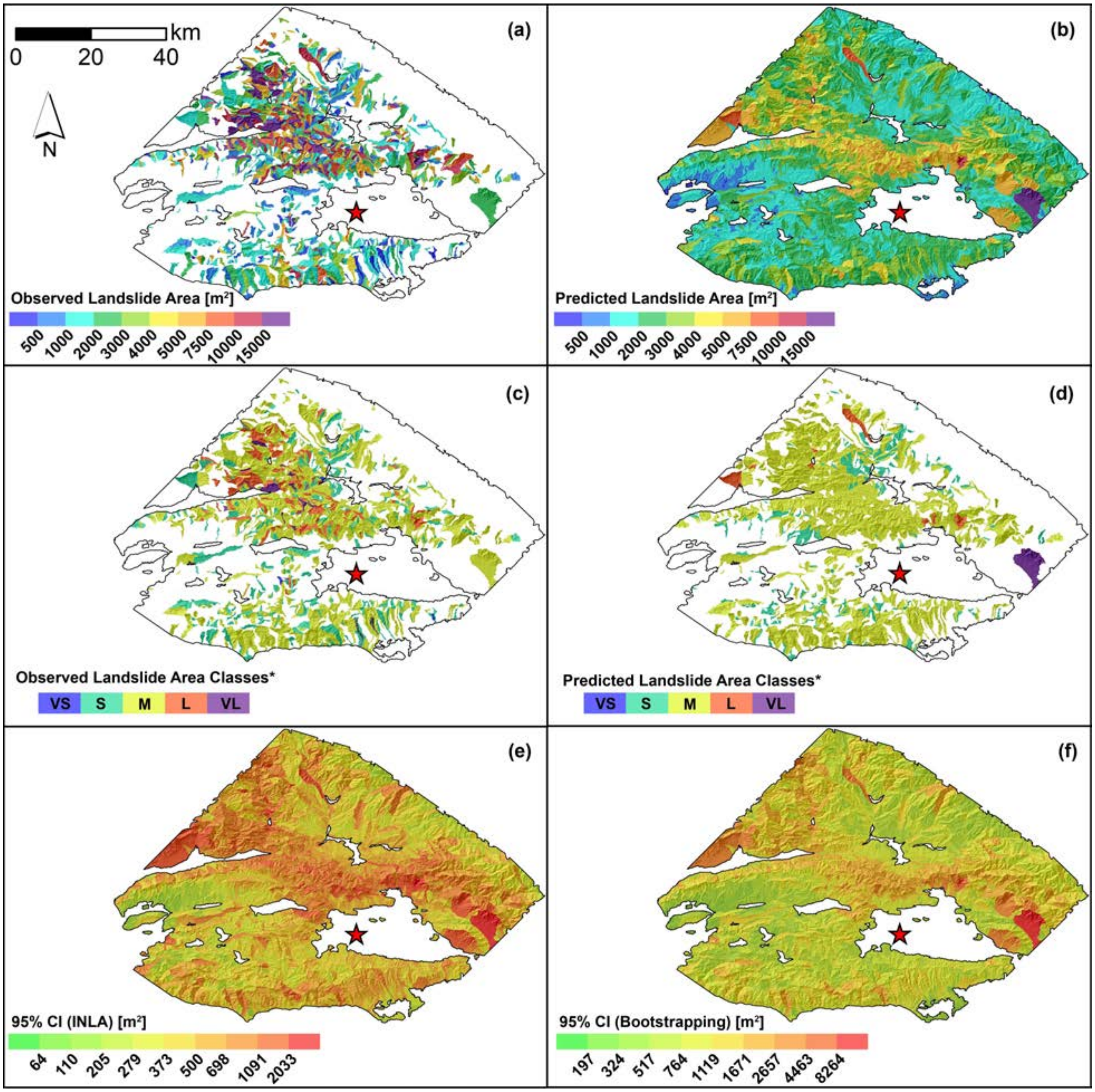

Figure 15: Good agreement example for Northridge Max maps: (a) Observed maximum landslide area per SU. (b) Predicted maximum landslide area per SU. (c) Classified observed maximum landslide area per SU. (d) Classified predicted maximum landslide area per SU. (d) 95% credible interval estimated with INLA. (e) 95% credible interval estimated via bootstrap.

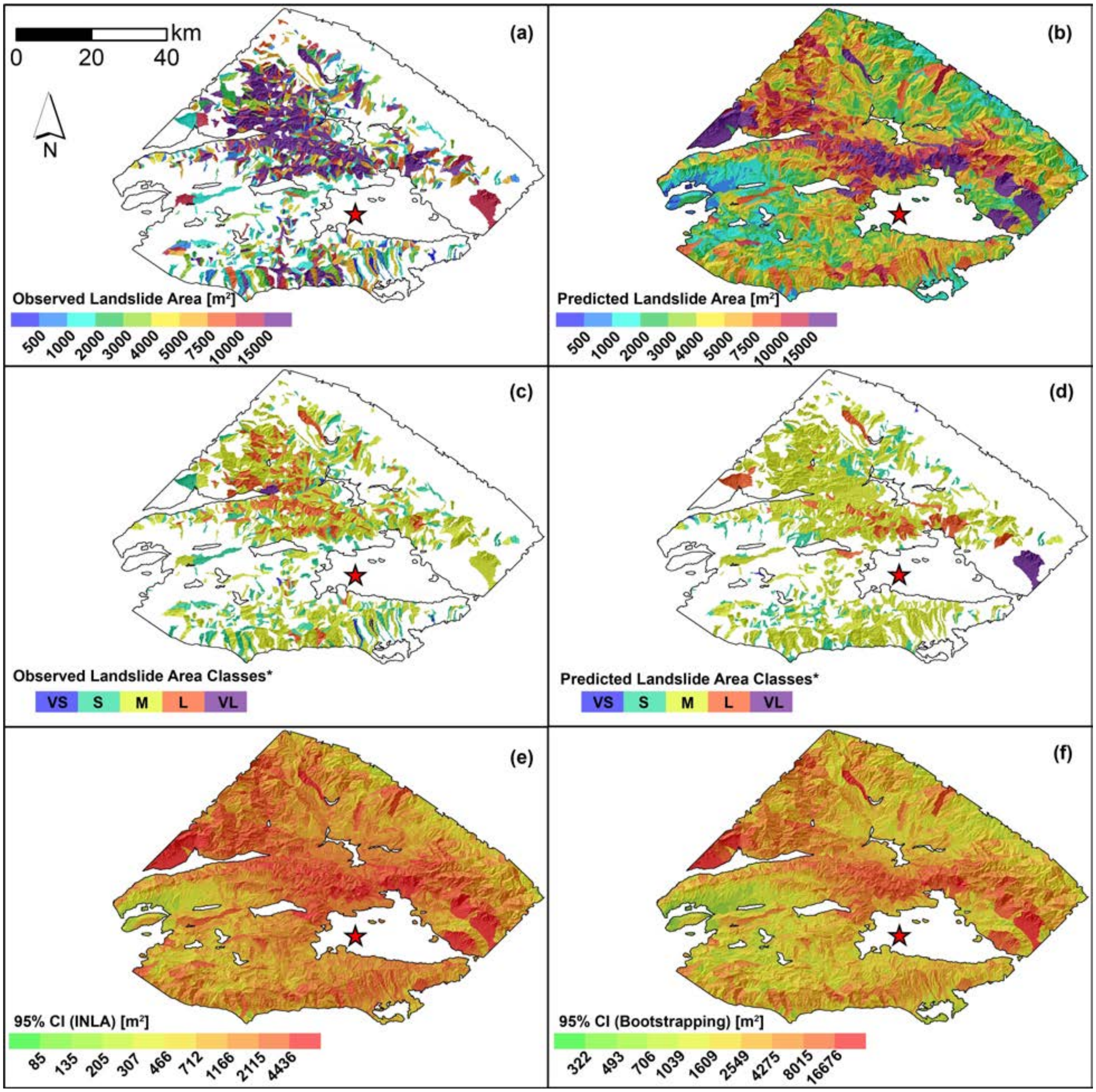

Figure 16: Good agreement example for Northridge Sum maps: (a) Observed summed landslide area per SU. (b) Predicted mean of summed landslide area per SU. (c) Classified observed sum of landslide area per SU. (d) Classified predicted mean of summed landslide area per SU. (d) 95% credible interval estimated with INLA. (e) 95% credible interval estimated via bootstrap.

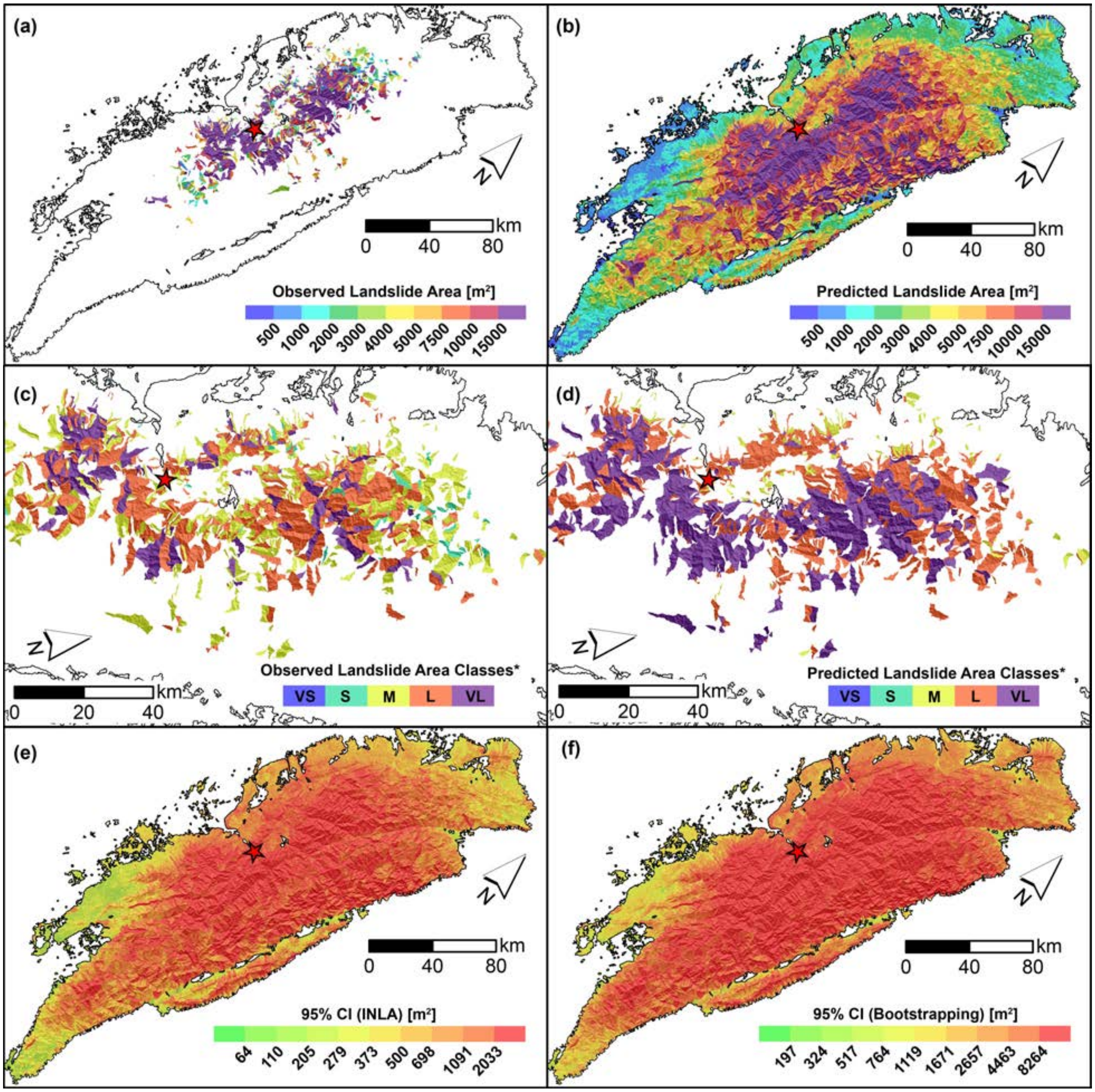

Figure 17: Acceptable agreement example for Chi–Chi Max maps: (a) Observed maximum landslide area per SU. (b) Predicted maximum landslide area per SU. (c) Classified observed maximum landslide area per SU. (d) Classified predicted maximum landslide area per SU. (d) 95% credible interval estimated with INLA. (e) 95% credible interval estimated via bootstrap.

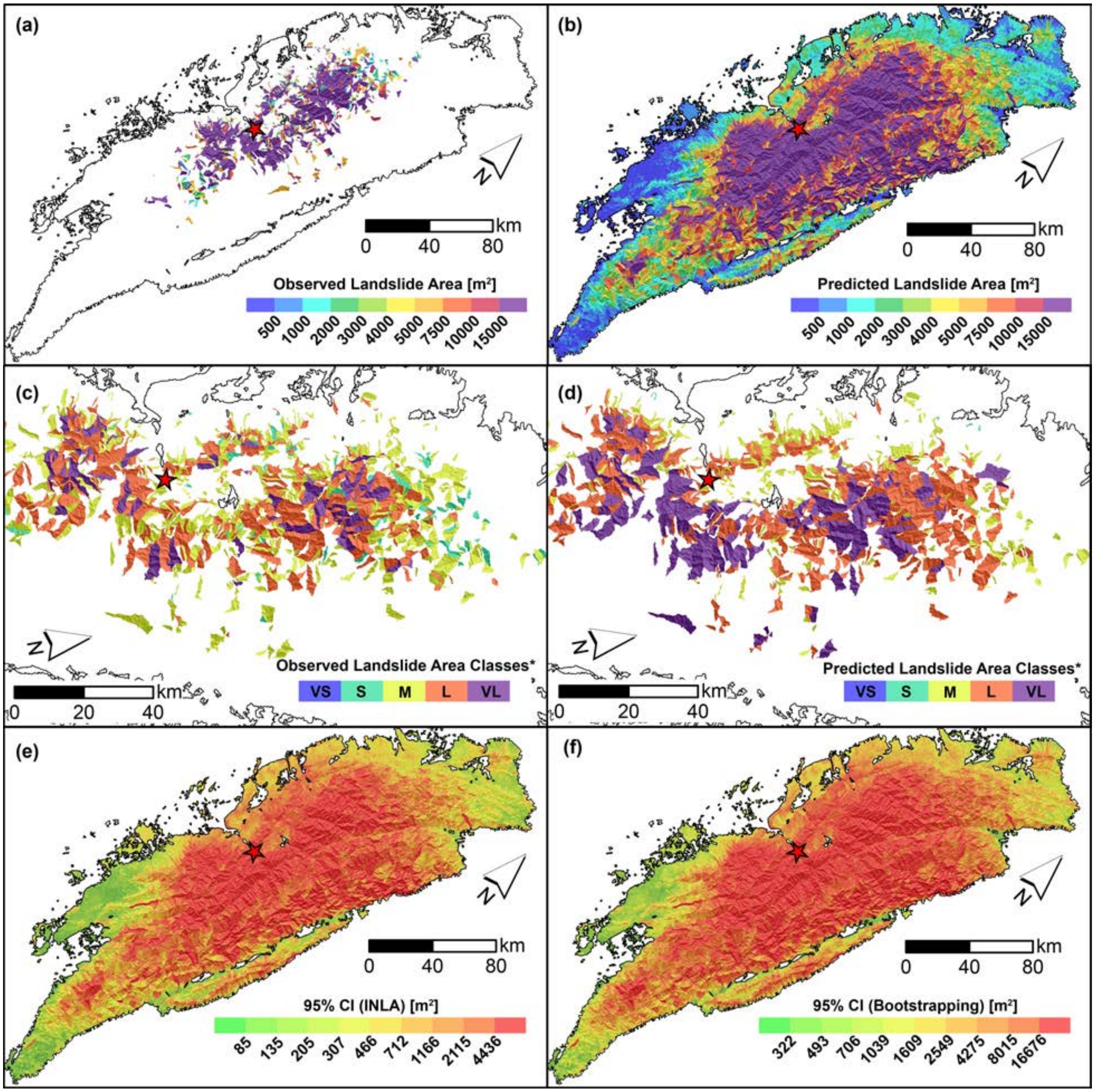

Figure 18: Acceptable agreement example for Chi–Chi Sum maps: (a) Observed summed landslide area per SU. (b) Predicted mean of summed landslide area per SU. (c) Classified observed sum of landslide area per SU. (d) Classified predicted mean of summed landslide area per SU. (d) 95% credible interval estimated with INLA. (e) 95% credible interval estimated via bootstrap.

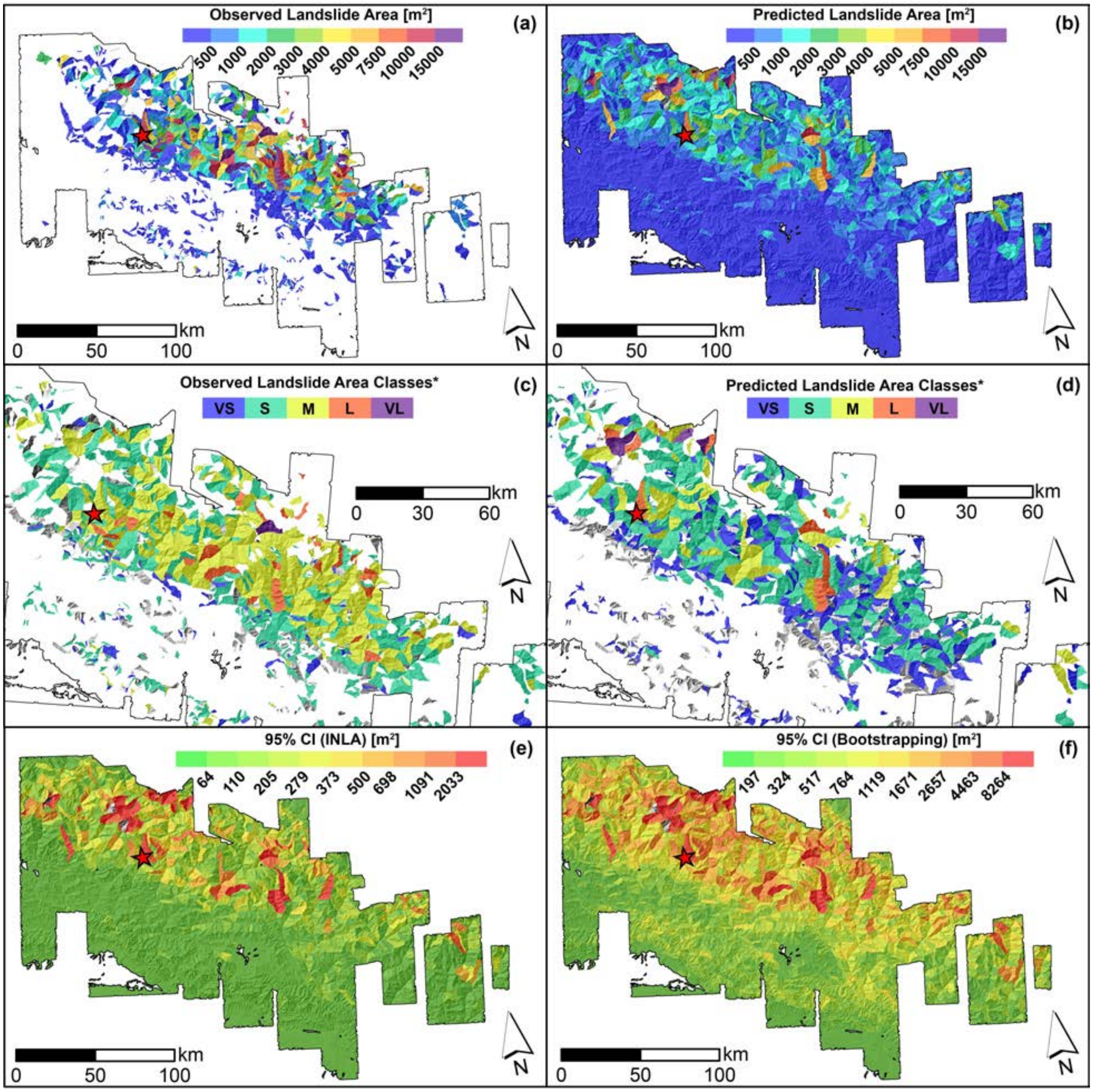

Figure 19: Acceptable agreement example for Gorkha Max maps: (a) Observed maximum landslide area per SU. (b) Predicted maximum landslide area per SU. (c) Classified observed maximum landslide area per SU. (d) Classified predicted maximum landslide area per SU. (d) 95% credible interval estimated with INLA. (e) 95% credible interval estimated via bootstrap.

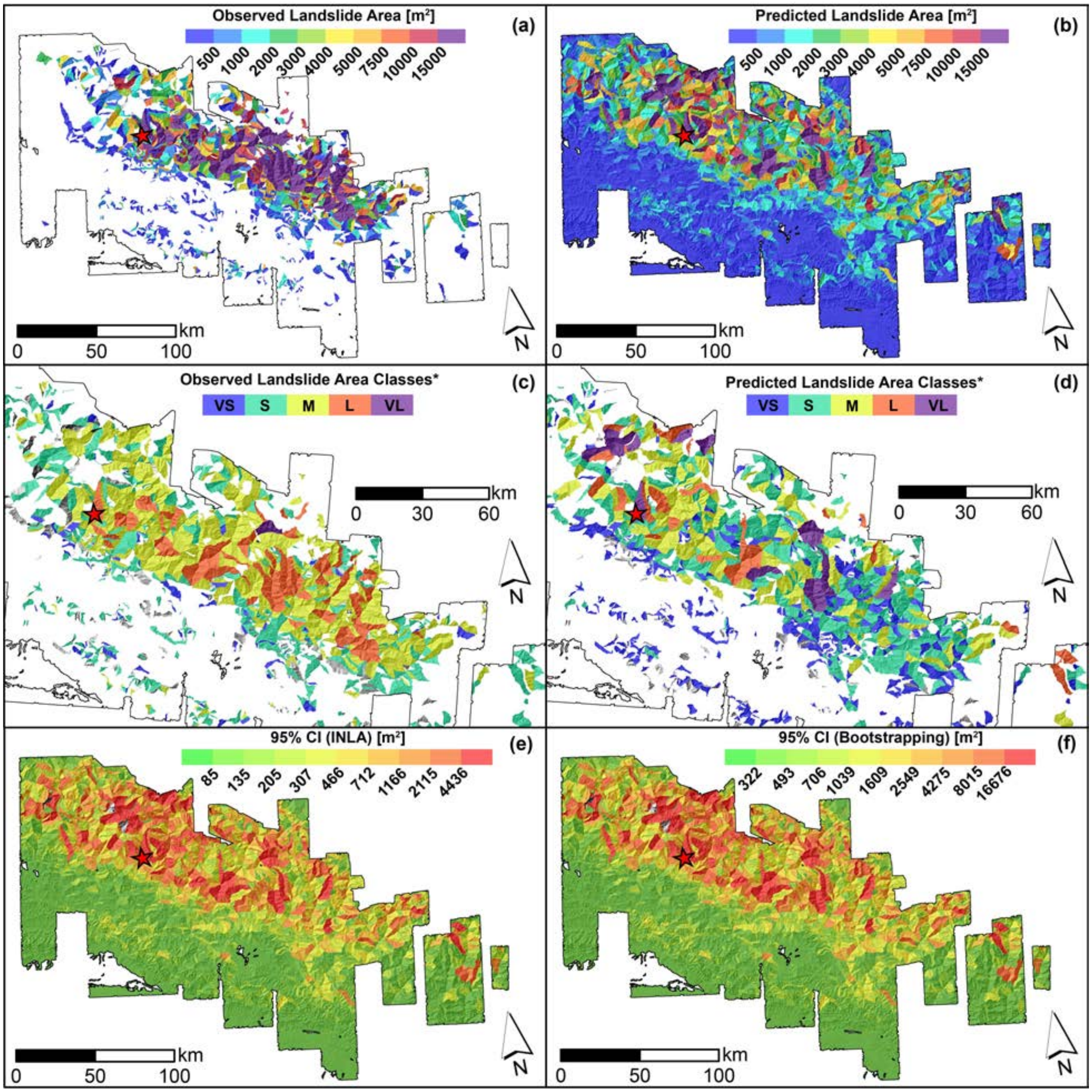

Figure 20: Acceptable agreement example for Gorkha Sum maps: (a) Observed summed landslide area per SU. (b) Predicted mean of summed landslide area per SU. (c) Classified observed sum of landslide area per SU. (d) Classified predicted mean of summed landslide area per SU. (d) 95% credible interval estimated with INLA. (e) 95% credible interval estimated via bootstrap.

6 Discussion

This section is meant to provide the reader with an interpretation of the modelling protocol we present as well as to share our views on its limitations and strengths. The following sections will focus on one element at a time and will be concluded with our future plans for further extensions.

6.1 Performance Overview

Our Log-Gaussian model of planimetric landslide areas is a global model, thus it may perform differently for each of the considered earthquakes. And yet, both Max and Sum models are generally able to characterize the $\log(A_L)$ distributions in each of the 25 study sites. We summarized this information in Figure 21.

We recall here that the performance of both Max and Sum models appears to be quite satisfactory also when this information is graphically shown for the whole landslide size dataset (see also Figures 8 and 4) or geographically shown for specific sites (see Figures from 9 to 20). These predictive maps visually and intuitively demonstrate how the observed and predicted $\log(A_L)$'s patterns match. To provide a numerical overview of the models' performance for each of the 25 earthquakes, in Figure 22 we also show the agreement among observed and predicted landslide sizes, after we performed the classification explained in Section 5.5. In this figure, we show that despite the Max and Sum models generally agree, the classified landslide size per earthquakes may be misrepresented. This is the case of Coalinga, Minxian and Yushu, both for Max and Sum models. These specific events show the least agreement among classes with a perfect match between observed and predicted being confined below 30%. Besides, the slight under- or over- estimation demonstrated by a single shift in class is larger than 50% and the large under- or over- estimation demonstrated by a two (or more) class shift characterizes 20% of the predicted landslide size.

These three cases clearly represent the worst prediction our Max and Sum models produced. Similarly, we can also highlight three earthquakes for which our models perform very well. This is the case for Loma Prieta, Limon and Izu Oshima where the two (or more) class shift characterizes less than 1% of the prediction, the one class shift corresponds to less than 45% and the perfect match is found in more than 55% of the SUs.

This overview provides a better summary of the models we propose. It certainly suggests that our models are quite performing but also that some improvements could still be achieved, possibly improving the quality of the data, the scale at which the models are built and the model structure. Each of these elements will be discussed in the following sections.

6.2 Interpretation of the covariates' role

For a model to be operational, good performances are not the only requirement. Each model component should be interpretable and make sense from a geomorphological standpoint.

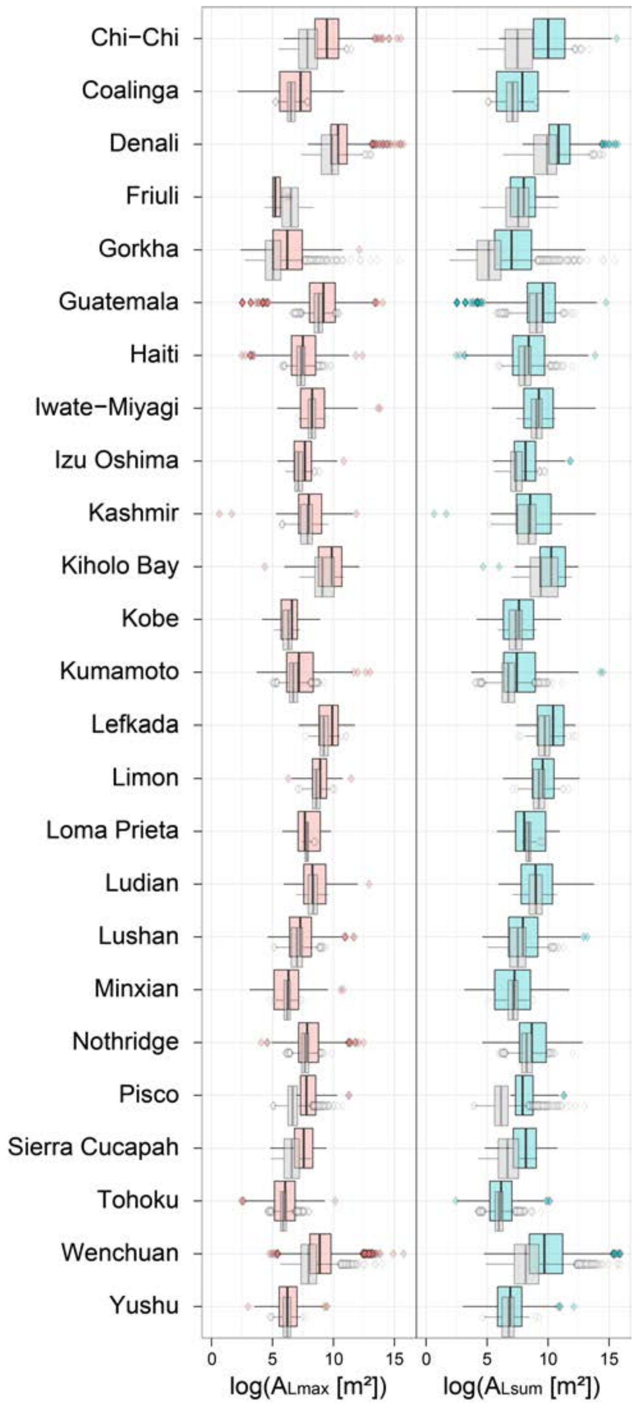

Figure 21: Distribution of the posterior mean of landslide sizes per SU, for the Max (pink boxplots) and Sum (cyan boxplots) models. The grey boxplots correspond to the observed $\log(A_L)$.

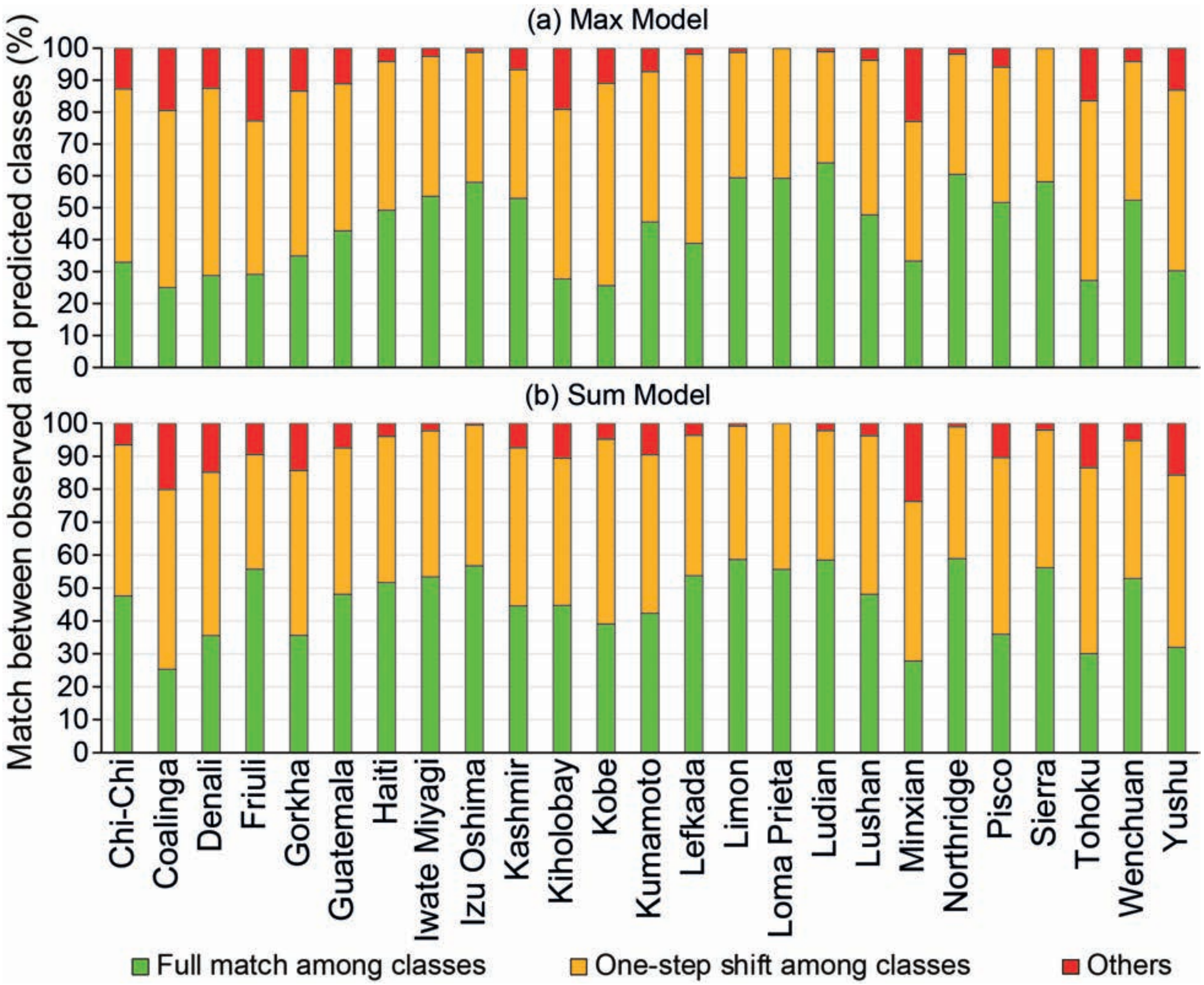

Figure 22: Stacked barplot reporting the percentage of cases—with respect to the total for each earthquake—for which the observed and predicted classes of landslide area coincide (green), are shifted by a single class (orange) and are shifted by two classes (red).

Here we examine how reasonable our Max and Sum models are on the basis of the estimated regression coefficients' distribution.

As briefly anticipated in Section 5.2, the fixed effects appear to be geomorphologically sound, with the exception of the *VRM (avg)*. Both for the Max and Sum models, the mean Macroseismic Intensity (MI) per SU is the largest contributor (in the Sum model case, it has a much larger posterior mean value). This may indicate that the ground motion not only plays an important role in explaining any landslide size but it may imply the *MI (avg)* is even more crucial to estimate very large aggregated landslide sizes per SU, which are part of the Sum model rather than the Max model. Similar considerations can be found in, *e.g.*, Keefer and Manson (1998) and Massey et al. (2018), where the authors mentioned a similar relation by assuming that the intensity of the ground motion decreases as a function of the distance to the rupture zone. Similarly, the *Relief rng (avg)* appears to be the second largest contributor both for the Max and Sum models. More specifically, its effect onto the landslide size estimates is equivalent to the *MI (avg)* for the Max model case and it is 24% smaller than the contribution of the *MI (avg)* in the Sum model case. This can be interpreted in terms of topographic control on landslide sizes. For the Max model, the potential gravitational energy expressed by the relief is able to explain the landslide size as much as the trigger itself (*MI (avg)*). In the Sum model, although the relief is still fundamental to estimate A_{Lsum}, its contribution is ranked second overall, likely because extremely large landslide sizes do require an exceptional seismic stress to be triggered. High relief may be interpreted as a sign of relatively strong rock mass properties constituting the hillslope materials (Schmidt and Montgomery, 1995; Townsend et al., 2020) and yet the positive contribution can be linked to the higher potential gravitational energy and longer runout associated with hillslopes with high relief. Similar considerations can be found in Medwedeff et al. (2020) where the authors emphasize how much hillslope relief is crucial to control landslide sizes.

Another reassuring covariate contribution can be seen for the *Slope (std)*, both for the Max and Sum models. The variation of the steepness inside a given SU can be intuitively interpreted as a proxy for topographic roughness. For instance, if the mean steepness per SU is 40 degrees but the standard deviation is close to zero, then the whole slope unit would certainly be steep but its surface would be smooth. Conversely, in the case where the mean steepness per SU is 40 degrees but the standard deviation is 20 degrees, then one should expect the SU surface to be rough and likely hummocky at times. Such a surface should offer a bumpy landscape upon which the ground motion can act to mobilize unstable material. As a result, a significant and positive coefficient estimated for *Slope (std)* appears to be reasonable for the larger the roughness, the more available potentially unstable material should be, hence the larger the resulting landslide. *Slope (std)* also appears as a positively contributing variable in studies assessing the susceptibility of rainfall- and earthquake-induced landslides (*e.g.*, Guzzetti et al., 2005a; Tanyaş et al., 2019a).

The fourth ranked covariate is more problematic. The *VRM (avg)* is an expression of topographic roughness. Therefore, one should expect a positive sign of the regression coefficient distribution, both for the Max and Sum models. However, the coefficient of *VRM (avg)* appears to be significant and negative overall, making any interpretation difficult to formulate. We believe this to be a case of a confounding covariate. In fact, although our variable selection step (see Section 4.1) included the *VRM (avg)*, this covariate still interacts with the others. Therefore, in case this covariate would share a similar signal to another one or more than one, its sign and amplitude of the regression coefficient will be influenced by other interactions. In the specific case, we believe *VRM (avg)* to be potentially interacting with more than one covariate that carries the topographic roughness information. For instance, not only the *Slope (std)* may play a similar role but also the two curvatures. In fact, the planar and profile curvatures are by definition summarizing how rough the given landscape is in two main directions. This is particularly exacerbated in case of a SU partition where we compute the mean and standard deviation for each morphometric property. In this sense, computing the standard deviation of the curvatures inside a given SU certainly stresses how rough the mapping unit is. Therefore, it can share a similar role with the *VRM (avg)*, which is estimated to be negative overall, to counterbalance different positive contributions for proxies of topographic roughness. To expand on this, both Max and Sum models estimate the *Prof Cur (std)* to be significant and positive.

As for the interpretation of the random effects (see Section 5.3 and Figure 6a), the multiple intercept per earthquake provides an interesting point of discussion. In the Max model built for Coalinga, Izu Oshima, Kumamoto, Loma Prieta and Pisco, the intercepts appear to be non-significant. In these cases, not being significant has a particular meaning because it indicates specific earthquakes for which the model does not strictly require a regression constant. In other words, these five study sites behave in line with the average Max landslide size computed for the whole 25 datasets combined. A similar situation can be seen for the Sum model where four earthquakes (Izu Oshima, Kiholo Bay, Kumamoto and Loma Prieta) have been estimated with a non-significant intercept, indicating their average behavior to be aligned with the whole average summed landslide size across the 25 earthquake cases.

As for the significant cases, a distinction should be made between positive and negative multiple intercepts. A positive regression coefficient implies that for the earthquake under consideration a regression constant should be added to the model to increase the estimated landslide size (whether it is for the Max or Sum models) with respect to the average landslide size for all the 25 cases combined. For the Max model, ten intercepts are significant and positive. By sorting them according to the absolute posterior mean, we can list Guatemala ($|\hat{\beta}| = 1.60$), Denali ($|\hat{\beta}| = 1.36$), Lefkada ($|\hat{\beta}| = 1.09$), Chi-Chi ($|\hat{\beta}| = 0.99$), Iwate Miyagi ($|\hat{\beta}| = 0.87$), Limon ($|\hat{\beta}| = 0.83$), Ludian ($|\hat{\beta}| = 0.80$), Northridge ($|\hat{\beta}| = 0.73$), Wenchuan ($|\hat{\beta}| = 0.73$) and Kiholo Bay ($|\hat{\beta}| = 0.71$).

Similarly, ten more events have been estimated to be significant and negative overall. This is the case for Gorkha ($|\hat{\beta}| = 2.46$), Friuli ($|\hat{\beta}| = 1.98$), Kobe ($|\hat{\beta}| = 1.27$), Yushu ($|\hat{\beta}| = 1.18$), Tohoku ($|\hat{\beta}| = 0.85$), Kashmir ($|\hat{\beta}| = 0.65$), Sierra Cucapah ($|\hat{\beta}| = 0.63$), Minxian ($|\hat{\beta}| = 0.56$), Lushan ($|\hat{\beta}| = 0.18$) and Haiti ($|\hat{\beta}| = 0.12$).

An analogous situation can be found for the Sum model although the events with a significant and positive regression constant are 13 and those that are significant and negative are eight. Sorting for absolute mean regression coefficients, to the positive category belong: Guatemala ($|\hat{\beta}| = 1.55$), Ludian ($|\hat{\beta}| = 1.24$), Iwate Miyagi ($|\hat{\beta}| = 1.22$), Northridge ($|\hat{\beta}| = 1.08$), Limon ($|\hat{\beta}| = 0.87$), Wenchuan ($|\hat{\beta}| = 0.79$), Lefkada ($|\hat{\beta}| = 0.79$), Denali ($|\hat{\beta}| = 0.58$), Coalinga ($|\hat{\beta}| = 0.54$), Chi–Chi ($|\hat{\beta}| = 0.52$), Minxian ($|\hat{\beta}| = 0.42$), Lushan ($|\hat{\beta}| = 0.23$) and Haiti ($|\hat{\beta}| = 0.15$).

As for the negative counterparts the eight cases belong to Gorkha ($|\hat{\beta}| = 2.75$), Friuli ($|\hat{\beta}| = 1.97$), Kashmir ($|\hat{\beta}| = 1.25$), Yushu ($|\hat{\beta}| = 1.11$), Tohoku ($|\hat{\beta}| = 0.94$), Sierra Cucapah ($|\hat{\beta}| = 0.93$), Kobe ($|\hat{\beta}| = 0.85$) and Pisco ($|\hat{\beta}| = 0.48$).

These significant regression coefficients could be associated with both site-specific factors and/or quality of landslide inventories. Hence, they may be sensitive to real landslide size characteristics but also to landslide positional and mapped extent biases (Steger et al., 2016). Denali is one of those cases where the significant and positive intercept is relatively easy to justify. In fact, Jibson et al. (2004) already stated that the 2002 Denali earthquake had significantly lower concentrations of small landslides (rock-falls and rock-slides) compared to an earthquake with comparable or lower magnitude. Their interpretation was mainly due to the ground motion characteristics of the Denali earthquake. Furthermore, they argued that the reason was the deficiency in high-frequencies and high-amplitude accelerations of the seismic shaking. Conversely, a significant regression constant could also be associated with the quality of dataset. For instance, the Limon inventory is another case where we observe a significant and positive regression constant. We recall here that the inventory was mapped by Marc et al. (2016) using 30 m resolution satellite scenes (see Table 1). Notably, mapping landslides using relatively coarse resolution images can induce substantial amalgamation issues in the delineation of large landslides. Therefore, the multiple intercept for Limon could be due to the large size of the landslides, because anything below a 900 m^2 pixel was not even visible during the mapping procedure. Therefore, here we make the point that the quality (Guzzetti et al., 2012) of an inventory could affect the estimates of each regression constant per earthquake. But, this effect can still be traced back and interpreted.

This is not exactly the case for the completeness (Guzzetti et al., 2012) of an EQIL. Tanyaş and Lombardo (2020) proposed a semi-quantitative routine to assess the completeness of the same coseismic landslide inventories used in this work (see Figure 5 in their work). If our model would have strongly suffered from a bias brought by the varying completeness associated with each of the 25 inventories, then one could have expected good inventories to share a common multiple intercept sign and/or amplitude and vice-versa in case of bad inventories. Fortunately, mixed completeness levels are featured in sub-groups of earthquakes associated with positive and negative regression constants. In turn, we can assume that a marked bias towards good or bad inventories should not be assumed for the Max model.

Even for the Sum model, the completeness of each corresponding inventory largely varies between positively and negatively attributed regression constants per earthquake events. This means that a strong influence of the completeness bias should not be present even in our Sum model, although quality-wise the effect can still be present.

This being said, it is inevitable that several sources of bias have made their way into our model, and they will be further discussed in Section 6.3.

Another iid effect in our model corresponds to the Landform classification. We have initially made the expert choice of selecting three properties and use them as random effects whereas all the remaining linear covariates have then been selected on the basis of a variable selection procedure. Therefore, we have kept the Landform classification in the model although, as also visible in Figure 6b, none of the lanform classes play a significant role, nor exhibit a posterior mean coefficient large enough to assume that its inclusion would actually play any role at all in modelling landslide sizes.

Two considerations must be made here. First of all, whether the landforms are featured in the model or not, as they are expressed, the results will essentially stay the same. We have actually re-run a set of tests that confirm this statement (unreported results). However, to avoid re-computing the fits, the 5000 simulations and the Bootstrap step, both for Max and Sum models, we have opted to keep the landforms in. The second consideration consists of assessing why such a covariate, usually quite important in landslide predictive models, has a negligible contribution to the landslide areas. We will start by saying that for consistency reasons we used the same landform classification adopted in Tanyaş et al. (2019a). In this work, the authors used the same SUs partition and co-seismic landslide inventories for building a global susceptibility model. Moreover, they derived only five grouped landform classes. This could have smoothed out the signal of different landform categories to the point where both Max and Sum models may not be able to capture any dependence with respective to the landslide size. Also, a landform classification reflects several aspects of the terrain morphometry, which could have been better explained via numerical covariates such as relief, slope and curvatures, rather than in a categorical form. This being said, we stress that the Max and Sum models are essentially unchanged whether the landforms are featured or not, and yet the overall performance is more than satisfactory. Ultimately, we would like to further comment on the nonlinear effect of the *Slope (avg)*. Figure 6c shows two slightly different patterns for the Max and Sum models. They both appear to play a negligible role in explaining the variability of the landslide sizes up to approximately 30 degrees of SU average steepness. From this threshold onward, the *Slope (avg)* effect becomes slightly positive for the Max model and it becomes positive and much larger for the Sum model. The difference between the two models is subtle but essentially one can see the Sum model to be characterized by larger landslide planimetric areas compared to the Max model. Therefore, a much steeper trend in the regression coefficients of the Sum model can be explained with a greater need of a SU to be steep for it to generate larger mass movements.

6.3 Sources of uncertainty

A large number of uncertainty sources inevitably affect our co-seismic landslide datasets. As briefly mentioned in Section 6.2, the main sources of uncertainty essentially boil down to the quality, completeness and representation of the co-seismic landslide inventories (Guzzetti et al., 2012; Tanyaş et al., 2017). Below, we list potential biases associated with the three concepts mentioned above, and further below we will provide our interpretation of the resulting bias.

- composition of the team mapping the co-seismic landslide inventories.
- the quality of the support data upon which the mapping is undertaken.
  - spatial resolution. Is it fine enough to be able to map?
  - temporal resolution. Is it sufficiently close to the earthquake occurrence or is it far and therefore potentially containing subsequent unrelated landslides?
  - are the satellite scenes covered by clouds?
  - is the extent of the satellite imagery comparable to the extent of the landslide-affected area?
- the technique used for mapping
  - the subjectiveness of the mapping itself in case of manually digitized inventories.
  - the error in the automatic or semi-automatic mapping procedure.
- minimum resolved landslide size.
- the classification (or not) of each landslide according to its types.

The quality of landslide inventories could bring some uncertainties into spatial distribution of co-seismic landslides' size. In this regard, amalgamation of coalescing or adjacent landslides is an issue that typically affects any estimate of landslide sizes, but the level of amalgamation can also vary on the basis of: (i) mapping techniques, (ii) spatial and (iii) temporal resolution of examined scenes (Tanyaş et al., 2019b).

Overall, manual landslide mapping is subjective and the final product varies based on mapping objectives, preferences and/or skill of the interpreter(s) and the time invested in the inventory (Soeters and Van Westen, 1996). Obviously, the database we used in this study includes landslide inventories compiled for different purposes, through various methods and expertise in the 40-year period from 1976 to 2016. With the exception of the Pisco inventory, created via semi-automated mapping routines (Lacroix et al., 2013), all the inventories were mapped manually. Therefore, it is not a homogeneous dataset. Given this limitation, the multiple intercept we included in our models is a way to cope with such uncertainties. For instance, landslides triggered by the Gorkha earthquake were mapped (Roback et al.,

2018) not only to assess the landslide hazard but also to examine mobility of landslides. In turn, Roback et al. (2018) paid an extra attention to amalgamation issues and they even differentiate landslide source and deposit. This could partly explains the significant and negative regression coefficient we calculated for the intercept of the Gorkha case, which is the most striking example among multiple intercepts per earthquake. In fact, Figure 6 reports the largest (in absolute value) posterior mean of the regression coefficient distribution for Gorkha, that the model uses to reduce the estimated landslide size for this particular earthquake. We should also note that this may not be the only interpretation available. The reasons behind it, may also be due to additional seismo-tectonic or ground-motion related factors. And, disentangling the main reason to which extent one cause or the other may be responsible for such a small intercept certainly requires further investigation, even beyond the scope of this work. In either case this particular earthquake was already pointed out to have produced less landslides than the expected number for a comparable magnitude (Kargel et al., 2016; Xu et al., 2016). Moreover, our model adds to this observation, stressing that not only the number of landslides is smaller than other earthquakes, but that this is valid also in terms of planimetric areas.

In addition to mapping techniques, the spatial resolution of the satellite images or orthophotos used to support the mapping itself also effects the level of amalgamation (see the details provided for the Limon case in Section 6.2). Whenever supporting images with high spatial resolution images are used, the ability to characterize small landslides also increases. Therefore, positive or negative regression coefficients associated with each multiple intercept may also be due to this. Haiti is again a good example for a such case. The landslides triggered by the Haiti earthquake were mapped using scenes with a spatial resolution of less than 1 m (see, (Harp et al., 2016) for details and Table 1 for comparison with other inventories). In this regard, we consider the Haiti inventory to be effected by amalgamation to a much lesser extent than most of the other inventories we used.

Moreover, in some cases, if the time gap between pre- and post-seismic images is relatively long, some pre-seismic landslides could be included into the co-seismic landslide inventory by mistake (Tanyaş et al., 2017). This may also lead to map reactivation or expansion or pre-earthquake landslides including the whole landslide scar rather than the newly failed surface. In turn, this may bias the A_L towards much larger estimates than what they should be in reality.

Moreover, the global nature of our dataset incorporates all the above inventory-specific issues. Therefore, biases can arise from their combined co-existence in our Max and Sum models. For instance, inventories containing a much larger landslide population may bias the final predictive model at the expenses of inventories represented by fewer landslides. In this complex system of potential bias interactions, we should also mention that another possible source of bias may exist and it may have directly affected the way we constructed our global dataset. In fact, the Slope Unit partition controlled the landslide area aggregation when we computed the Max and Sum out of the multiple landslides per mapping unit. In this sense, to generate a number of SUs for which a global landslide model can be efficiently built, Tanyaş et al. (2019a) chose a relatively coarse parameterization of *r.slopeunits*—we recall here that the SUs we used are the same as those generated by Tanyas and co-authors. However, a much finer and realistic SU subdivision can still be made, which we expect would substantially improve the Max and Sum models' performance. This being said, we should also report that the selected *r.slopeunits* parameterization has been consistent among different earthquakes. This ensures that whatever bias may exist because of the coarse dimension of the SUs, it would be consistent and relatively constant across our entire global dataset.

Ultimately, it is fair to report that the covariates themselves may bring some degree of uncertainty. In fact, the resolution among covariates substantially changes, starting from a fine representation of terrain properties at 30 m and ending up to the 1 km resolution of the ground motion properties. However, similarly to the Slope Unit dimension case, the difference in resolution among covariates is constant in our global dataset.

6.4 Considerations on modelling landslide areas

Our model has a specific limitation which is worth to be extensively addressed here. We model the planimetric area of landslides on a logarithmic scale. Our model overall performed well in such scale but in order to produce practically interpretable results or maps, we should convert our prediction back into a metric unit. We recall here that as most of the Gaussian models do, we performed much better around the bulk of the landslide area distribution rather than in the tails. Therefore, converting our prediction from the logarithmic to the actual meter scale would exacerbate the difference between (very small and very large) observed and estimated landslide areas.

It is worth noting that this problem exists in most Log-Gaussian models and even in the context of landslide-event magnitude scale. In fact, the same logarithmic representation and associated limitations affect landslide magnitude studies, where frequency-area distributions are modelled in log-scale rather than the metric one (Malamud et al., 2004a).

Another potential difficulty is that the mean of A_L is *not* equal to the exponential of the mean of $\log(A_L)$, which makes the interpretation of results more intricate. However, the logarithm being a monotone increasing function, it respects the transformation of quantiles from one scale to the other (*e.g.*, the median of A_L is equal to the exponential of the median of $\log(A_L)$). Therefore, in two theoretical maps where the landslide size is predicted per SU, the relative classes would be visually maintained in both metric and logarithmic scales.

The landslide area classification we explain in Section 5.5 and show in Figure 8 is meant to limit the issues between the two scales. The overall agreement between observed and predicted landslide classes shows the success of this classification approach (see Figure 22). On average, observed and predicted landslide classes perfectly match for 44% and 46% of examined mapping units for Max and Sum models, respectively (these values correspond to the average height of the green barplots in Figure 22). As for an average percentage of strongly mismatching case, only 7% of predicted landslide sizes is associated with a two-class shift, both for the Max and Sum models (these values correspond to the average height of the red barplots in Figure 22).

6.5 Implications for landslide hazard assessment

The method we propose is the first of its kind. Therefore, the implications it may produce to the landslide hazard concept are still to be investigated. For sure, this globally-applicable model has provided the first predictive maps of the potential landslide area generated in response to an earthquake. This information only answers to one of the three components of the landslide hazard concept, this being how large a landslide-event may be spatially. However, our model, as we defined it, is tightly linked to the ground motion patterns of past earthquakes. Therefore, there is no guarantee that future earthquakes will produce analogous shaking levels and thus, our current landslide size maps are mostly reflecting what happened in the past. We envision two extensions of our model for it to become fully operative. One way is to feature a probabilistic term for the seismic hazard. For instance, once our model has been built and the regression coefficient for the Macroseismic Intensity is available, then any other Macroseismic Intensity (*e.g.*, exceedance in 10 or 50 years return time, Giardini et al., 1999; Jordan et al., 2014) map can be plugged in to produce scenario-based outputs. These scenario-based maps could then be integrated in the decision-making procedure for medium to long term territorial planning.

Conversely, another possible alternative is to use our model in near real–time. As before, the regression coefficients of all covariates, including the Macroseismic Intensity can be kept fixed and right after a future earthquake, the associated Macroseismic Intensity can be plugged in to provide quick post-disaster information on landslide sizes. Nowadays, the United States Geological Survey is able to provide reliable shaking level maps within hours after a major earthquake (Allstadt et al., 2018) and therefore our model could rapidly provide estimates of how large the resulting landslides might be, and how they might be distributed over space.

It is also important to stress that our model is currently valid purely for earthquake-induced landslides. However, we limited our scope to this specific class of trigger because of the global availability of the data. An analogous model could be replicated for rainfall-induced landslides and also for a mixture of both trigger types. Nevertheless, a proportionally large global inventory should be made for the precipitation case.

As mentioned above, to date, no statistically-based spatially-explicit model was able to predict landslide planimetric areas, or their aggregation in a given mapping unit. Therefore, there is no landslide hazard guideline where the use of the model we propose is clearly defined. And yet, in landslide hazard assessment, the frequency-area distribution (Malamud et al., 2004a) derived for a landslide event of a given magnitude is measured as a function of the overall number of landslides and their associated planimetric areas, produced by a given trigger.

Our model can offer additional information to two key tools in landslide hazard assessment. In addition to the prediction of landslide occurrence locations (susceptibility, Reichenbach et al., 2018), and to the estimation of how many landslides may trigger per mapping unit (intensity, Lombardo et al., 2018a), our model can inform decision makers on the extent of the failed surface per slope unit.

Furthermore, in the traditional literature of landslide predictive models, the most common mapping units are grid cells and slope units. However, the model we propose is not suitable for a grid cell spatial partition. In fact, we need to express the landslide size at a scale comparable or larger to the actual landslides. Therefore, grid cells, which are typically much smaller than a landslide, cannot be used. Moreover, in case one would like to generate a squared lattice with a size larger than a landslide, then we stress here that the geomorphological significance will be mostly lost. This is also true for susceptibility studies because a single pixel does not represent the geomorphological process behind a landslide. However, it is even more true and strict when modelling landslide planimetric areas. This is not the case for SUs. Geomorphologically, a slope unit is a medium scale representation of the landscape, positioned in between the fine grid cells—often criticized for the same reason mentioned above, *e.g.*, Reichenbach et al. (2018)—and the catchments—undoubtedly too coarse to be effective for slope stabilization practices. Therefore, at least theoretically a SU partition offers an operational spatial scale upon which the method we propose can be repeated for any other area and/or landslide type. Therefore an additional map predicting SU-based landslide Max or Sum scenarios could become a new tool in landslide hazard mapping. As for a catchment partition, this could still be theoretically doable but the representation of the covariates at such scale may lose connection or correlation with respect to the A_L. For instance, the average slope steepness in a given catchment may be totally unrelated to the landslide planimetric area at a single slope.

6.6 Considerations on the use of earthquake-specific intercepts

In scientific research and experiments, an important requirement of any new concept or model is for it to be repeatable and reproducible. Our model satisfies the repeatability requirement for it is certainly possible to re-run the same analyses following the model description explained in Section 4.3. Moreover, our modeling framework is generic enough that it also satisfies the reproducibility requirement, since the same model structure and estimation method could easily be used with a different earthquake-induced landslide dataset from other study areas. However, a limitation of our approach is that our fitted model, applied to our particular dataset, is not "transferable", in the sense that it cannot be directly applied to other areas without first fitting the model again to relevant data. Transferability assumes that a given model or analytical protocol can be taken outside the specific context in which it was presented and tested elsewhere, by other scientists or engineers. The key reason for the lack of transferability in our case, is that we decided to include earthquake-specific intercept parameters, whose estimated values cannot be extrapolated to other areas. Hence, while the inclusion of a multiple intercept was here necessary to get a good overall fit, it also hinders the use of our model in other geographic areas.

Two solutions are possible to make our model transferable. The first solution involves continuous updates. This means that whenever an earthquake occurs and induces landslides, if the study area is not part of the 25 earthquakes we modelled here, then our model can simply be re-run including the new co-seismic inventory. As the model is updated, we can obtain the regression constant for the new event and extend the geographic validity of our model. This procedure comes at a relevant cost. It implies that we need to wait for an inventory to be compiled before being able to use it for a specific area. In other words, we cannot use it preemptively but rather we have to wait for co-seismic landslides to cause damage before being able to extend our model via a new spatial dataset. Therefore, if this is the case, our model may be of limited practical use.

An alternative does exist even if it comes with some inherited limitations. A regression constant estimated per specific study area essentially applies a constant shift to the $\log(A_L)$ estimates. This shift summarizes site-specific characteristics with respect to the global dataset we used. Therefore, for areas that are not included among the 25 we examined here, one should find a trade off between the optimal $\log(A_L)$ prediction and the need for such estimates despite some bias they may contain. In other words, we could choose to take a leap of faith. We could assume that the new area upon which we need to transfer our Max and/or Sum models behaves similarly to the average landslide size in our global dataset (in which case we can fix the intercept value to be zero, like for Haiti or Kumamoto, see Figure 6a), or to a specific EQIL from our dataset because of analogous tectonic regimes (in which case we can fix the intercept to the value estimated for this particular EQIL). If such a procedure is acceptable, our model then becomes transferable. Surely this procedure might under-/over- estimate the $\log(A_L)$ distribution to some extent. However, the resulting predictive maps will still provide useful information for master planners. In fact, a regression constant added to each SU in a given area does not change the relative spatial predictive pattern. In other words, SUs that are shown to potentially release a larger landslide planimetric area, will still be represented as the most hazardous, even without the site-specific regression constant. Surely, the $\log(A_L)$ estimation per SU will loose accuracy and therefore should not be used to make precise numerical decisions. However, any master planner could still recognize hazardous SUs in a relative sense. This is not trivial information. Knowing which SUs may release a larger landslide area and therefore volume, is extremely important even if we do not know the exact extent.

6.7 Geomorphological Considerations

The model we present can be of use even beyond the landslide hazard context. Landscape evolutionary models (Hancock et al., 2000; Van De Wiel et al., 2007) predict the change of the earth surface in relatively long time scales, compared to the human life expectancy. They are calibrated on the basis of the volume of material eroded from the slopes and deposited away by natural agents. However, these volumes are often estimates only measured for specific catchments and do not account for the contribution of mass wasting processes.

In the context of our model, the volume estimation of EQILs addresses the fundamental question, whether large earthquakes contribute to lift the earth surface and produce mountainous topographies or whether EQILs reduce the actual topography by removing thick portions of the landscape (Parker et al., 2011). The conversion from landslide area to landslide volume is one of a first steps to tackle with this question because the total amount of landslide deposits needs to be identified to assess the mass balance after an earthquake (Dadson et al., 2004; Malamud et al., 2004a; Hovius et al., 2011; Li et al., 2016; Wang et al., 2015). In this regard, the method we introduced could help not only to predict total landslide planimetric areas associated with an earthquake but also their spatial distribution right after the event. Consequently, this method could lead to better understand the balance between crustal advection and seismically induced mass wasting and finally inform us on potential landscape evolution processes. Therefore, our model could be a valid support, providing information on the expected volumes that may be mobilized due to an earthquake. The landslide area has been demonstrated to be related to the landslide volume via a power law (Larsen et al., 2010). Therefore, by transforming the output of the predicted landslide areas into volumes, one could better parametrize landscape evolutionary models with further information that is not usually accounted for. Notably, our model is expressed in $\log(A_L)$, thus an initial transformation in metric scale and then a power law conversion could heavily bias the predicted volume estimates. However, we stress here that the performance we obtained originate from a global dataset, hence, we can only assume it to improve for finer studies, as the data quality increases.

Also, the model we present is based on landslide inventories associated with a single triggering event. Therefore, our model is purely spatial (further details on this definition will be provided in Section 6.8) and does not features the temporal dimension. However, our model could be used also in case of multi-temporal landslide inventories. In such cases, we could model the spatio-temporal evolution of landslide sizes. This could open up interesting geomorphological interpretation of mass wasting processes and their influence on landscape evolution and more details are provided in Section 6.8.

6.8 Statistical Considerations

Although our modelling approach represents an important contribution landslide hazard modelling, many improvements can already be envisioned from a statistical perspective.

First, our focus here is to model and predict the size of landslides only, but a joint modelling approach could have been considered to simultaneously model both the landslide susceptibility (Reichenbach et al., 2018) and sizes, or landslide intensity (Lombardo et al., 2020a) and size. In particular, the INLA approach offers a suitable statistical framework where different likelihoods can be assumed for different responses sharing common features (see, *e.g.*, Krainski et al. 2018, Chapter 3).

Second, our modelling approach is not "strictly spatial" in the sense that—for fixed covariate values—it does not define a correlation or covariance structure between observations in neighboring SUs. In other words, our Max and Sum models treat close-by and far away SUs equally. While such an assumption is reasonable from a computational perspective, it also means that we are unable to capture spatially structured effects that are not already captured by the available covariates. If such unobserved spatial effects are strong and not accounted for in the model, this might bias the estimated covariate effects and might even in some cases affect their geomorphological interpretation. Fortunately for us, as shown by Lombardo et al. (2019a), the *Macroseimic Intensity (MI)* covariate is a good proxy for the trigger and usually provides similar information as a model for EQILs that would include a latent spatially-correlated effect (Lombardo et al., 2018a). Therefore, we can here reasonably assume, and be confident that by including the *MI* and related covariate information in our model, the residual spatial correlation is quite weak overall, though this would need to be checked more systematically and thoroughly. For rainfall-induced landslides, however, it is usually much more difficult to obtain relevant covariates representing the trigger at high resolution, and for such data, additional latent spatial effects (specific to each event) would seem necessary. Such a spatial model defined at the latent level can be constructed using the stochastic partial differential equation (SPDE) approach that provides accurate Markovian representations of the flexible Matérn covariance (see, Schabenberger and Gotway 2017, Chapter 4 for an introduction on covariance functions and Castro-Camilo et al. 2020 for the use of the SPDE approach in a prediction framework). For the dataset used here, a sensible approach is to assume different SPDE models for each earthquake inventory, which helps us reduce the computation burden. However, even doing so, this modelling approach carries significant computational challenges (Castro-Camilo et al., 2020), and simpler spatial structures could be envisioned, *e.g.*, using the Besag model for areal units as in Lombardo et al. (2018a).

Third, although the inventories used in our work correspond to spatially replicated events around the world, we could focus on a single area instead, where multitemporal inventories are available. Under such a setting, spatio-temporal models based on a Log-Gaussian likelihood can help us describe the spatial extent of landslides and their evolution in time. Space-time landslide intensity models were fitted by Lombardo et al. (2020a) and it would be interesting to generalize their approach to model the spatio-temporal evolution of landslide sizes, potentially jointly with their occurrence locations. Moreover, the SPDE approach mentioned earlier can also be extended to describe processes evolving in space and time using separable covariance structures (Gneiting et al., 2006). It is important to notice, however, that the computational gains obtained through the reduction in spatial coverage are counterbalanced by the complexity associated with spatio-temporal models; therefore, it is difficult to assess the computational requirements in advance.

As mentioned above, our model is not spatial in the sense that it does not account for the spatial relationship between slope units. Ignoring spatial correlation would make estimates' posterior standard deviations too small. A spatial model would reduce the effective sample size since realisations that are spatially correlated reduce their contribution as they provide similar information. Nonetheless, such spatial analysis will have little effect on the estimates (Hodges, 2013, Chapter 9). Therefore, the main difference between a model such as ours and a model that includes spatial interactions lies in the uncertainty quantification of the estimates. The parametric Bootstrap methodology that we described in Section 4.2 is one way to compensate for this and to quantify the potential uncertainty underestimation. Indeed, it can be perceived as a post-processing step of the fits, where resampling techniques are used in order to construct many new data samples that, in turn, can be used to refit several models. The estimates extracted from each new fit are then used to compute sample standard deviations for the original estimates. Although this process is more computationally demanding, it guarantees a more realistic uncertainty quantification. This means that Bootstrap-based standard deviations can in some cases be fairly large compared to their INLA counterpart, as can be observed in Figures 9 to 20.

6.9 Computational Requirements

The models used here for $A_{L_{max}}$ and $A_{L_{sum}}$ can be fitted using cutting-edge computers running any of the standard operating systems currently available. RAM requirements are usually linear in the number of INLA threads, which is a parameter that can be specified with the main INLA function. In our case, the models were fitted using a CentOS 7 Linux computer with two threads. RAM usage was less than 1 Gb for INLA alone, which means that additional RAM should be considered to, *e.g.*, run the R software. Model fitting and prediction took approximately 10 minutes for both models.

The Bootstrap procedure consisted mainly of two stages. The first one (creating the Bootstrap samples) took approximately 3.2 hours, while the second one (fitting models using Bootstrap samples) took roughly the same time as for the original fits, for each model and each of the 300 Bootstrap samples. The first stage can be fitted using a state-of-the-art laptop or desktop computer, but the second stage requires additional computational power and can easily exploit parallel computing. We used resources for distributed computers to speed up the Bootstrap samples fits, using CentOS 7 Linux workstations. Again, for every single fit, less than 1 Gb was required for INLA alone.

A key element at the core of the INLA algorithm is numerical linear algebra for large sparse matrices, which take most of the total runtime. For a spatial model with $|\mathcal{S}| \sim 10^5$ or less data points, these operations can be handle by INLA thanks to an internal parallelisation using OpenMP (Van Niekerk et al., 2019). For greater $|\mathcal{S}|$, additional parallel numerical methods for large sparse matrices are needed. The current R-INLA implementation allows the use of the PARDISO library, which is a powerful memory-efficient software for solving large sparse linear systems of equations. Its integration with INLA further increases INLA capability to solve very high-dimensional problems (Van Niekerk et al., 2019), such as the one we will face using landslide inventories with a more refined SU partition. Further runtime reductions can be achieve using any of the less accurate approximations methods provided in the R-INLA library (Rue et al., 2017).

6.10 Additional Information

We remind here the reader that our Gaussian model estimates the mean of the target variable conditional to a set of covariates. This implies that our Max model estimates the conditional mean of the maximum log-landslide size per SU. Similarly, our Sum model estimates the conditional mean of the logarithmic cumulative landslide size per SU. If we had used the average of all the landslide planimetric areas per SU, we would have therefore modelled the conditional mean of the logarithmic average landslide size per SU. For landslide hazard assessment, where the common assumption is to generally consider or prioritize the worst case scenarios, modelling the mean of the average landslide size might not add information of particular relevance. In fact, on a slope where multiple landslides occur, a model able to predict the average landslide size will inevitably underestimate the combined effect of several, potentially interacting, moving masses. Conversely, the Max and Sum models should be much closer to the actual physical manifestation of multiple interacting landslides.

Nevertheless, we envisioned that modelling the actual landslide size of single landslides per SU could have enabled interesting geomorphological considerations. Modelling the size of single landslides would imply looking for the "true mean" of the landslide size distribution. This could be achieved by modelling all the possible landslides per SU simultaneously rather than feeding to our model a single aggregated measure. We initially attempted to model the "true mean" of the landslide size by implementing a similar log-Gaussian model. In this case, the dataset contained repeated covariate values for landslides occurring in the same SU, giving rise to a data frame with approximately 450,000 observations. This model did not provide satisfactory results, having tested multiple parameterisations and combinations of covariates. This might be due to the large increase in the number of observations, while keeping the number of covariates and the model structure fixed (which might imply a reasonable fit for some data points, but poor fit for a larger proportion of the data), or it might be due to correlations between landslide sizes within the same SUs that we neglected, or finally it could also be due to numerical instabilities owing to the larger sample size.

In a second attempt, we tried to reach to the same outcome via a slightly different model. As per Equation (1), every slope unit $\mathbf{s}$ is assigned with a precision parameter, $\tau(\mathbf{s})$, which we assumed to be random but the same for all SUs. To model the "true mean" landslide size, we computed the average and standard deviation of the landslides' planimetric areas per SU. As a result, our log-Gaussian model had as target variable the average of all landslides per SU, and the precision parameter was set to be a function of the standard deviation of all landslides falling in a SU. The above means that the standard deviation is assumed to be the same within each SU, but possibly different among different SUs. In this way, we avoided the repetition of covariates in case of multiple landslides per SU, which we believed to be the reason for the previous failure. However, even in this case, our log-Gaussian model did not converge to a satisfactory solution.

Another potential reason for this might be amalgamation issues in the landslide mapping procedure. In fact, by using a single summary statistic, the Max or the Sum, we reduce the large variability in the landslide size distribution. Therefore, in some way, we are smoothing the extremely varied and detailed information brought by each landslide in a SU. However, we believe this to be a topic of particular relevance for the geomorphological community. Therefore, in our future research, we plan to model the "true mean" landslide size per SU with a much more precise landslide inventory and much more refined SU partition. More details on possible future extensions of our model are presented in the next section.

6.11 Future extensions

The model we present has been built on the basis of global EQILs but it is not bound to the global nor to the co-seismic context. Its structure is applicable to any landslide hazard and for this reason, we envision to extend the very same model in few but precise directions:

- Application to specific landslide types.
- Application to any scale, from the catchment to the global levels.
- Application to rainfall-induced landslides.
- Application to snow-melt-induced landslides.
- Application to co-seimic, rainfall-induced and snow-melt-induced landslides altogether.

The current dataset could not discriminate between landslide types. Therefore, the uncertainty due to the difference in failure mechanisms among landslides has inevitably propagated into our result. However, we expect that a much more precise outcome could be achieved by modelling the planimetric area of landslides that share a common physical behavior. In turn, this will also enable landslide-class-specific interpretations and considerations that could better inform decision makers. For instance, one could estimate the potential landslide planimetric area to be triggered per SU in a specific site, and examine the expected $\log(A_L)$ for rockfalls and debris-flows separately.

Also, one of the problems in this work is the global nature of the dataset we used. However, one could opt to model the $\log(A_L)$ at any other scale, from the fine catchment level, to the coarser regional or national scale. This would likely get rid of the necessity for a multiple intercept, making future models potentially more spatially or temporally transferable.

The present model can be applied to rainfall-triggered landslides. The structure could be left unchanged whereas the covariate selection could certainly vary by removing the ground motion, both *MI (avg)* and *MI (std)*, and/or adding the spatial signal of the rainfall discharge, if available. The same is valid for snow-melt landslide inventories.

Ultimately, we also envision a possible application of statistical models that can contextually distinguish the landslide size to the class of the landslide itself. Such models will represent an extension to the present case where a single likelihood for the $\log(A_L)$ is taken into consideration. Such extension would require statistical models that can take on multiple likelihoods also referred to as joint-probability models.

7 Conclusions

Fulfilling the standard definition of landslide hazard requires the expectation or prediction of where, when or how frequently a population of landslides may occur, as well as how large the landslide population may be. The way that the geomorphological community—at least the part of the community working on statistically-based hazard models—has interpreted the term "how large" for decades, is to estimate the event landslide magnitude, an index of how many and how large the total number of landslides may be. As a result, by providing a single number to represent the landslide-event-magnitude, the community has disregarded the geographic characteristic of the landslide size information. In other words, maps capable of statistically estimating the expected extent of a failing slope are not available at present. Our work, fills this gap and it is aimed to provide an additional tool both for academic researchers as well as the public. The current way governmental agencies manage the territory for landslide risk prevention is to use susceptibility maps, which convey the information about where landslides are expected to trigger. Therefore, our Max and Sum models could be considered a complementary resource to improve operational decisions in territorial management protocols. By additionally considering the expected extent of a failing slope, together with the probability of a given slope to fail in the first place, much better decisions could be made to ensure the safety of human infrastructure and lives. We stress here that we consider the SU spatial partition to be the most suitable for our model to be performed. If for susceptibility models the community is still debating whether a fine grid cell or a SU can provide useful information, we believe that a fine grid cell partition will not capture the Max and Sum landslide size characteristics. Furthermore, we think that a coarse pixel partition upon which to compute the Max and Sum landslide area would neglect the geomorphological and intrinsically non-regular nature of the landslide process. Conversely, a SU-based approach both provides a suitable terrain partition upon which one can compute the two landslide area parameters and a geomorphologically-sound subdivision of the landscape.

References

Adams, P. W. and Sidle, R. C. (1987) Soil conditions in three recent landslides in southeast Alaska. Forest Ecology and Management **18**(2), 93–102.

Allstadt, K. E., Jibson, R. W., Thompson, E. M., Massey, C. I., Wald, D. J., Godt, J. W. and

Rengers, F. K. (2018) Improving Near-Real-Time Coseismic Landslide Models: Lessons Learned from the 2016 Kaikōura, New Zealand, EarthquakeImproving Near-Real-Time Coseismic Landslide Models. Bulletin of the Seismological Society of America **108**(3B), 1649–1664.

Alvioli, M., Marchesini, I., Reichenbach, P., Rossi, M., Ardizzone, F., Fiorucci, F. and Guzzetti, F. (2016) Automatic delineation of geomorphological slope units with r.slopeunits v1.0 and their optimization for landslide susceptibility modeling. Geoscientific Model Development **9**(11), 3975–3991.

Amatulli, G., Domisch, S., Tuanmu, M.-N., Parmentier, B., Ranipeta, A., Malczyk, J. and Jetz, W. (2018) A suite of global, cross-scale topographic variables for environmental and biodiversity modeling. Scientific data **5**, 180040.

Ardizzone, F., Cardinali, M., Carrara, A., Guzzetti, F. and Reichenbach, P. (2002) Impact of mapping errors on the reliability of landslide hazard maps. Natural Hazards and Earth System Science, Publications on behalf of the European Geosciences Union **2**, 3–14.

Barlow, J., Barisin, I., Rosser, N., Petley, D., Densmore, A. and Wright, T. (2015) Seismically-induced mass movements and volumetric fluxes resulting from the 2010 Mw= 7.2 earthquake in the Sierra Cucapah, Mexico. Geomorphology **230**, 138–145.

Beven, K. and Kirkby, M. J. (1979) A physically based, variable contributing area model of basin hydrology/Un modèle à base physique de zone d'appel variable de l'hydrologie du bassin versant. Hydrological Sciences Journal **24**(1), 43–69.

Bivand, R. and Piras, G. (2015) Comparing Implementations of Estimation Methods for Spatial Econometrics. Journal of Statistical Software **63**(18), 1–36.

Bourdeau, C., Havenith, H.-B., Fleurisson, J.-A. and Grandjean, G. (2004) Numerical modelling of seismic slope stability. In Engineering Geology for Infrastructure Planning in Europe, pp. 671–684. Springer.

Brabb, E. E. (1991) The world landslide problem. Episodes **14**(1), 52–61.

Brabb, E. E. and Harrod, B. L. (eds) (1989) Landslides: Extent and Economic Significance: Proceedings 28th International Geological Congress Symposium on Landslides. Vermont: Rotterdam and Brookfield. 00000.

Brenning, A. (2005) Spatial prediction models for landslide hazards: review, comparison and evaluation. Natural Hazards and Earth System Science **5**(6), 853–862.

Broeckx, J., Rossi, M., Lijnen, K., Campforts, B., Poesen, J. and Vanmaercke, M. (2019) Landslide mobilization rates: A global analysis and model. Earth-Science Reviews p. 102972.

Brunetti, M., Guzzetti, F. and Rossi, M. (2009a) Probability distributions of landslide volumes. Nonlinear Processes in Geophysics **16**(2), 179–188.

Brunetti, M., Guzzetti, F. and Rossi, M. (2009b) Probability distributions of landslide volumes. Nonlinear Processes in Geophysics **16**(2), 179–188.

Buchanan, T. J. and Somers, W. P. (1976) Discharge measurements at gaging stations. In Techniques for Water Investigations of the United States Geological Survey, number 3 in Applications of Hydraulics. Washington D.C.: United States Government Printing Office, second edition.

Bucknam, R. C., Coe, J. A., Chavarria, M. M., Godt, J. W., Tarr, A. C., Bradley, L.-A., Rafferty, S., Hancock, D., Dart, R. L. and Johnson, M. L. (2001) Landslides Triggered by Hurricane Mitch in Guatemala — Inventory and Discussion. Technical report, U. S. Geological Survey Open-File Report.

Cardinali, M., Ardizzone, F., Galli, M., Guzzetti, F. and Reichenbach, P. (2000) Landslides triggered by rapid snow melting: the December 1996–January 1997 event in Central Italy. In Proceedings 1^st Plinius Conference on Mediterranean Storms, pp. 439–448.

Cardinali, M., Reichenbach, P., Guzzetti, F., Ardizzone, F., Antonini, G., Galli, M., Cacciano, M., Castellani, M. and Salvati, P. (2002) A geomorphological approach to the estimation of landslide hazards and risks in umbria, central italy. Natural Hazards Earth Systems Science .

Carrara, A. (1988) Drainage and divide networks derived from high-fidelity digital terrain models. In Quantitative analysis of mineral and energy resources, pp. 581–597. Springer.

Castro Camilo, D., Lombardo, L., Mai, P., Dou, J. and Huser, R. (2017) Handling high predictor dimensionality in slope-unit-based landslide susceptibility models through LASSO-penalized Generalized Linear Model. Environmental Modelling and Software **97**, 145–156.

Castro-Camilo, D., Mhalla, L. and Opitz, T. (2020) Bayesian space-time gap filling for inference on extreme hot-spots: an application to red sea surface temperatures. Extremes (to appear) .

Catani, F., Tofani, V. and Lagomarsino, D. (2016) Spatial patterns of landslide dimension: a tool for magnitude mapping. Geomorphology **273**, 361–373.

Chen, C.-W., Oguchi, T., Hayakawa, Y. S., Saito, H. and Chen, H. (2017) Relationship between landslide size and rainfall conditions in Taiwan. Landslides **14**(3), 1235–1240.

Cheng, S., Yang, G., Yu, H., Li, J. and Zhang, L. (2012) Impacts of Wenchuan Earthquake-induced landslides on soil physical properties and tree growth. Ecological Indicators **15**(1), 263–270.

Chigira, M. and Yagi, H. (2006) Geological and geomorphological characteristics of landslides triggered by the 2004 mid niigta prefecture earthquake in japan. Engineering Geology **82**(4), 202–221.

Corominas, J. and Mavrouli, J. (2011) Living with landslide risk in europe: Assessment, effects of global change, and risk management strategies. Documento técnico, SafeLand. 7th Framework Programme Cooperation Theme **6**.

Cressie, N. (2015) Statistics for spatial data. John Wiley & Sons.

Cruden, D. and Fell, R. (1997a) Quantitative risk assessment for slopes and landslides-the state of the art. Landslide Risk Assessment pp. 3–12.

Cruden, D. M. (1991) A simple definition of a landslide. Bulletin of the International Association of Engineering Geology **43**(1), 27–29.

Cruden, D. M. and Fell, R. (1997b) Landslide Risk Assessment. First edition, volume 1. CRC Press - Taylor & Francis. ISBN 978-90-5410-914-3.

Cruden, D. M. and Varnes, D. J. (1996) Landslides: investigation and mitigation. Chapter 3–Landslide types and processes. Transportation research board special report (247).

Dadson, S. J., Hovius, N., Chen, H., Dade, W. B., Lin, J.-C., Hsu, M.-L., Lin, C.-W., Horng, M.-J., Chen, T.-C., Milliman, J. et al. (2004) Earthquake-triggered increase in sediment delivery from an active mountain belt. Geology **32**(8), 733–736.

Dai, F. and Lee, C. (2001) Frequency–volume relation and prediction of rainfall-induced landslides. Engineering geology **59**(3-4), 253–266.

Daniell, J. E., Schaefer, A. M. and Wenzel, F. (2017) Losses Associated with Secondary Effects in Earthquakes. Frontiers in built environment **3**, Article: 30.

Dowling, C. A. and Santi, P. M. (2014) Debris flows and their toll on human life: a global analysis of debris–flow fatalities from 1950 to 2011. Natural hazards **71**(1), 203–227.

Dussauge, C., Grasso, J.-R. and Helmstetter, A. (2003) Statistical analysis of rockfall volume distributions: Implications for rockfall dynamics. Journal of Geophysical Research: Solid Earth **108**(B6).

Fan, X., Scaringi, G., Korup, O., West, A. J., van Westen, C. J., Tanyas, H., Hovius, N., Hales, T. C., Jibson, R. W., Allstadt, K. E. et al. (2019) Earthquake-Induced Chains of Geologic Hazards: Patterns, Mechanisms, and Impacts. Reviews of Geophysics .

Farr, T. G., Rosen, P. A., Caro, E., Crippen, R., Duren, R., Hensley, S., Kobrick, M., Paller, M., Rodriguez, E., Roth, L. et al. (2007) The Shuttle Radar Topography Mission. Reviews of geophysics **45**(2).

Fell, R. (1994) Landslide risk assessment and acceptable risk. Canadian Geotechnical Journal **31**(2), 262–272.

Fell, R., Corominas, J., Bonnard, C., Cascini, L., Leroi, E., Savage, W. Z. et al. (2008) Guidelines for landslide susceptibility, hazard and risk zoning for land-use planning. Engineering Geology **102**(3-4), 99–111.

Fell, R. and Harford, D. (1997) Landslide risk management. In Landslide Risk Assessment, eds D. M. Cruden and R. Fell, pp. 51–109. Balkema, rotterdam edition.

Frattini, P., Crosta, G. and Carrara, A. (2010) Techniques for evaluating the performance of landslide susceptibility models. Engineering Geology **111**(1), 62–72.

Frattini, P. and Crosta, G. B. (2013) The role of material properties and landscape morphology on landslide size distributions. Earth and Planetary Science Letters **361**, 310–319.

Fuchs, S., Heiss, K. and Hübl, J. (2007) Towards an empirical vulnerability function for use in debris flow risk assessment. Natural Hazards and Earth System Sciences **7**, 495–506.

Galli, M. and Guzzetti, F. (2007) Landslide vulnerability criteria: A case study from umbria, central italy. Environmental Management **40**(4), 649–665. 00089.

Gelman, A., Carlin, J. B., Stern, H. S., Dunson, D. B., Vehtari, A. and Rubin, D. B. (2013) Bayesian data analysis. CRC press.

Giardini, D., Grünthal, G., Shedlock, K. M. and Zhang, P. (1999) The GSHAP global seismic hazard map. Annals of Geophysics **42**(6).

Glade, T., Anderson, M. and Crozier, M. J. (eds) (2005) Landslide Hazard and Risk. Volume 1. Chichester, West Sussex, England ; Hoboken, NJ: J. Wiley. ISBN 978-0-471-48663-3.

Gneiting, T., Balabdaoui, F. and Raftery, A. E. (2007) Probabilistic forecasts, calibration and sharpness. Journal of the Royal Statistical Society: Series B (Statistical Methodology) **69**(2), 243–268.

Gneiting, T., Genton, M. G. and Guttorp, P. (2006) Geostatistical space-time models, stationarity, separability, and full symmetry. Monographs On Statistics and Applied Probability **107**, 151.

Gorum, T., Korup, O., van Westen, C. J., van der Meijde, M., Xu, C. and van der Meer, F. D. (2014) Why so few? Landslides triggered by the 2002 Denali earthquake, Alaska. Quaternary Science Reviews **95**, 80–94.

Govi, M. (1977) Photo-interpretation and mapping of the landslides triggered by the Friuli earthquake (1976). Bulletin of the International Association of Engineering Geology-Bulletin de l'Association Internationale de Géologie de l'Ingénieur **15**(1), 67–72.

Grabs, T., Seibert, J., Bishop, K. and Laudon, H. (2009) Modeling spatial patterns of saturated areas: A comparison of the topographic wetness index and a dynamic distributed model. Journal of Hydrology **373**(1-2), 15–23.

GRASS Development Team (2017) Geographic Resources Analysis Support System (GRASS) Software. Open Source Geospatial Foundation.

Gutenberg, B. and Richter, C. F. (1936) Magnitude and energy of earthquakes. Science **83**(2147), 183–185.

Guthrie, R. and Evans, S. (2004) Magnitude and frequency of landslides triggered by a storm event, loughborough inlet, british columbia .

Guzzetti, F. (2000) Landslide fatalities and the evaluation of landslide risk in Italy. Engineering Geology **58**(2), 89–107. 00381.

Guzzetti, F. (2005) Landslide hazard and risk assessment (Ph.D. Thesis). Mathematisch-Naturwissenschaftlichen Fakultät der Rheinischen Friedrich-Wilhelms-Universität, University of Bonn, Bonn, Germany pp. 33–65.

Guzzetti, F., Ardizzone, F., Cardinali, M., Rossi, M. and Valigi, D. (2009) Landslide volumes and landslide mobilization rates in Umbria, central Italy. Earth and Planetary Science Letters **279**(3-4), 222–229.

Guzzetti, F., Cardinali, M., Reichenbach, P. and Carrara, A. (2000) Comparing landslide maps: A case study in the upper tiber river basin, central italy. Environmental Management **25**(3), 247–263. 00000.

Guzzetti, F., Carrara, A., Cardinali, M. and Reichenbach, P. (1999) Landslide hazard evaluation: A review of current techniques and their application in a multi-scale study, central italy. Geomorphology **31**(1), 181–216.

Guzzetti, F., Galli, M., Reichenbach, P., Ardizzone, F. and Cardinali, M. (2006) Landslide hazard assessment in the Collazzone area, Umbria, Central Italy. Natural Hazards and Earth System Sciences **6**(1), 115–131.

Guzzetti, F., Malamud, B. D., Turcotte, D. L. and Reichenbach, P. (2002) Power-law correlations of landslide areas in central Italy. Earth and Planetary Science Letters **195**(3-4), 169–183.

Guzzetti, F., Mondini, A. C., Cardinali, M., Fiorucci, F., Santangelo, M. and Chang, K.-T. (2012) Landslide inventory maps: New tools for an old problem. Earth-Science Reviews **112**(1-2), 42–66.

Guzzetti, F., Reichenbach, P., Cardinali, M., Ardizzone, F. and Galli, M. (2003) The impact of landslides in the Umbria region, central Italy. Natural Hazards and Earth System Sciences **3**, 469–486.

Guzzetti, F., Reichenbach, P., Cardinali, M., Galli, M. and Ardizzone, F. (2005a) Probabilistic landslide hazard assessment at the basin scale. Geomorphology **72**(1-4), 272–299.

Guzzetti, F., Stark, C. P. and Salvati, P. (2005b) Evaluation of flood and landslide risk to the population of Italy. Environmental Management **36**(1), 15–36.

Hancock, G., Evans, K., Willgoose, G., Moliere, D., Saynor, M. and Loch, R. (2000) Medium-term erosion simulation of an abandoned mine site using the SIBERIA landscape evolution model. Soil Research **38**(2), 249–264.

Hansen, A. (1984) Landslide hazard analysis. Slope instability. Wiley, New York pp. 523–602.

Harp, E. L., Hartzell, S. H., Jibson, R. W., Ramirez-Guzman, L. and Schmitt, R. G. (2014) Relation of Landslides Triggered by the Kiholo Bay Earthquake to Modeled Ground MotionRelation of Landslides Triggered by the Kiholo Bay Earthquake to Modeled Ground Motion. Bulletin of the Seismological Society of America **104**(5), 2529–2540.

Harp, E. L. and Jibson, R. W. (1995) Inventory of landslides triggered by the 1994 northridge, california earthquake.

Harp, E. L. and Jibson, R. W. (1996) Landslides triggered by the 1994 Northridge, California earthquake. Seismological Society of America Bulletin **86**, S319–S332. 00000.

Harp, E. L., Jibson, R. W. and Schmitt, R. G. (2016) Map of landslides triggered by the January 12, 2010, Haiti earthquake. US Geological Survey Scientific Investigations Map **3353**, 15.

Harp, E. L. and Keefer, D. (1990) Landslides triggered by the earthquake. In The Coalinga, California, Earthquake of May 2, 1983, Rymer MJ, Ellsworth WL (eds). Technical report, Vol. 1487, US Geological Survey Professional Paper; 335347.

Harp, E. L., Wilson, R. C. and Wieczorek, G. F. (1981) Landslides from the February 4, 1976, Guatemala earthquake. Technical report, US Government Printing Office Washington, DC.

Heerdegen, R. G. and Beran, M. A. (1982) Quantifying source areas through land surface curvature and shape. Journal of Hydrology **57**(3-4), 359–373.

Hengl, T., de Jesus, J. M., Heuvelink, G. B., Gonzalez, M. R., Kilibarda, M., Blagotić, A., Shangguan, W., Wright, M. N., Geng, X., Bauer-Marschallinger, B. et al. (2017) SoilGrids250m: Global gridded soil information based on machine learning. PLoS one **12**(2), e0169748.

Hengl, T., Kempen, B., Heuvelink, G. and Malone, B. (2019) Package 'gsif' .

Hodges, J. S. (2013) Richly parameterized linear models: additive, time series, and spatial models using random effects. CRC Press.

Hovius, N., Meunier, P., Lin, C.-W., Chen, H., Chen, Y.-G., Dadson, S., Horng, M.-J. and Lines, M. (2011) Prolonged seismically induced erosion and the mass balance of a large earthquake. Earth and Planetary Science Letters **304**(3-4), 347–355.

Hovius, N., Stark, C. P. and Allen, P. A. (1997) Sediment flux from a mountain belt derived by landslide mapping. Geology **25**(3), 231–234.

Hrafnkelsson, B., Siegert, S., Huser, R., Bakka, H. and Jóhannesson, A. (2020) Max-and-Smooth: a two-step approach for approximate Bayesian inference in latent Gaussian models. Bayesian Analysis To appear.

Hungr, O. (1997a) Some methods of landslide hazard intensity mapping. In Landslide Risk Assessment, eds D. M. Cruden and R. Fell, volume 1, pp. 215–226. Rotterdam: Balkema Publisher.

Hungr, O. (1997b) Some methods of landslide hazard intensity mapping. In Landslide risk assessment, pp. 215–226. Routledge.

Hungr, O., Leroueil, S. and Picarelli, L. (2014) The Varnes classification of landslide types, an update. Landslides **11**(2), 167–194.

Jacobs, L., Dewitte, O., Poesen, J., Maes, J., Mertens, K., Sekajugo, J. and Kervyn, M. (2017) Landslide characteristics and spatial distribution in the Rwenzori Mountains, Uganda. Journal of African Earth Sciences **134**, 917–930.

Jasiewicz, J. and Stepinski, T. F. (2013) Geomorphons—a pattern recognition approach to classification and mapping of landforms. Geomorphology **182**, 147–156.

Jeandet, L., Steer, P., Lague, D. and Davy, P. (2019) Coulomb mechanics and relief constraints explain landslide size distribution. Geophysical Research Letters **46**(8), 4258–4266.

Jibson, R. W., Harp, E. L., Schulz, W. and Keefer, D. K. (2004) Landslides triggered by the 2002 Denali Fault, Alaska, earthquake and the inferred nature of the strong shaking. Earthquake Spectra **20**(3), 669–691.

Jibson, R. W., R. Grant, A. R., Witter, R. C., Allstadt, K. E., Thompson, E. M. and Bender, A. M. (2020) Ground Failure from the Anchorage, Alaska, Earthquake of 30 November 2018. Seismological Research Letters **91**(1), 19–32.

Jibson, R. W. and Tanyaş, H. (2020) The influence of frequency and duration of seismic ground motion on the size of triggered landslidesA regional view. Engineering Geology p. 105671.

Jóhannesson, A., Hrafnkelsson, B., Huser, R., Bakka, H. and Siegert, S. (2020) Approximate Bayesian inference for spatio-temporal flood frequency analysis. Submitted, arXiv preprint:1907.04763.

Jordan, T., Marzocchi, W., Michael, A. and Gerstenberger, M. (2014) Operational earthquake forecasting can enhance earthquake preparedness.

Kargel, J. S., Leonard, G. J., Shugar, D. H., Haritashya, U. K., Bevington, A., Fielding, E., Fujita, K., Geertsema, M., Miles, E., Steiner, J. et al. (2016) Geomorphic and geologic controls of geohazards induced by Nepal's 2015 Gorkha earthquake. Science **351**(6269), aac8353.

Keefer, D. K. (1984) Landslides caused by earthquakes. Geological Society of America Bulletin **95**(4), 406–421.

Keefer, D. K. (2000) Statistical analysis of an earthquake-induced landslide distribution—the 1989 Loma Prieta, California event. Engineering Geology **58**(3-4), 231–249.

Keefer, D. K. (2002) Investigating Landslides Caused by Earthquakes: A Historical Review. Surveys in Geophysics **23**, 473–510.

Keefer, D. K. (2013) Landslides Generated by Earthquakes: Immediate and Long-Term Effects. In Treatise on Geomorphology, eds J. F. Shroder Jr and L. A. Owen, pp. 250–266. San Diego: Elsevier Ltd.

Keefer, D. K. and Manson, M. W. (1998) Regional distribution and characteristics of landslides generated by the earthquake, in d. k. keefer (ed.), the loma prieta, california, earthquakes of october 17, 1989-landslides (pp. 7–32).u.s. geological survey professional paper(1551-c) .

Kennedy, I., Petley, D., Williams, R. and Murray, V. (2015) A systematic review of the health impacts of mass earth movements (landslides). PLoS Currents **7**(DISASTERS).

Khaldoun, A., Moller, P., Fall, A., Wegdam, G., De Leeuw, B., Méheust, Y., Fossum, J. O. and Bonn, D. (2009) Quick clay and landslides of clayey soils. Physical review letters **103**(18), 188301.

Khazai, B. and Sitar, N. (2004) Evaluation of factors controlling earthquake-induced landslides caused by chi-chi earthquake and comparison with the northridge and loma prieta events. Engineering geology **71**(1-2), 79–95.

Kirschbaum, D. B., Adler, R., Hong, Y., Hill, S. and Lerner-Lam, A. (2010) A global landslide catalog for hazard applications: method, results, and limitations. Natural Hazards **52**(3), 561–575.

Kockelman, W. J. (1986) Some techniques for reducing landslide hazards. Bulletin of the Association of Engineering Geologists **23**(1), 29–52.

Korup, O., Görüm, T. and Hayakawa, Y. (2012) Without power? Landslide inventories in the face of climate change. Earth Surface Processes and Landforms **37**(1), 92–99.

Korup, O., Gorum, T. and Hayakawa, Y. S. (2011) Without power? Landslide Inventories in the Face of Climate Change. Earth Surface Processes and Landforms pp. n/a–n/a.

Krainski, E. T., Gómez-Rubio, V., Bakka, H., Lenzi, A., Castro-Camilo, D., Simpson, D., Lindgren, F. and Rue, H. (2018) Advanced spatial modeling with stochastic partial differential equations using R and INLA. Chapman and Hall/CRC.

Kramer, S. L. (1996) Geotechnical earthquake engineering. Prentice Hall, Upper Saddle River, N.J. .

Kritikos, T., Robinson, T. R. and Davies, T. R. (2015) Regional coseismic landslide hazard assessment without historical landslide inventories: A new approach. Journal of Geophysical Research: Earth Surface **120**(4), 711–729.

Ksu, K. J. (1975) Catastrophic debris stream (Sturzstorm) generated by rockfalls. Geological Society of America Bulletin **86**, 129–140.

Lacroix, P., Zavala, B., Berthier, E. and Audin, L. (2013) Supervised method of landslide inventory using panchromatic SPOT5 images and application to the earthquake-triggered landslides of Pisco (Peru, 2007, Mw8. 0). Remote Sensing **5**(6), 2590–2616.

Lagomarsino, D., Tofani, V., Segoni, S., Catani, F. and Casagli, N. (2017) A tool for classification and regression using random forest methodology: Applications to landslide susceptibility mapping and soil thickness modeling. Environmental Modeling & Assessment **22**(3), 201–214.

Lari, S., Frattini, P. and Crosta, G. (2014) A probabilistic approach for landslide hazard analysis. Engineering geology **182**, 3–14.

Larsen, I. J., Montgomery, D. R. and Korup, O. (2010) Landslide erosion controlled by hillslope material. Nature Geoscience **3**(4), 247.

Li, G., West, A. J., Densmore, A. L., Hammond, D. E., Jin, Z., Zhang, F., Wang, J. and Hilton, R. G. (2016) Connectivity of earthquake-triggered landslides with the fluvial network: Implications for landslide sediment transport after the 2008 Wenchuan earthquake. Journal of Geophysical Research: Earth Surface **121**(4), 703–724.

Liao, H.-W. and Lee, C.-T. (2000) Landslides triggered by the Chi-Chi earthquake. In Proceedings of the 21st Asian conference on remote sensing, Taipei, volume 1, pp. 383–388.

Lombardo, L., Bakka, H., Tanyas, H., van Westen, C., Mai, P. M. and Huser, R. (2019a) Geostatistical modeling to capture seismic-shaking patterns from earthquake-induced landslides. Journal of Geophysical Research: Earth Surface **124**(7), 1958–1980.

Lombardo, L., Fubelli, G., Amato, G. and Bonasera, M. (2016) Presence-only approach to assess landslide triggering-thickness susceptibility: a test for the Mili catchment (north-eastern Sicily, Italy). Natural Hazards **84**(1), 565–588.

Lombardo, L. and Mai, P. M. (2018) Presenting logistic regression-based landslide susceptibility results. Engineering geology **244**, 14–24.

Lombardo, L., Opitz, T., Ardizzone, F., Guzzetti, F. and Huser, R. (2020a) Space-time landslide predictive modelling. Earth-Science Reviews p. 103318.

Lombardo, L., Opitz, T. and Huser, R. (2018a) Point process-based modeling of multiple debris flow landslides using INLA: an application to the 2009 Messina disaster. Stochastic Environmental Research and Risk Assessment **32**(7), 2179–2198.

Lombardo, L., Opitz, T. and Huser, R. (2019b) Numerical Recipes for Landslide Spatial Prediction Using R-INLA: A Step-by-Step Tutorial. In Spatial Modeling in GIS and R for Earth and Environmental Sciences, eds H. R. Pourghasemi and C. Gokceoglu, pp. 55–83. Elsevier. ISBN 978-0-12-815226-3.

Lombardo, L., Saia, S., Schillaci, C., Mai, P. M. and Huser, R. (2018b) Modeling soil organic carbon with Quantile Regression: Dissecting predictors' effects on carbon stocks. Geoderma **318**, 148–159.

Lombardo, L., Tanyas, H. and Nicu, I. C. (2020b) Spatial modeling of multi-hazard threat to cultural heritage sites. Engineering Geology p. 105776.

MacMillan, R. and Shary, P. (2009) Landforms and landform elements in geomorphometry. Developments in soil science **33**, 227–254.

Malamud, B. D., Turcotte, D. L., Guzzetti, F. and Reichenbach, P. (2004a) Landslides, earthquakes, and erosion. Earth and Planetary Science Letters **229**(1-2), 45–59.

Malamud, B. D., Turcotte, D. L., Guzzetti, F. and Reichenbach, P. (2004b) Landslide inventories and their statistical properties. Earth Surface Processes and Landforms **29**(6), 687–711.

Marc, O. and Hovius, N. (2015) Amalgamation in landslide maps: effects and automatic detection. Natural Hazards and Earth System Sciences **15**(4), 723–733.

Marc, O., Hovius, N., Meunier, P., Gorum, T. and Uchida, T. (2016) A seismologically consistent expression for the total area and volume of earthquake-triggered landsliding. Journal of Geophysical Research: Earth Surface **121**(4), 640–663.

Marjanović, M., Kovačević, M., Bajat, B. and Voženílek, V. (2011) Landslide susceptibility assessment using SVM machine learning algorithm. Engineering Geology **123**(3), 225–234.

Martin, Y., Rood, K., Schwab, J. W. and Church, M. (2002) Sediment transfer by shallow landsliding in the Queen Charlotte Islands, British Columbia. Canadian Journal of Earth Sciences **39**(2), 189–205.

Massey, C., Townsend, D., Rathje, E., Allstadt, K. E., Lukovic, B., Kaneko, Y., Bradley, B., Wartman, J., Jibson, R. W., Petley, D. et al. (2018) Landslides triggered by the 14 november 2016 mw 7.8 kaikōura earthquake, new zealandlandslides triggered by the 14 november 2016 mw 7.8 kaikōura earthquake, new zealand. Bulletin of the Seismological Society of America **108**(3B), 1630–1648.

McCrink, P. (2001) Regional earthquake-induced landslide mapping using Newmark displacement criteria, Santa Cruz County, California. Engineering Geology Practice in Northern California: California Division of Mines and Geology Bulletin **210**, 77–93.

Medwedeff, W. G., Clark, M. K., Zekkos, D. and West, A. J. (2020) Characteristic landslide distributions: An investigation of landscape controls on landslide size. Earth and Planetary Science Letters **539**, 116203.

Meunier, P., Hovius, N. and Haines, A. J. (2007) Regional patterns of earthquake-triggered landslides and their relation to ground motion. Geophysical Research Letters **34**(20).

Nadim, F., Kjekstad, O., Peduzzi, P., Herold, C. and Jaedicke, C. (2006) Global landslide and avalanche hotspots. Landslides **3**(2), 159–173.

National Research Council (1991) A Safer Future. Reducing the Impacts of Natural Disasters. Washington, D.C.: National Academy Press. ISBN 978-0-309-04546-9.

Newhall, C. G. and Self, S. (1982) The volcanic explosivity index (vei) an estimate of explosive magnitude for historical volcanism. Journal Geophysical Research **87**(C2), 1231–1238.

NIED (2016) Distribution map of mass movement by the 2016 Kumamoto earthquake, edited by National Research Institute for Earth Science and Disaster of Japan, http://www.bosai.go.jp/mizu/ dosha.html. (in Japanese) .

Nowicki, M. A., Wald, D. J., Hamburger, M. W., Hearne, M. and Thompson, E. M. (2014) Development of a globally applicable model for near real-time prediction of seismically induced landslides. Engineering Geology **173**, 54–65.

Ohlmacher, G. C. (2007) Plan curvature and landslide probability in regions dominated by earth flows and earth slides. Engineering Geology **91**(2), 117–134.

Papathanassiou, G., Valkaniotis, S., Ganas, A. and Pavlides, S. (2013) GIS-based statistical analysis of the spatial distribution of earthquake-induced landslides in the island of Lefkada, Ionian Islands, Greece. Landslides **10**(6), 771–783.

Parise, M. and Jibson, R. W. (2000) A seismic landslide susceptibility rating of geologic units based on analysis of characteristics of landslides triggered by the 17 January, 1994 Northridge, California earthquake. Engineering geology **58**(3-4), 251–270.

Parker, R. N., Densmore, A. L., Rosser, N. J., De Michele, M., Li, Y., Huang, R., Whadcoat, S. and Petley, D. N. (2011) Mass wasting triggered by the 2008 Wenchuan earthquake is greater than orogenic growth. Nature Geoscience **4**(7), 449–452.

Pelletier, J. D., Malamud, B. D., Blodgett, T. and Turcotte, D. L. (1997) Scale-invariance of soil moisture variability and its implications for the frequency-size distribution of landslides. Engineering Geology **48**(3-4), 255–268.

Pereira, S., Zêzere, J. L. and Quaresma, I. (2017) Landslide Societal Risk in Portugal in the Period 1865–2015. In Workshop on World Landslide Forum, pp. 491–499.

Petley, D. (2012) Global patterns of loss of life from landslides. Geology **40**(10), 927–930.

Reichenbach, P., Galli, M., Cardinali, M., Guzzetti, F. and Ardizzone, F. (2005) Geomorphologic mapping to assess landslide risk: concepts, methods and applications in the Umbria Region of central Italy. Landslide Risk Assessment. John Wiley, Chichester pp. 429–468.

Reichenbach, P., Rossi, M., Malamud, B. D., Mihir, M. and Guzzetti, F. (2018) A review of statistically-based landslide susceptibility models. Earth-Science Reviews **180**, 60–91.

Rickli, C., Graf, F. et al. (2009) Effects of forests on shallow landslides–case studies in Switzerland. Forest Snow and Landscape Research **82**(1), 33–44.

Roback, K., Clark, M., West, A., Zekkos, D., Li, G., Gallen, S. and Godt, J. (2017) Map data of landslides triggered by the 25 April 2015 Mw 7.8 Gorkha, Nepal earthquake. US Geological Survey data release .

Roback, K., Clark, M. K., West, A. J., Zekkos, D., Li, G., Gallen, S. F., Chamlagain, D. and Godt, J. W. (2018) The size, distribution, and mobility of landslides caused by the 2015 Mw7.8 Gorkha earthquake, Nepal. Geomorphology **301**, 121–138.

Rossi, M., Cardinali, M., Fiorucci, F., Marchesini, I., Mondini, A. C., Santangelo, M., Ghosh, S., Riguer, D. E. L., Lahousse, T., Chang, K.-T. and Guzzetti, F. (2012) A tool for the estimation of the distribution of landslide area in R. In EGU General Assembly Conference — Geophysical Research Abstracts, volume 14, pp. EGU2012–9438–1. Vienna: .

Rossi, M., Guzzetti, F., Salvati, P., Donnini, M., Napolitano, E. and Bianchi, C. (2019) A predictive model of societal landslide risk in Italy. Earth-Science Reviews .

Rossi, M., Witt, A., Guzzetti, F., Malamud, B. D. and Peruccacci, S. (2010) Analysis of historical landslide time series in the emilia-romagna region, northern italy. Earth Surface Processes and Landforms **35**, 1123–1137.

Rue, H., Martino, S. and Chopin, N. (2009) Approximate Bayesian inference for latent Gaussian models by using integrated nested Laplace approximations. Journal of the Royal Statistical Society: Series B **71**(2), 319–392.

Rue, H., Riebler, A., Sørbye, S. H., Illian, J. B., Simpson, D. P. and Lindgren, F. K. (2017) Bayesian computing with INLA: A review. Annual Review of Statistics and Its Application **4**, 395–421.

Saffir, H. S. (1973) Hurricane wind and storm surge. Military Engineering **423**, 4–5.

Salvati, P., Bianchi, C., Rossi, M. and Guzzetti, F. (2010) Societal landslide and flood risk in Italy. Natural Hazards and Earth System Sciences **10**, 465–483.

Salvati, P., Petrucci, O., Rossi, M., Bianchi, C., Pasqua, A. A. and Guzzetti, F. (2018) Gender, age and circumstances analysis of flood and landslide fatalities in Italy. Science of the Total Environment **610-611**, 867–879.

Samia, J., Temme, A., Bregt, A., Wallinga, J., Guzzetti, F. and Ardizzone, F. (2020) Dynamic path-dependent landslide susceptibility modelling. Natural Hazards and Earth System Sciences **20**(1), 271–285.

Santangelo, M., Marchesini, I., Bucci, F., Cardinali, M., Fiorucci, F. and Guzzetti, F. (2015) An approach to reduce mapping errors in the production of landslide inventory maps. Natural Hazards & Earth System Sciences **15**(9).

Sappington, J. M., Longshore, K. M. and Thompson, D. B. (2007) Quantifying landscape ruggedness for animal habitat analysis: a case study using bighorn sheep in the Mojave Desert. The Journal of wildlife management **71**(5), 1419–1426.

Sassa, K. (1988) Speciallecture: Geotechnical model for the motion of landslides. In Proceedings 5th International Symposium on Landslides, Lausanne, volume 1, pp. 37–55. Lausanne: .

Sato, H. P., Hasegawa, H., Fujiwara, S., Tobita, M., Koarai, M., Une, H. and Iwahashi, J. (2007) Interpretation of landslide distribution triggered by the 2005 Northern Pakistan earthquake using SPOT 5 imagery. Landslides **4**(2), 113–122.

Šavrič, B., Patterson, T. and Jenny, B. (2019) The Equal Earth map projection. International Journal of Geographical Information Science **33**(3), 454–465.

Schabenberger, O. and Gotway, C. A. (2017) Statistical methods for spatial data analysis. CRC press.

Schmidt, K. M. and Montgomery, D. R. (1995) Limits to relief. Science **270**(5236), 617–620.

Schmitt, R. G., Tanyas, H., Jessee, M. A. N., Zhu, J., Biegel, K. M., Allstadt, K. E., Jibson, R. W., Thompson, E. M., van Westen, C. J., Sato, H. P., Wald, D. J., Godt, J. W., Gorum, T., Xu, C., Rathje, E. M. and Knudsen, K. L. (2017) An open repository of earthquake-triggered ground-failure inventories. U.S. Geological Survey Data Series 1064 .

Shangguan, W., Hengl, T., de Jesus, J. M., Yuan, H. and Dai, Y. (2017) Mapping the global depth to bedrock for land surface modeling. Journal of Advances in Modeling Earth Systems **9**(1), 65–88.

Simpson, R. (1974) The hurricane disaster potential scale. Weatherwise **27**(8), 169,186.

Soeters, R. and Van Westen, C. (1996) Slope instability recognition, analysis and zonation. Landslides: investigation and mitigation **247**, 129–177.

Soeters, R. and van Westen, C. J. (1996) Slope instability recognition, analysis and zonation. In Landslide Investigation and Mitigation., number 247 in Transportation Research Board Special Report, pp. 129–177. National Research Council, Transportation Research Board.

Spiegelhalter, D. J., Best, N. G., Carlin, B. P. and Van Der Linde, A. (2002) Bayesian measures of model complexity and fit. Journal of the royal statistical society: Series b (statistical methodology) **64**(4), 583–639.

Stark, C. and Guzzetti, F. (2009) Landslide rupture and the probability distribution of mobilized debris volumes. Journal of Geophysical Research: Earth Surface **114**(F2).

Stark, C. P. and Hovius, N. (2001) The characterization of landslide size distributions. Geophysical Research Letters **28**(6), 1091–1094.

Steger, S., Brenning, A., Bell, R. and Glade, T. (2016) The propagation of inventory-based positional errors into statistical landslide susceptibility models. Natural Hazards and Earth System Sciences **16**(12), 2729–2745.

Stepinski, T. F. and Jasiewicz, J. (2011) Geomorphons-a new approach to classification of landforms. Proceedings of geomorphometry **2011**, 109–112.

Suziki, K. (1979) On the disaster situation/land condition map of the Izu-Oshima Kinkai earthquake, 1978. Journal of the Japan Cartographers Association **17**(2), 16–22.

Tang, C., Tanyas, H., van Westen, C. J., Tang, C., Fan, X. and Jetten, V. G. (2019) Analysing post-earthquake mass movement volume dynamics with multi-source DEMs. Engineering geology **248**, 89–101.

Tanyaş, H., van Westen, C., Allstadt, K., Nowicki, A. J. M., Görüm, T., Jibson, R., Godt, J., Sato, H., Schmitt, R., Marc, O. and Hovius, N. (2017) Presentation and Analysis of a Worldwide Database of Earthquake-Induced Landslide Inventories. Journal of Geophysical Research: Earth Surface **122**(10), 1991–2015.

Tanyaş, H., Allstadt, K. E. and van Westen, C. J. (2018) An updated method for estimating landslide-event magnitude. Earth surface processes and landforms **43**(9), 1836–1847.

Tanyaş, H. and Lombardo, L. (2019) Variation in landslide-affected area under the control of ground motion and topography. Engineering Geology **260**, In print.

Tanyaş, H. and Lombardo, L. (2020) Completeness Index for Earthquake-Induced Landslide Inventories. Engineering geology **264**, 105331.

Tanyaş, H., Rossi, M., Alvioli, M., van Westen, C. J. and Marchesini, I. (2019a) A global slope unit-based method for the near real-time prediction of earthquake-induced landslides. Geomorphology **327**, 126–146.

Tanyaş, H., van Westen, C. J., Allstadt, K. E. and Jibson, R. W. (2019b) Factors controlling landslide frequency–area distributions. Earth surface processes and landforms **44**(4), 900–917.

Taylor, D. W. (1948) Fundamentals of Soil Mechanics. John Wiley & Sons.

Taylor, F. E., Malamud, B. D., Witt, A. and Guzzetti, F. (2018a) Landslide shape, ellipticity and length–to–width ratios. Earth Surface Processes and Landforms **43**(15), 3164–3189.

Taylor, F. E., Malamud, B. D., Witt, A. and Guzzetti, F. (2018b) Landslide shape, ellipticity and length-to-width ratios. Earth Surface Processes and Landforms **43**(15), 3164–3189.

Townsend, K. F., Gallen, S. F. and Clark, M. K. (2020) Quantifying near-surface rock strength on a regional scale from hillslope stability models. Journal of Geophysical Research: Earth Surface **125**(7), e2020JF005665.

Uchida, T., Kataoka, S., Iwao, T., Matsuo, O., Terada, H., Nakano, Y., Sugiura, N. and Osanai, N. (2004) A study on methodology for assessing the potential of slope failures during earthquakes. Technical note of National Institute for Land and Infrastructure Management **91**.

UNESCO Working Party On World Landslide Inventory (1995) A suggested method for describing the rate of movement of a landslide. Bulletin of the International Association of Engineering Geology **52**, 75–78.

Valagussa, A., Marc, O., Frattini, P. and Crosta, G. (2019) Seismic and geological controls on earthquake-induced landslide size. Earth and Planetary Science Letters **506**, 268–281.

Van De Wiel, M. J., Coulthard, T. J., Macklin, M. G. and Lewin, J. (2007) Embedding reach-scale fluvial dynamics within the CAESAR cellular automaton landscape evolution model. Geomorphology **90**(3-4), 283–301.

Van Niekerk, J., Bakka, H., Rue, H. and Schenk, L. (2019) New frontiers in bayesian modeling using the inla package in R. arXiv preprint arXiv:1907.10426 .

Varnes and the IAEG Commission on Landslides and Other Mass-Movements (1984) Landslide hazard zonation: A review of principles and practice. Natural Hazards, Series. Paris: United Nations Economic, Scientific and cultural organization. UNESCO **3**, 63.

Wald, D. J., Quitoriano, V., Heaton, T. H. and Kanamori, H. (1999) Relationships between peak ground acceleration, peak ground velocity, and modified mercalli intensity in california. Earthquake spectra **15**(3), 557–564.

Wald, D. J., Quitoriano, V., Worden, C. B., Hopper, M. and Dewey, J. W. (2012) USGS "Did You Feel It?" internet-based macroseismic intensity maps. Annals of Geophysics **54**(6).

Wan, J.-Z. and Wang, C.-J. (2018) Expansion risk of invasive plants in regions of high plant diversity: a global assessment using 36 species. Ecological informatics **46**, 8–18.

Wang, J., Jin, Z., Hilton, R. G., Zhang, F., Densmore, A. L., Li, G. and West, A. J. (2015) Controls on fluvial evacuation of sediment from earthquake-triggered landslides. Geology **43**(2), 115–118.

Wartman, J., Dunham, L., Tiwari, B. and Pradel, D. (2013) Landslides in eastern Honshu induced by the 2011 Tohoku earthquake. Bulletin of the Seismological Society of America **103**(2B), 1503–1521.

Watanabe, S. (2010) Asymptotic equivalence of bayes cross validation and widely applicable information criterion in singular learning theory. Journal of Machine Learning Research **11**(Dec), 3571–3594.

Watanabe, S. (2013) A widely applicable bayesian information criterion. Journal of Machine Learning Research **14**(Mar), 867–897.

van Westen, C., Castellanos, E. and Kuriakose, S. (2008) Spatial data for landslide susceptibility, hazard, and vulnerability assessment: An overview. Engineering Geology **102**(3-4), 112–131.

Williams, J. G., Rosser, N. J., Hardy, R. J., Brain, M. J. and Afana, A. A. (2018) Optimising 4-d surface change detection: an approach for capturing rockfall magnitude–frequency. Earth Surface Dynamics **6**(1), 101–119.

Wood, H. O. and Neumann, F. (1931) Modified mercalli intensity scale of 1931. Bulletin of the Seismological Society of America **21**(4), 277–283.

Worden, C. and Wald, D. (2016) ShakeMap manual online: Technical manual, users guide, and software guide. US Geol. Surv. .

Xu, C., Xu, X. and Shyu, J. B. H. (2015) Database and spatial distribution of landslides triggered by the Lushan, China Mw 6.6 earthquake of 20 april 2013. Geomorphology **248**, 77–92.

Xu, C., Xu, X., Shyu, J. B. H., Zheng, W. and Min, W. (2014a) Landslides triggered by the 22 July 2013 Minxian-Zhangxian, China, Mw 5.9 earthquake: inventory compiling and spatial distribution analysis. Journal of Asian Earth Sciences **92**, 125–142.

Xu, C., Xu, X., Tian, Y., Shen, L., Yao, Q., Huang, X., Ma, J., Chen, X. and Ma, S. (2016) Two comparable earthquakes produced greatly different coseismic landslides: The 2015 Gorkha, Nepal and 2008 Wenchuan, China events. Journal of Earth Science **27**(6), 1008–1015.

Xu, C., Xu, X., Yao, X. and Dai, F. (2014b) Three (nearly) complete inventories of landslides triggered by the May 12, 2008 Wenchuan Mw 7.9 earthquake of China and their spatial distribution statistical analysis. Landslides **11**(3), 441–461.

Xu, C., Xu, X. and Yu, G. (2013) Landslides triggered by slipping-fault-generated earthquake on a plateau: an example of the 14 April 2010, Ms 7.1, Yushu, China earthquake. Landslides **10**(4), 421–431.

Yagi, H., Sato, G., Higaki, D., Yamamoto, M. and Yamasaki, T. (2009) Distribution and characteristics of landslides induced by the Iwate–Miyagi Nairiku Earthquake in 2008 in Tohoku District, Northeast Japan. Landslides **6**(4), 335.

Ying-ying, T., Chong, X., Xi-wei, X., Sai-er, W. and Jian, C. (2015) Spatial distribution analysis of coseismic and pre-earthquake landslides triggered by the 2014 Ludian MS 6.5 earthquake. Seismology and Geology **37**(1), 291–306.

Zevenbergen, L. W. and Thorne, C. R. (1987) Quantitative analysis of land surface topography. Earth surface processes and landforms **12**(1), 47–56.

Supplementary Material of "Landslide size matters: a new spatial predictive paradigm"

Luigi Lombardo[1*], Hakan Tanyas[2,3], Raphaël Huser[4], Fausto Guzzetti[5,6], Daniela Castro-Camilo[7]

October 27, 2020

Keywords: Integrated nested Laplace approximation (INLA), Landslide Hazard, Earthquake, Landslide Area Prediction, Slope unit, Bayesian spatial modelling

[1]University of Twente, Faculty of Geo-Information Science and Earth Observation (ITC), PO Box 217, Enschede, AE 7500, Netherlands

[2]Hydrological Sciences Laboratory, NASA Goddard Space Flight Center, Greenbelt, MD, United States

[3]USRA, Universities Space Research Association, Columbia, MD, United States

[4]King Abdullah University of Science and Technology (KAUST), Computer, Electrical and Mathematical Sciences and Engineering (CEMSE) Division, Thuwal 23955-6900, Saudi Arabia

[5]Consiglio Nazionale delle Ricerche (CNR), Istituto di Ricerca per la Protezione Idrogeologica (IRPI), via Madonna Alta 126, 06128 Perugia, Italy

[6]Presidenza del Consiglio dei Ministri, Dipartimento della Protezione Civile, via Vitorchiano 2, 00189 Roma, Italy

[7]School of Mathematics and Statistics, University of Glasgow, Glasgow, G12 8QQ, UK

1 Landslide Area Predictive Mapping

Below we graphically summarize, in alphabetic order, the estimates of the *sum* and *max* models for the earthquakes we did not report in the main manuscript.

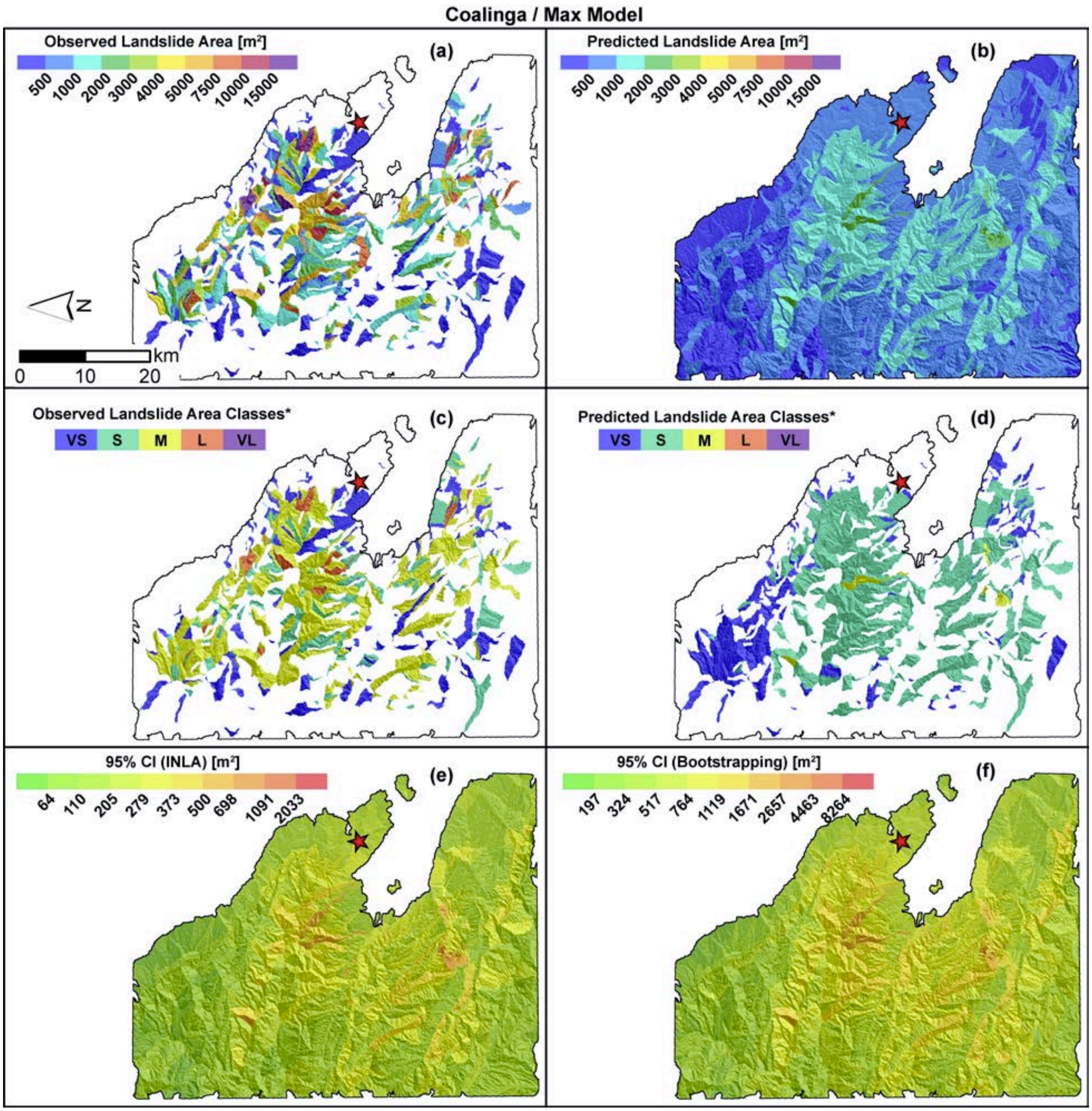

Figure SM1: Coalinga Max maps: (a) Observed maximum landslide area per SU. (b) Predicted maximum landslide area per SU. (c) Classified observed maximum landslide area per SU. (d) Classified predicted maximum landslide area per SU. (d) 95% credible interval estimated with INLA. (e) 95% credible interval estimated via bootstrap.

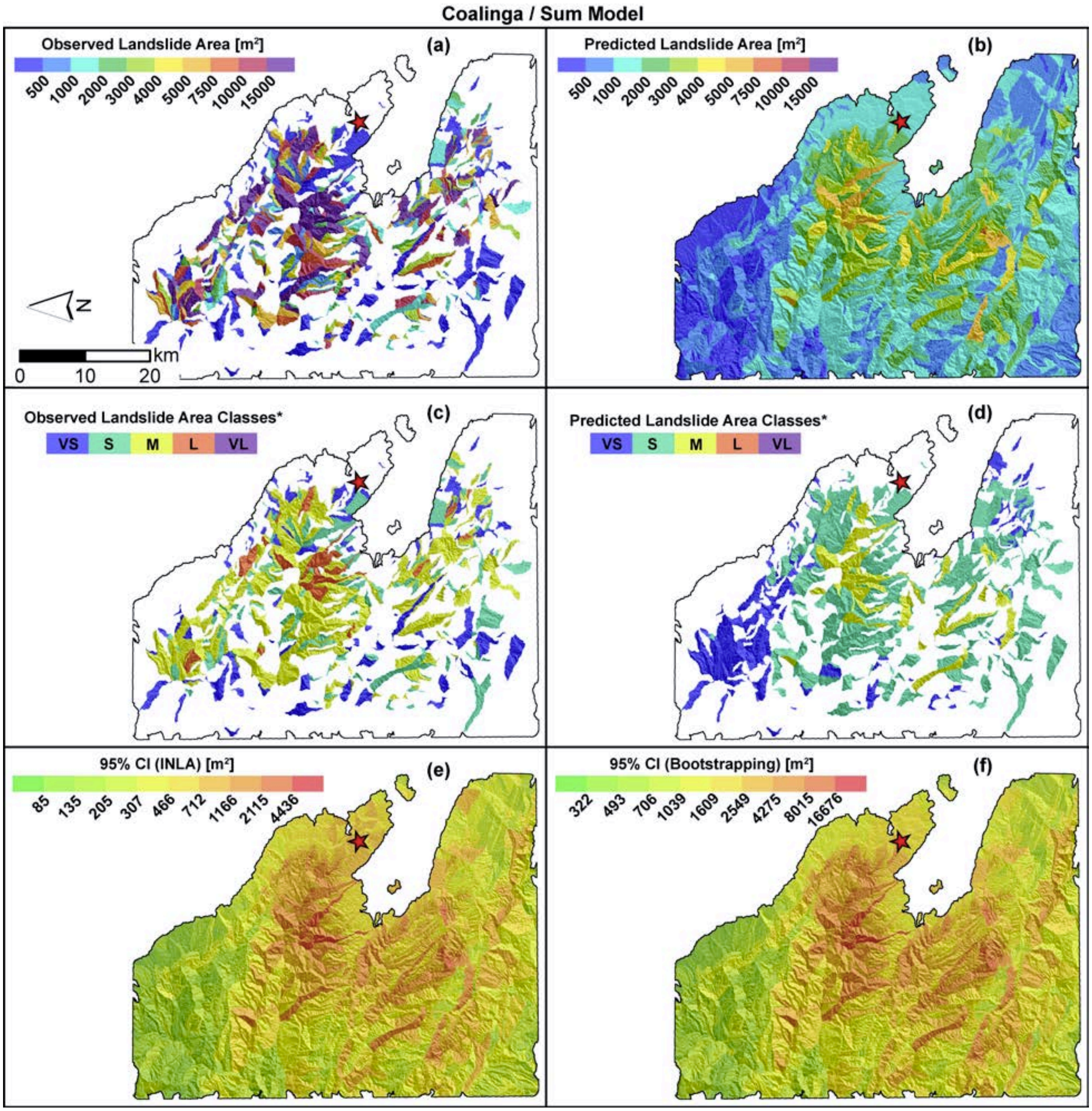

Figure SM2: Coalinga Sum maps: (a) Observed maximum landslide area per SU. (b) Predicted maximum landslide area per SU. (c) Classified observed maximum landslide area per SU. (d) Classified predicted maximum landslide area per SU. (d) 95% credible interval estimated with INLA. (e) 95% credible interval estimated via bootstrap.

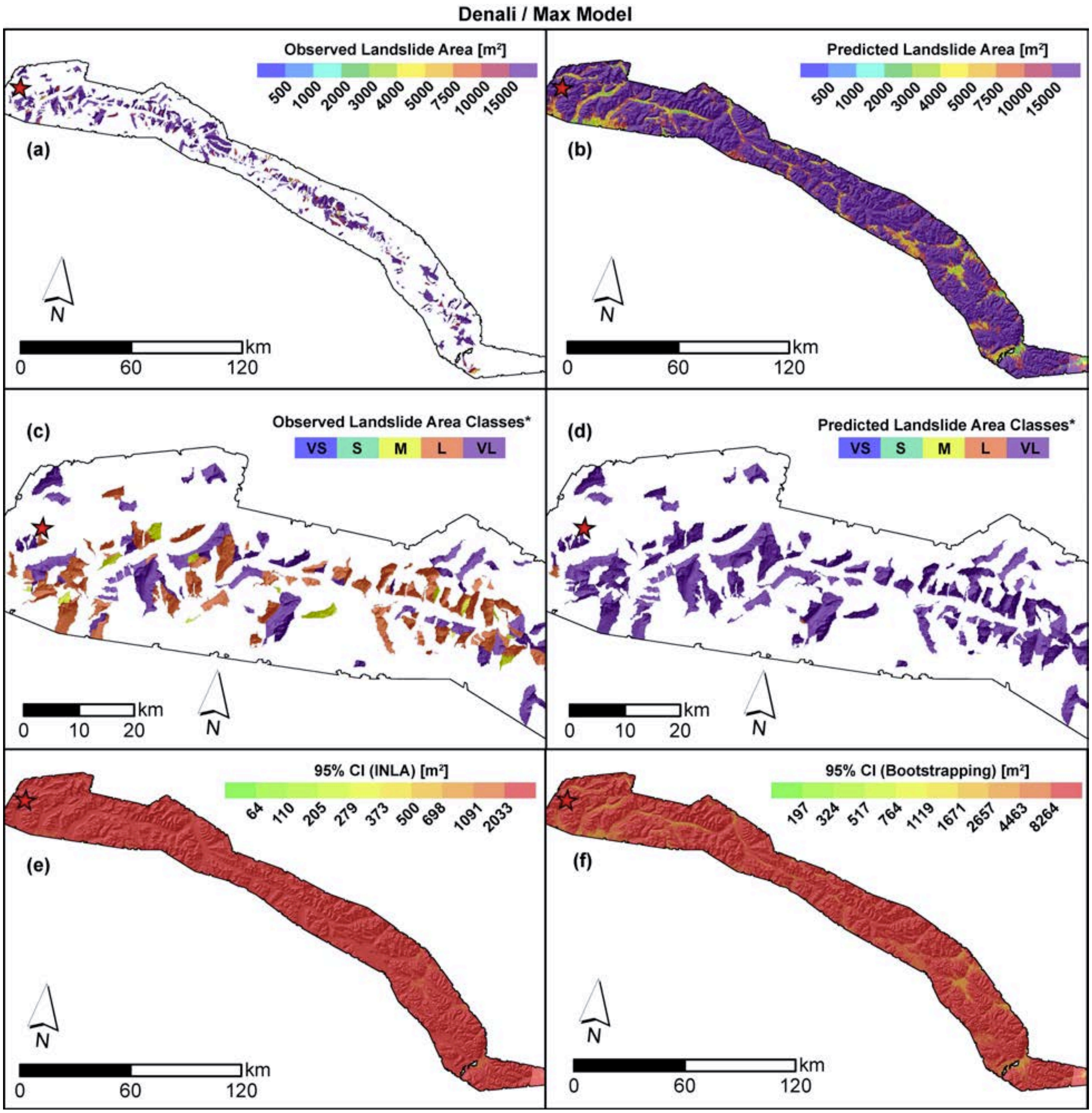

Figure SM3: Denali max maps: (a) Observed maximum landslide area per SU. (b) Predicted maximum landslide area per SU. (c) Classified observed maximum landslide area per SU. (d) Classified predicted maximum landslide area per SU. (d) 95% credible interval estimated with INLA. (e) 95% credible interval estimated via bootstrap.

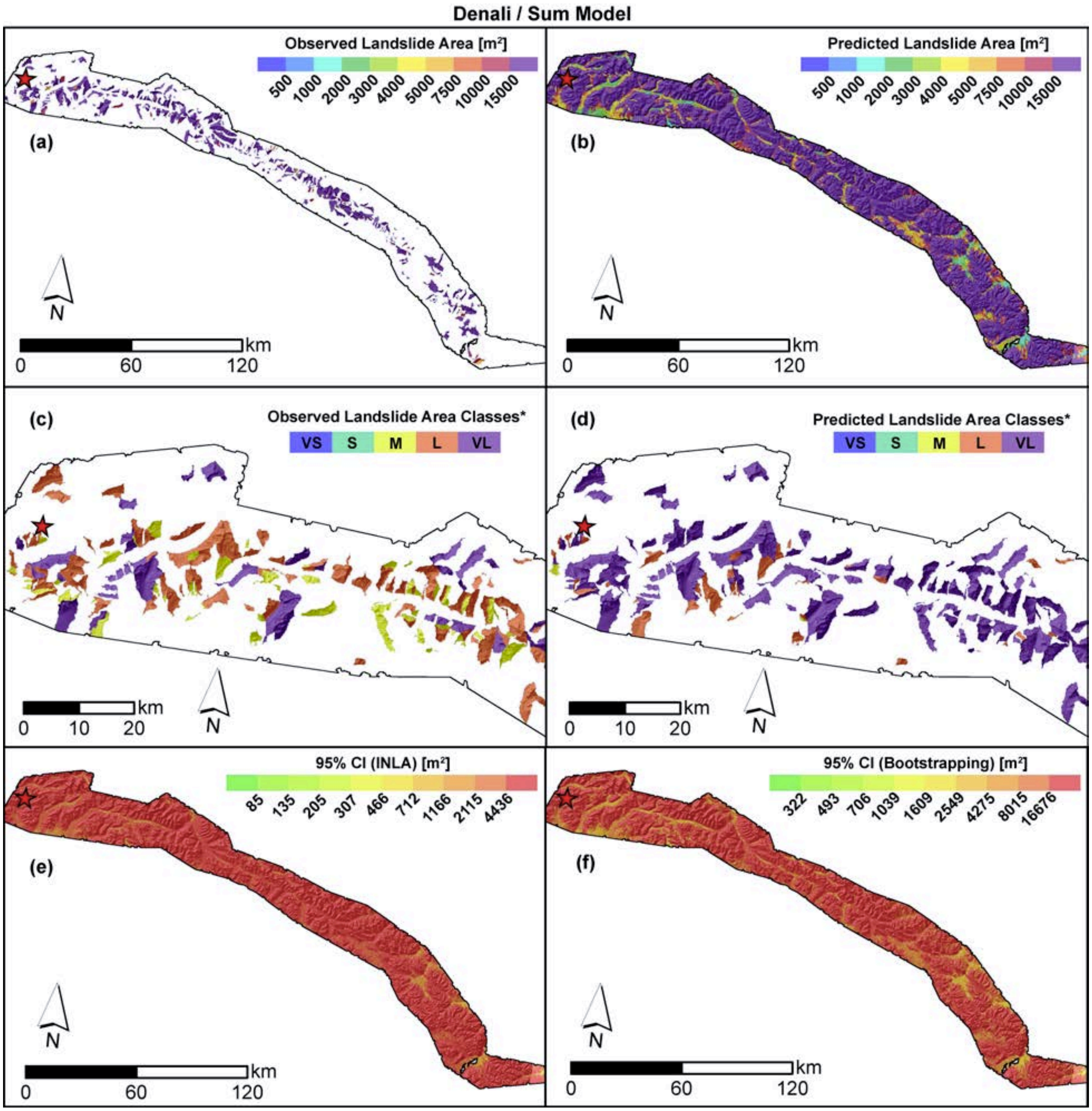

Figure SM4: Denali sum maps: (a) Observed maximum landslide area per SU. (b) Predicted maximum landslide area per SU. (c) Classified observed maximum landslide area per SU. (d) Classified predicted maximum landslide area per SU. (d) 95% credible interval estimated with INLA. (e) 95% credible interval estimated via bootstrap.

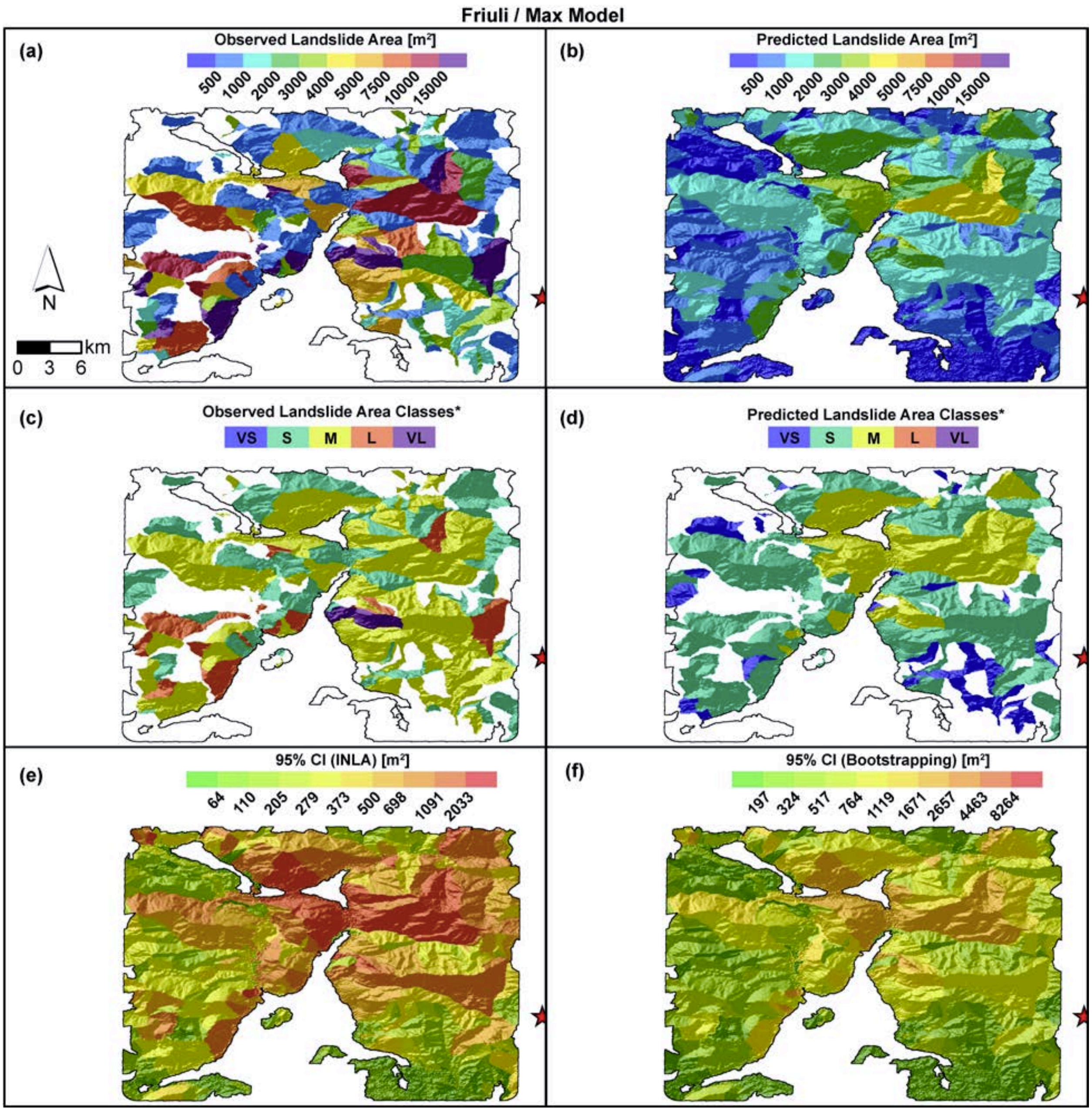

Figure SM5: Friuli max maps: (a) Observed maximum landslide area per SU. (b) Predicted maximum landslide area per SU. (c) Classified observed maximum landslide area per SU. (d) Classified predicted maximum landslide area per SU. (d) 95% credible interval estimated with INLA. (e) 95% credible interval estimated via bootstrap.

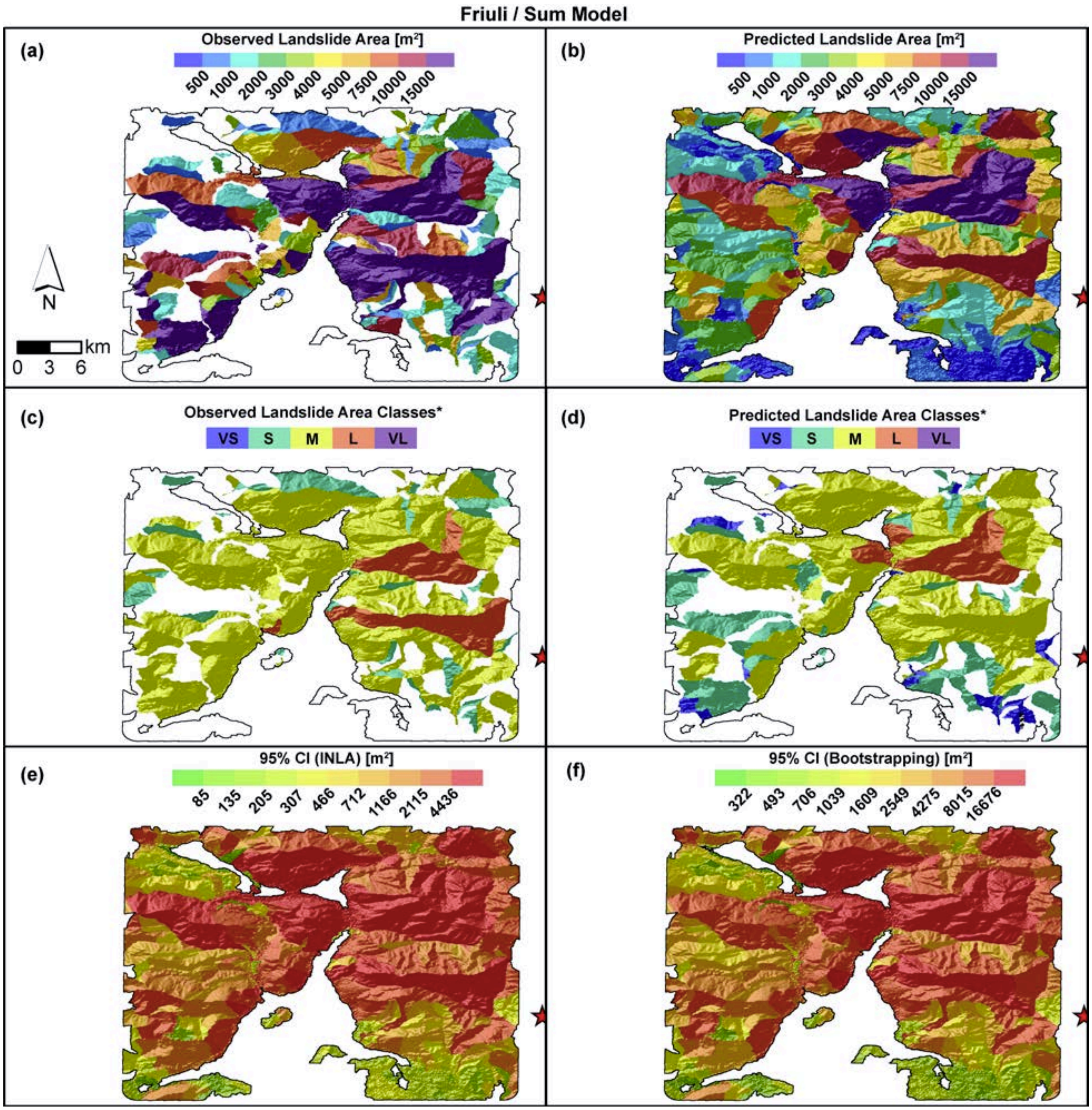

Figure SM6: Friuli sum maps: (a) Observed maximum landslide area per SU. (b) Predicted maximum landslide area per SU. (c) Classified observed maximum landslide area per SU. (d) Classified predicted maximum landslide area per SU. (d) 95% credible interval estimated with INLA. (e) 95% credible interval estimated via bootstrap.

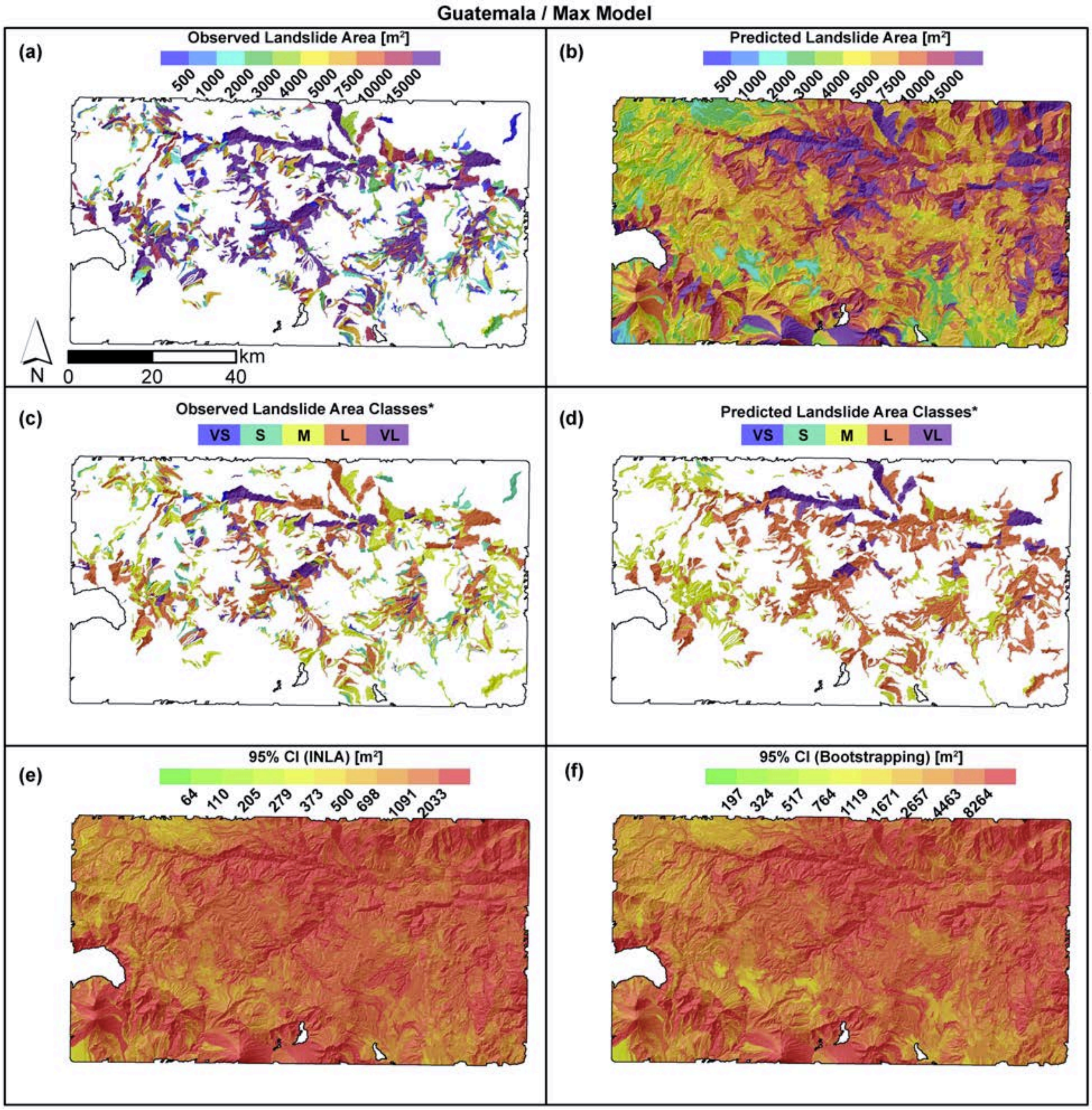

Figure SM7: Guatemala max maps: (a) Observed maximum landslide area per SU. (b) Predicted maximum landslide area per SU. (c) Classified observed maximum landslide area per SU. (d) Classified predicted maximum landslide area per SU. (d) 95% credible interval estimated with INLA. (e) 95% credible interval estimated via bootstrap.

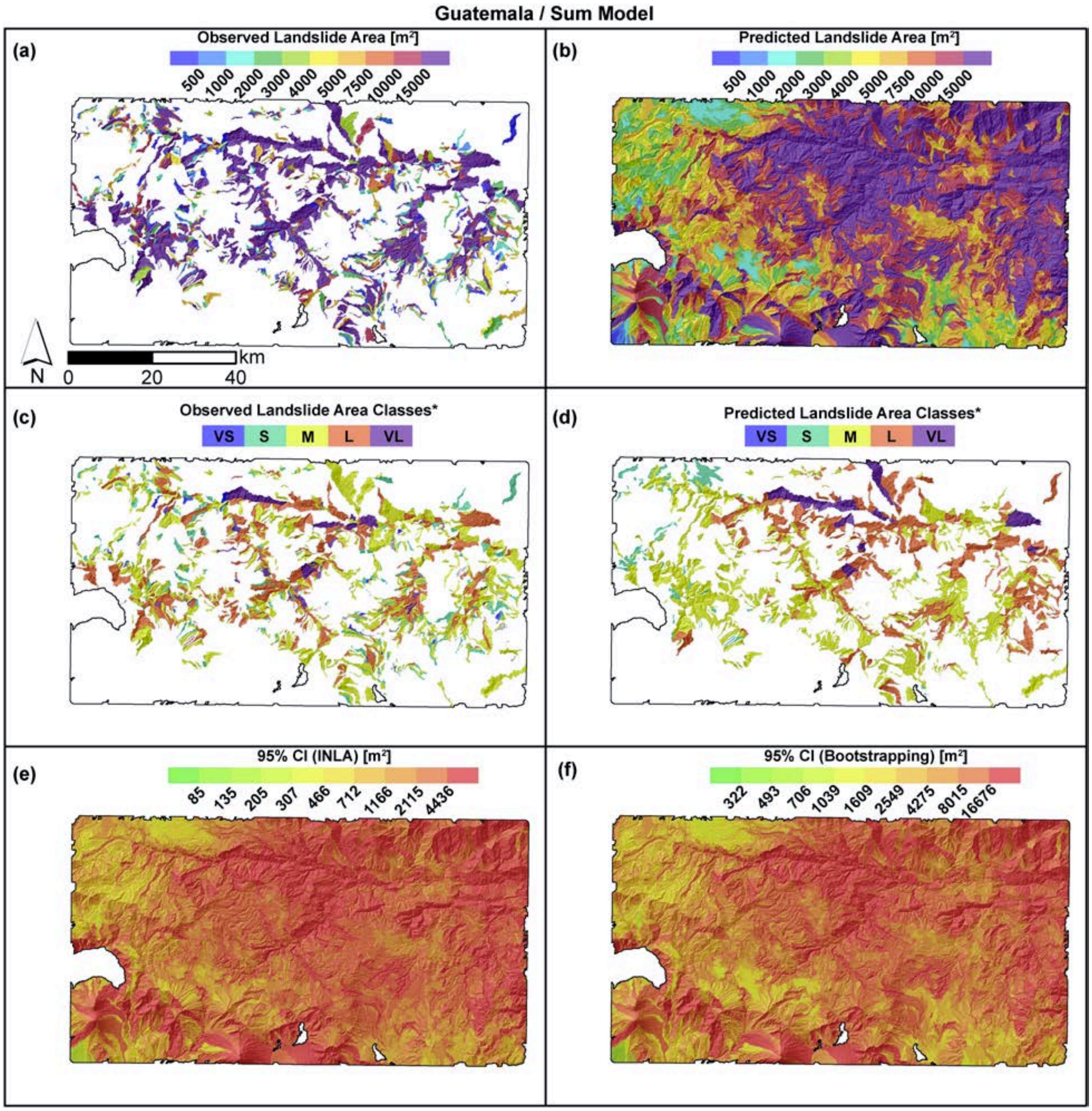

Figure SM8: Guatemala sum maps: (a) Observed maximum landslide area per SU. (b) Predicted maximum landslide area per SU. (c) Classified observed maximum landslide area per SU. (d) Classified predicted maximum landslide area per SU. (d) 95% credible interval estimated with INLA. (e) 95% credible interval estimated via bootstrap.

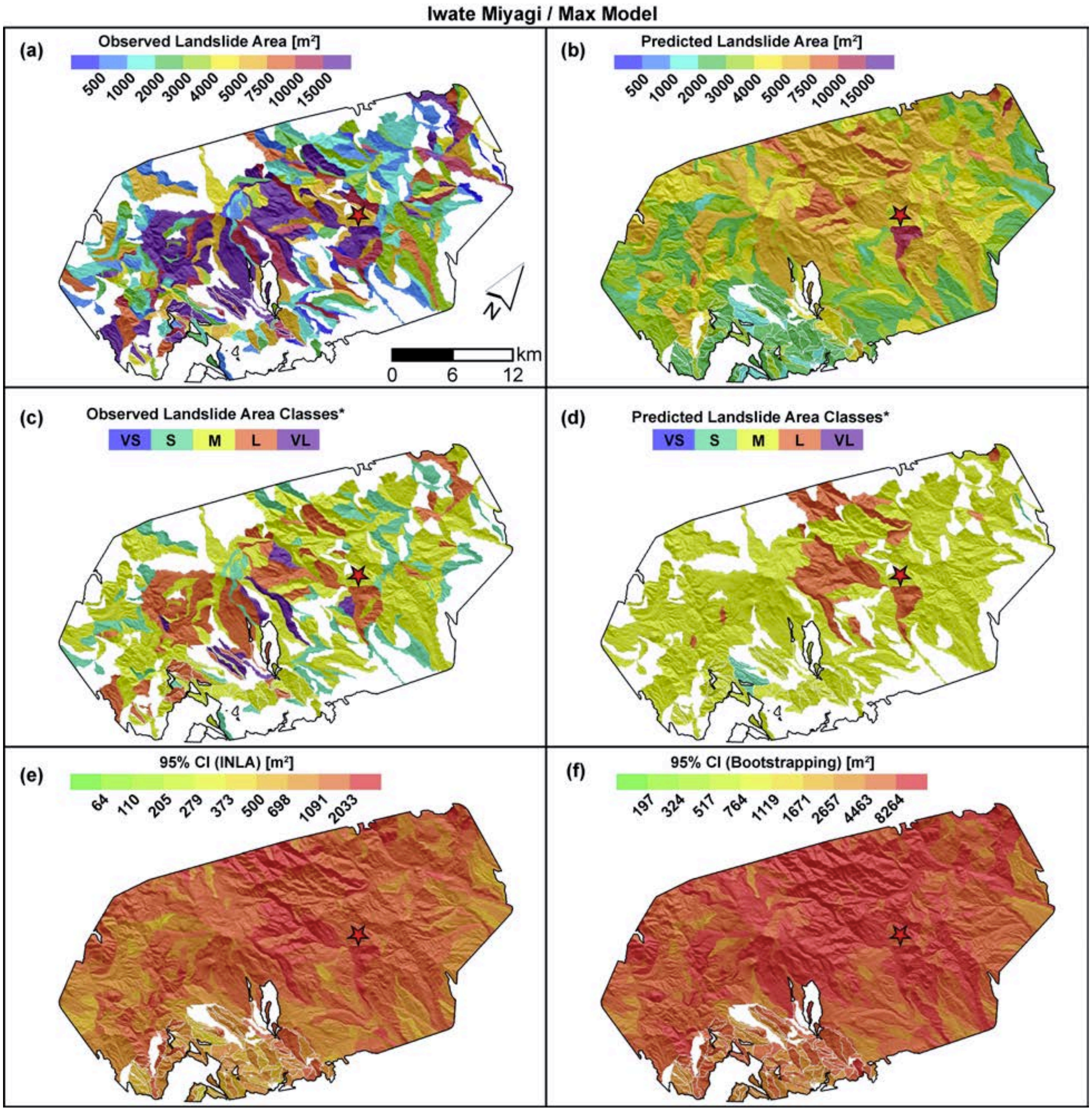

Figure SM9: Iwate Miyagi max maps: (a) Observed maximum landslide area per SU. (b) Predicted maximum landslide area per SU. (c) Classified observed maximum landslide area per SU. (d) Classified predicted maximum landslide area per SU. (d) 95% credible interval estimated with INLA. (e) 95% credible interval estimated via bootstrap.

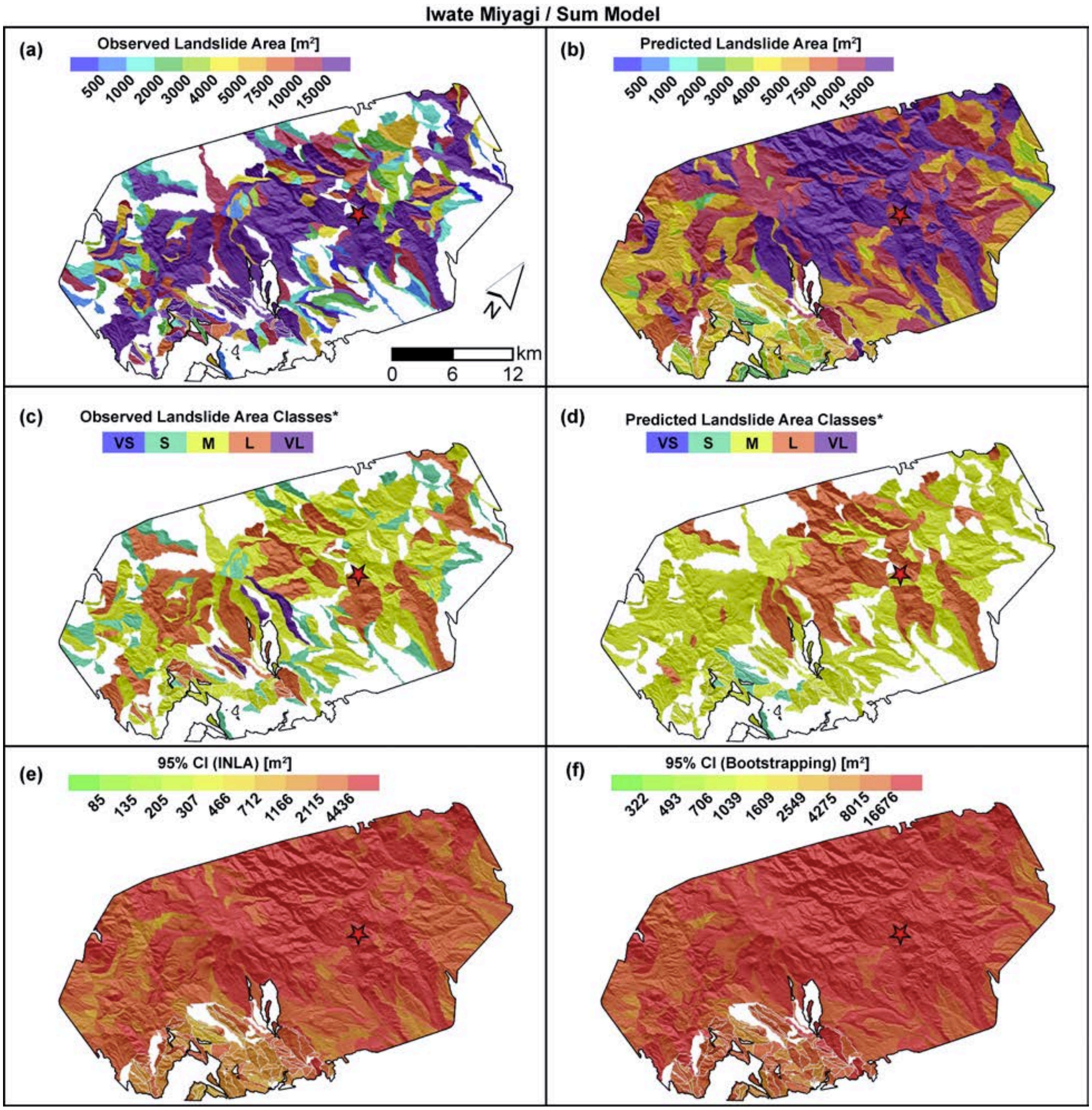

Figure SM10: Iwate Miyagi sum maps: (a) Observed maximum landslide area per SU. (b) Predicted maximum landslide area per SU. (c) Classified observed maximum landslide area per SU. (d) Classified predicted maximum landslide area per SU. (d) 95% credible interval estimated with INLA. (e) 95% credible interval estimated via bootstrap.

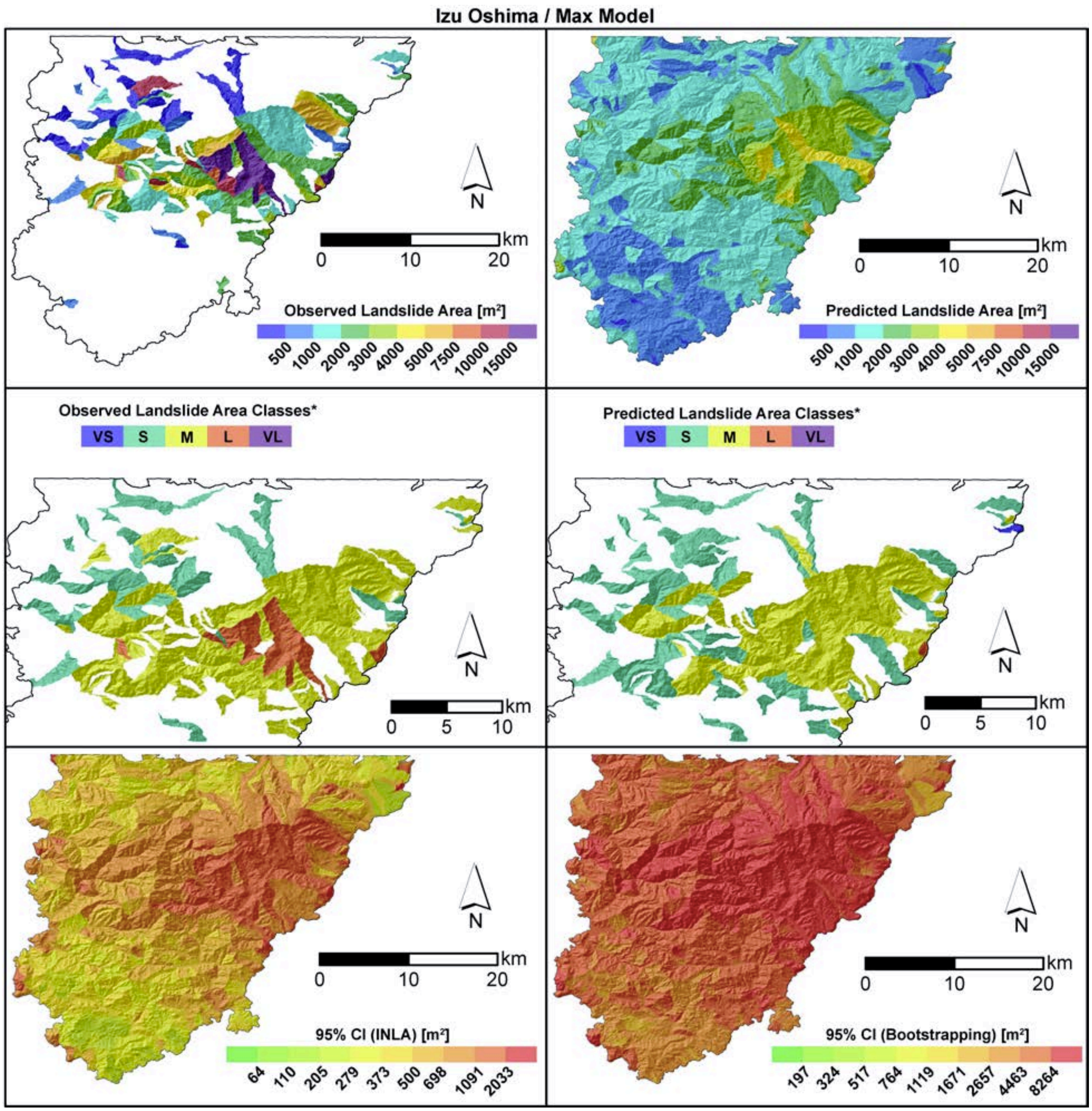

Figure SM11: Izu Oshima max maps: (a) Observed maximum landslide area per SU. (b) Predicted maximum landslide area per SU. (c) Classified observed maximum landslide area per SU. (d) Classified predicted maximum landslide area per SU. (d) 95% credible interval estimated with INLA. (e) 95% credible interval estimated via bootstrap.

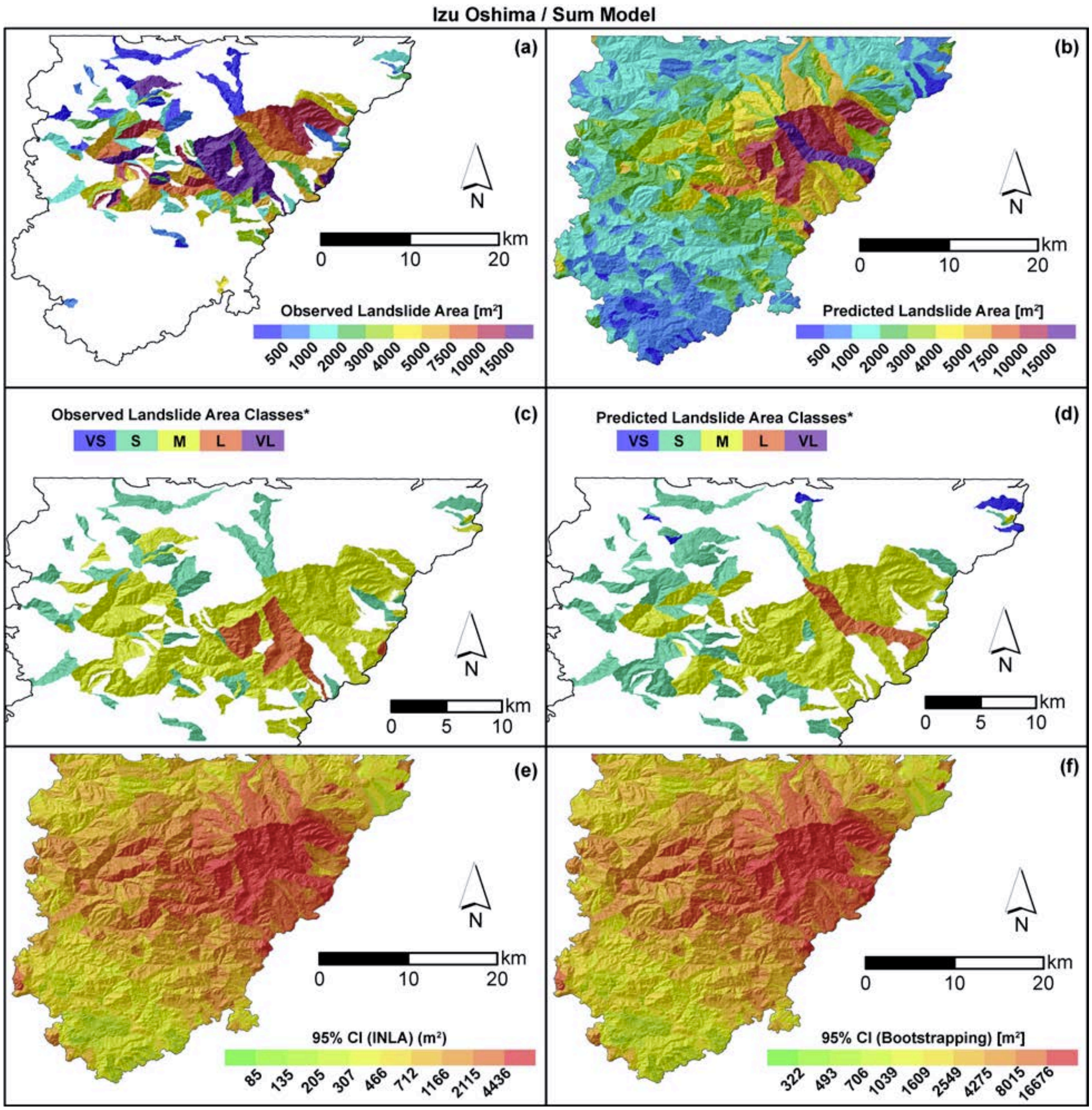

Figure SM12: Izu Oshima sum maps: (a) Observed maximum landslide area per SU. (b) Predicted maximum landslide area per SU. (c) Classified observed maximum landslide area per SU. (d) Classified predicted maximum landslide area per SU. (d) 95% credible interval estimated with INLA. (e) 95% credible interval estimated via bootstrap.

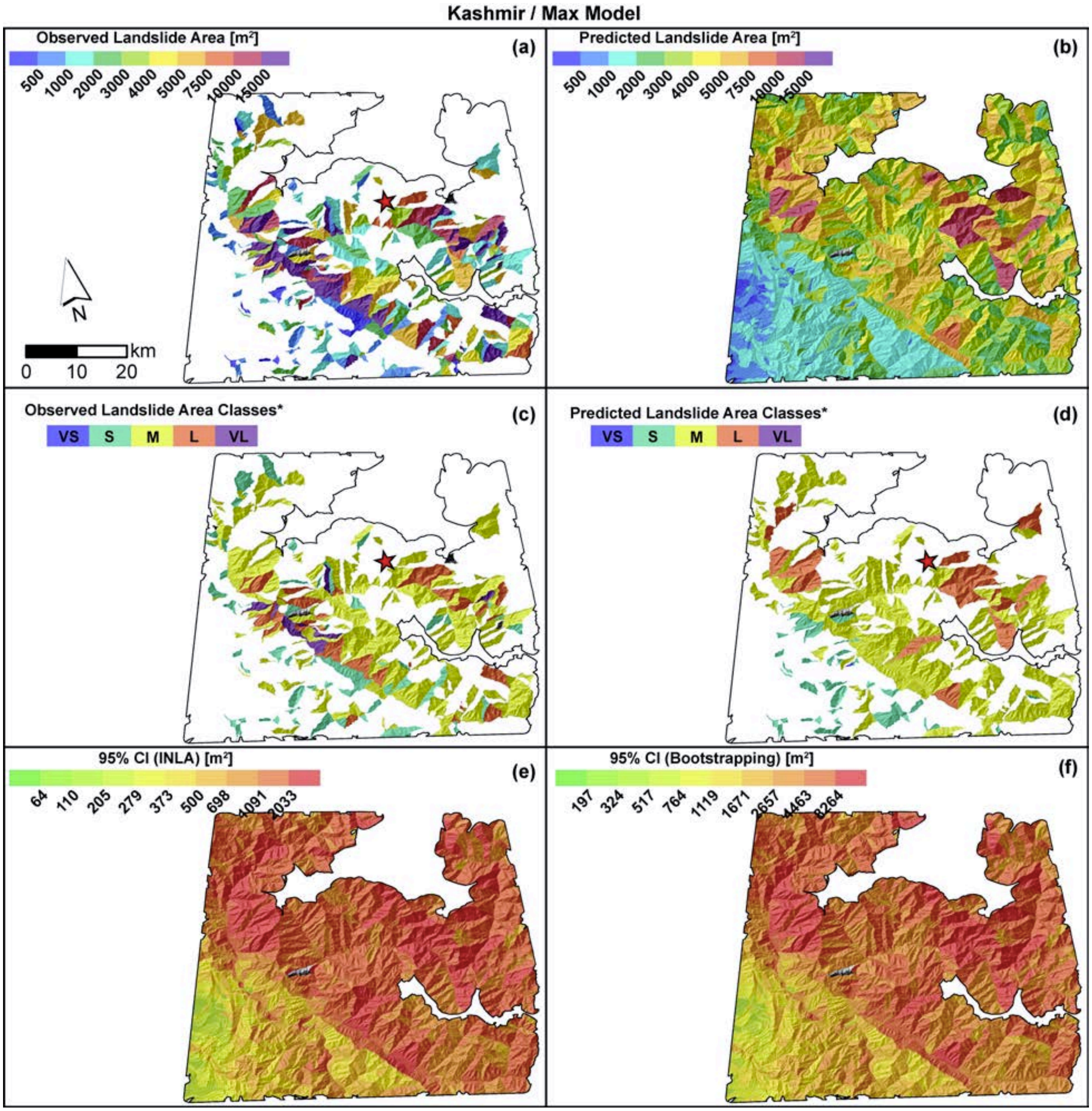

Figure SM13: Kashmir max maps: (a) Observed maximum landslide area per SU. (b) Predicted maximum landslide area per SU. (c) Classified observed maximum landslide area per SU. (d) Classified predicted maximum landslide area per SU. (d) 95% credible interval estimated with INLA. (e) 95% credible interval estimated via bootstrap.

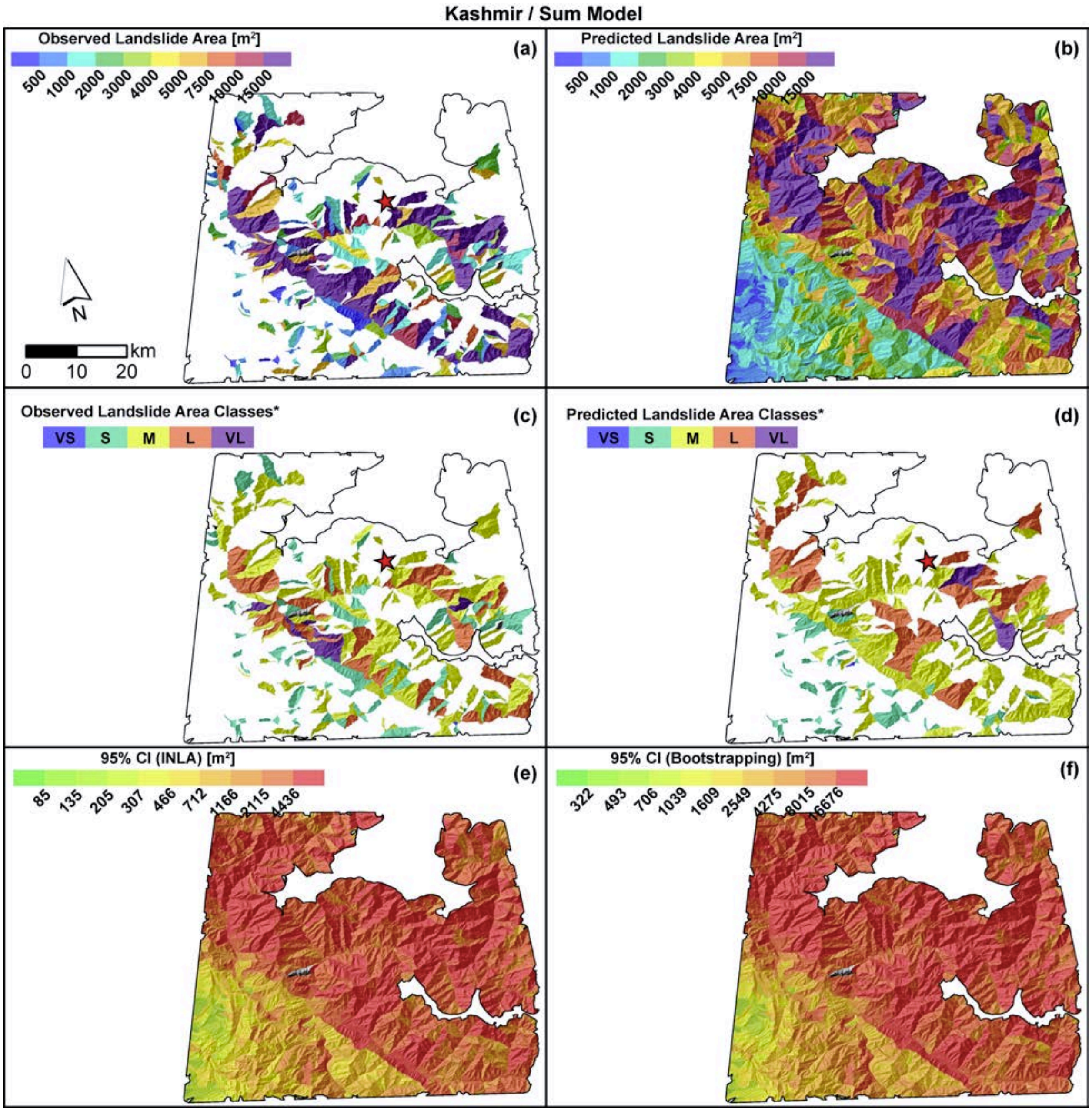

Figure SM14: Kashmir sum maps: (a) Observed maximum landslide area per SU. (b) Predicted maximum landslide area per SU. (c) Classified observed maximum landslide area per SU. (d) Classified predicted maximum landslide area per SU. (d) 95% credible interval estimated with INLA. (e) 95% credible interval estimated via bootstrap.

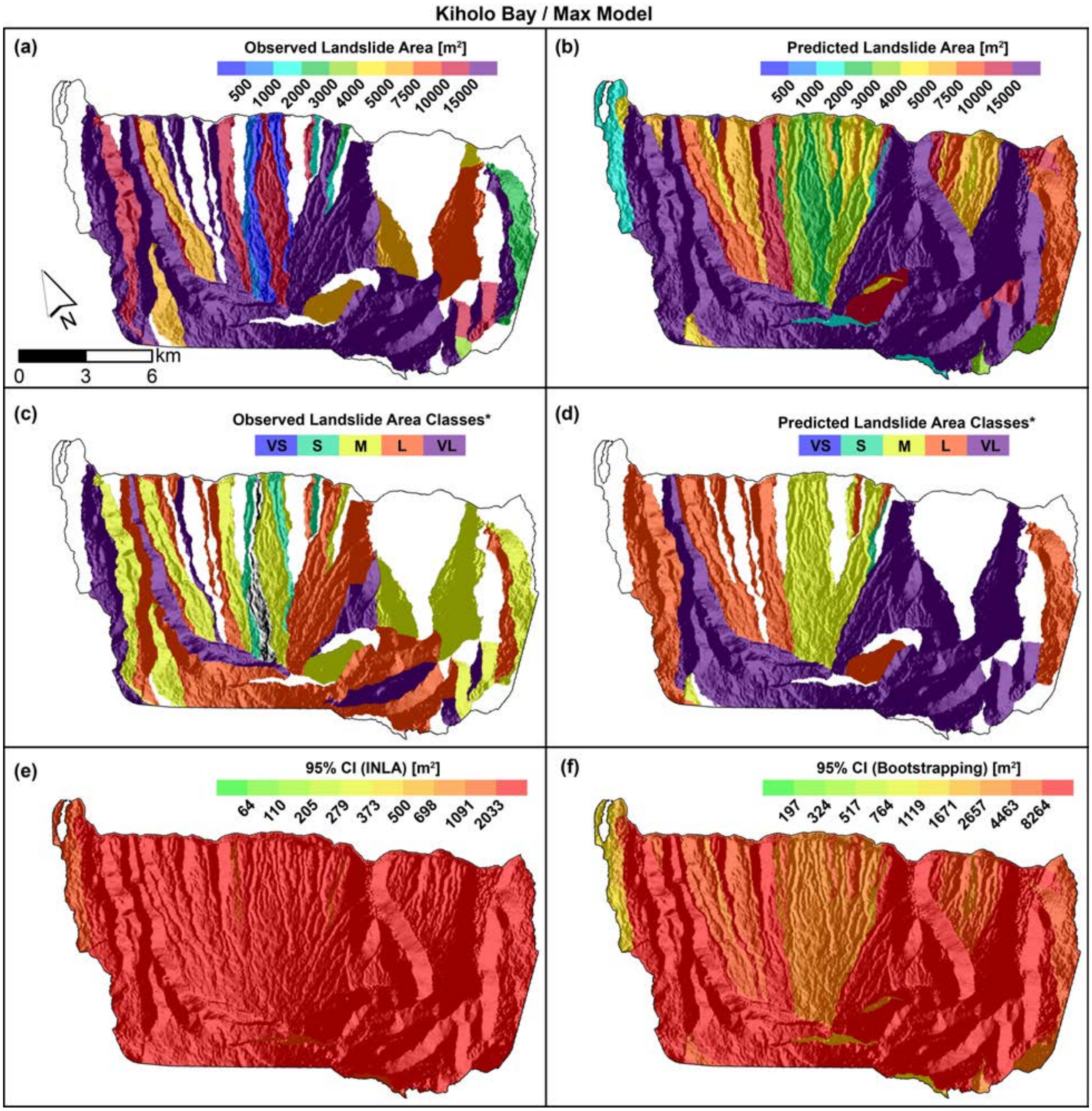

Figure SM15: Kiholo Bay max maps: (a) Observed maximum landslide area per SU. (b) Predicted maximum landslide area per SU. (c) Classified observed maximum landslide area per SU. (d) Classified predicted maximum landslide area per SU. (d) 95% credible interval estimated with INLA. (e) 95% credible interval estimated via bootstrap.

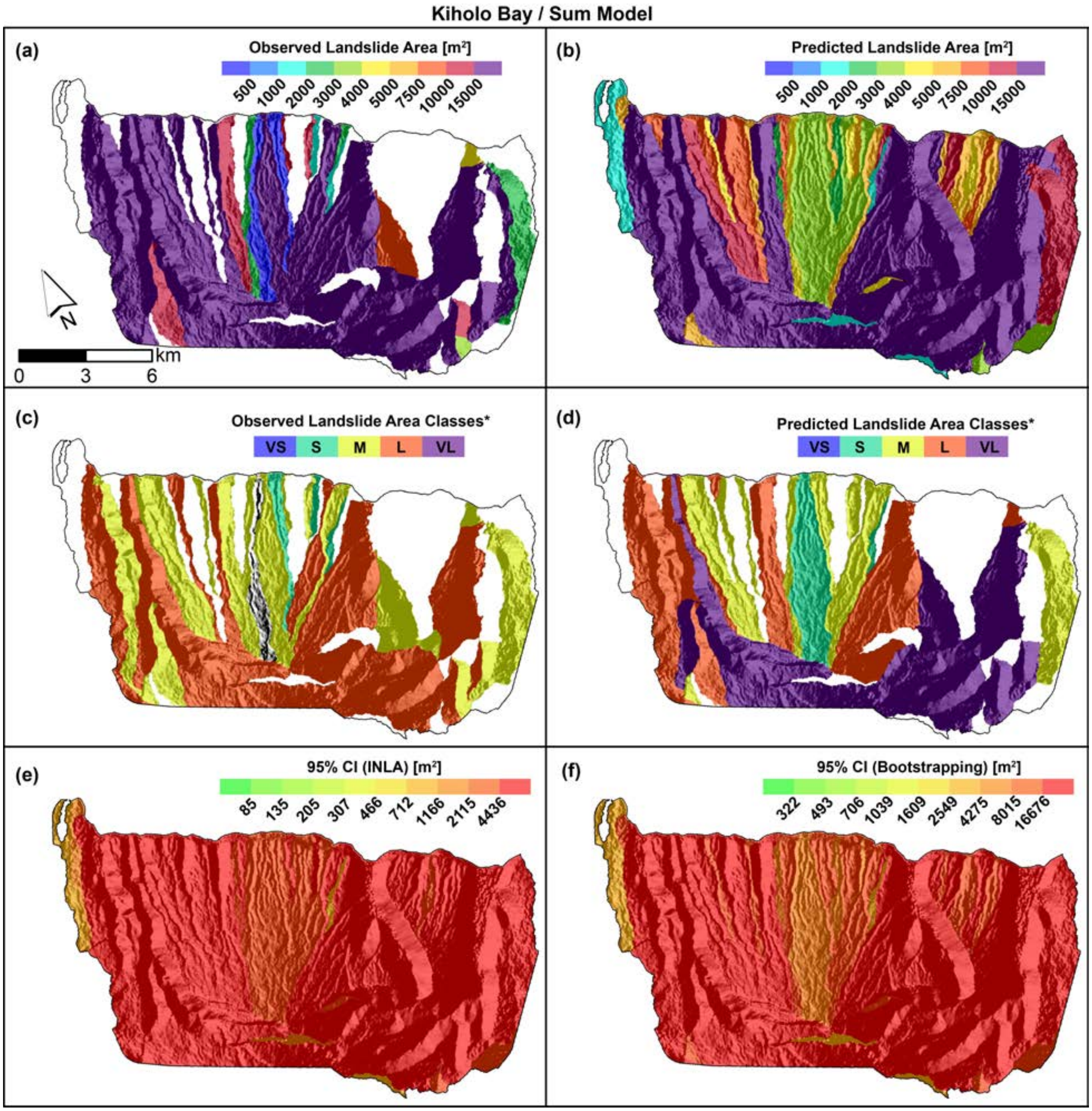

Figure SM16: Kiholo Bay sum maps: (a) Observed maximum landslide area per SU. (b) Predicted maximum landslide area per SU. (c) Classified observed maximum landslide area per SU. (d) Classified predicted maximum landslide area per SU. (d) 95% credible interval estimated with INLA. (e) 95% credible interval estimated via bootstrap.

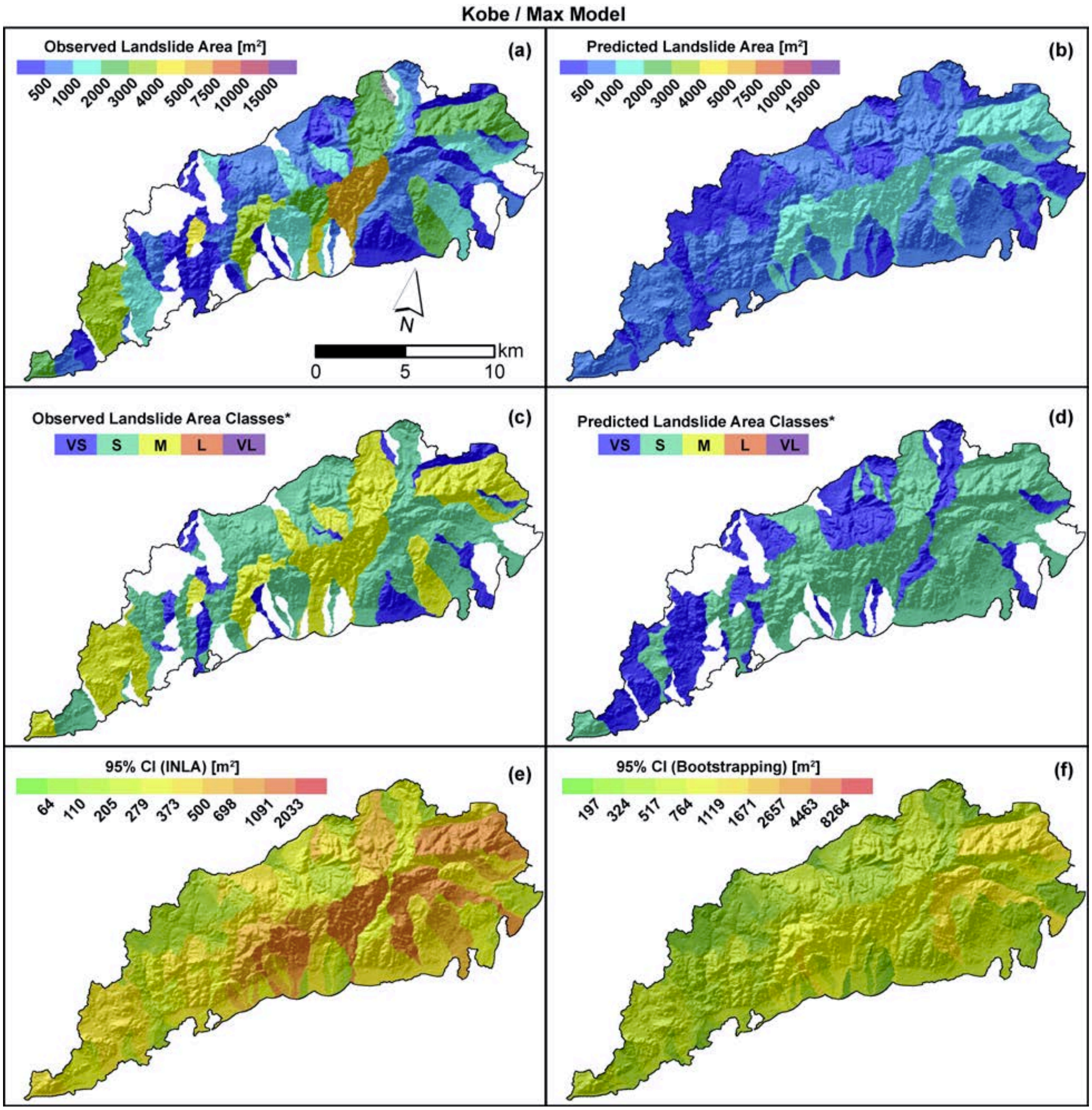

Figure SM17: Kobe max maps: (a) Observed maximum landslide area per SU. (b) Predicted maximum landslide area per SU. (c) Classified observed maximum landslide area per SU. (d) Classified predicted maximum landslide area per SU. (d) 95% credible interval estimated with INLA. (e) 95% credible interval estimated via bootstrap.

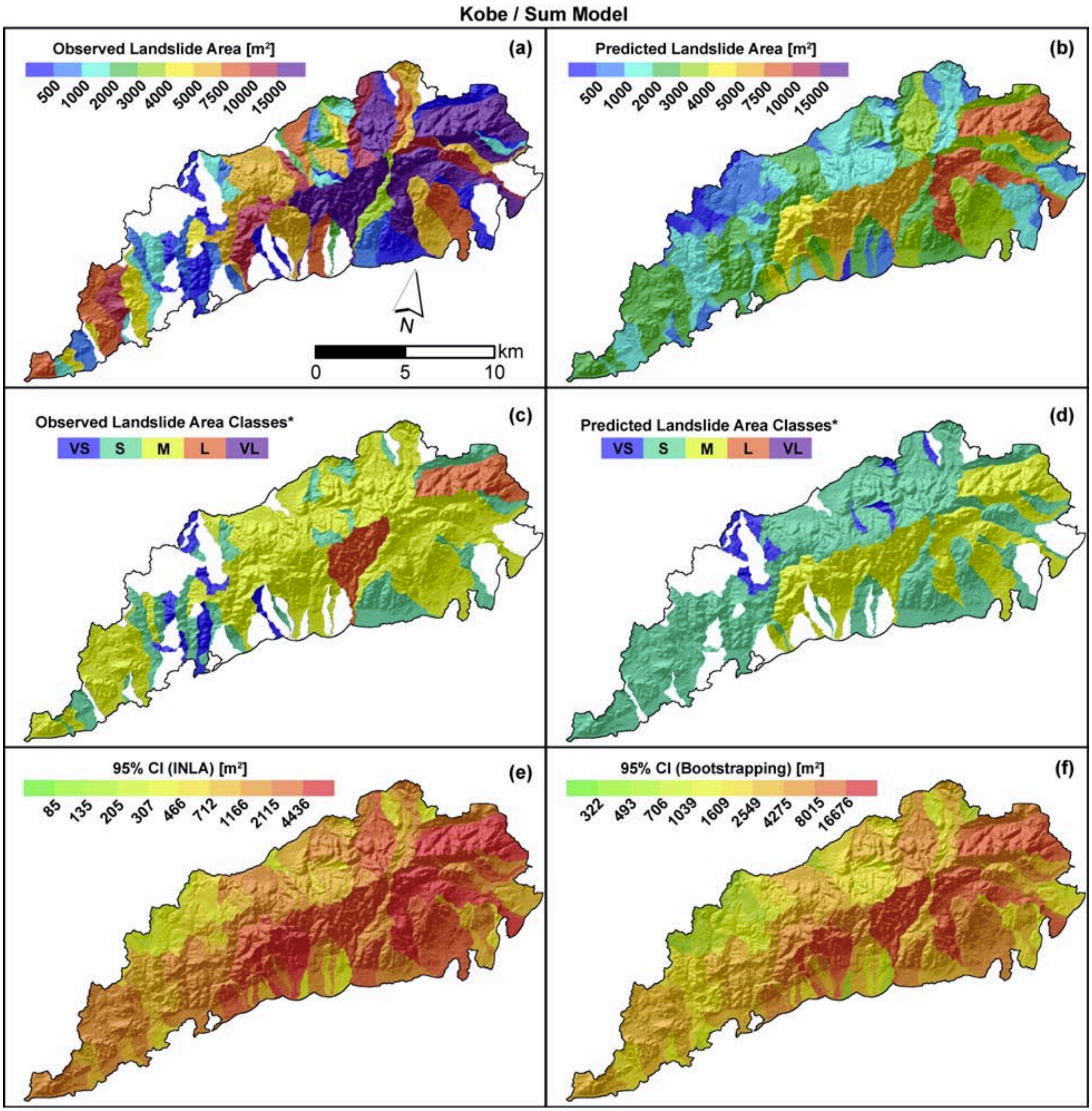

Figure SM18: Kobe sum maps: (a) Observed maximum landslide area per SU. (b) Predicted maximum landslide area per SU. (c) Classified observed maximum landslide area per SU. (d) Classified predicted maximum landslide area per SU. (d) 95% credible interval estimated with INLA. (e) 95% credible interval estimated via bootstrap.

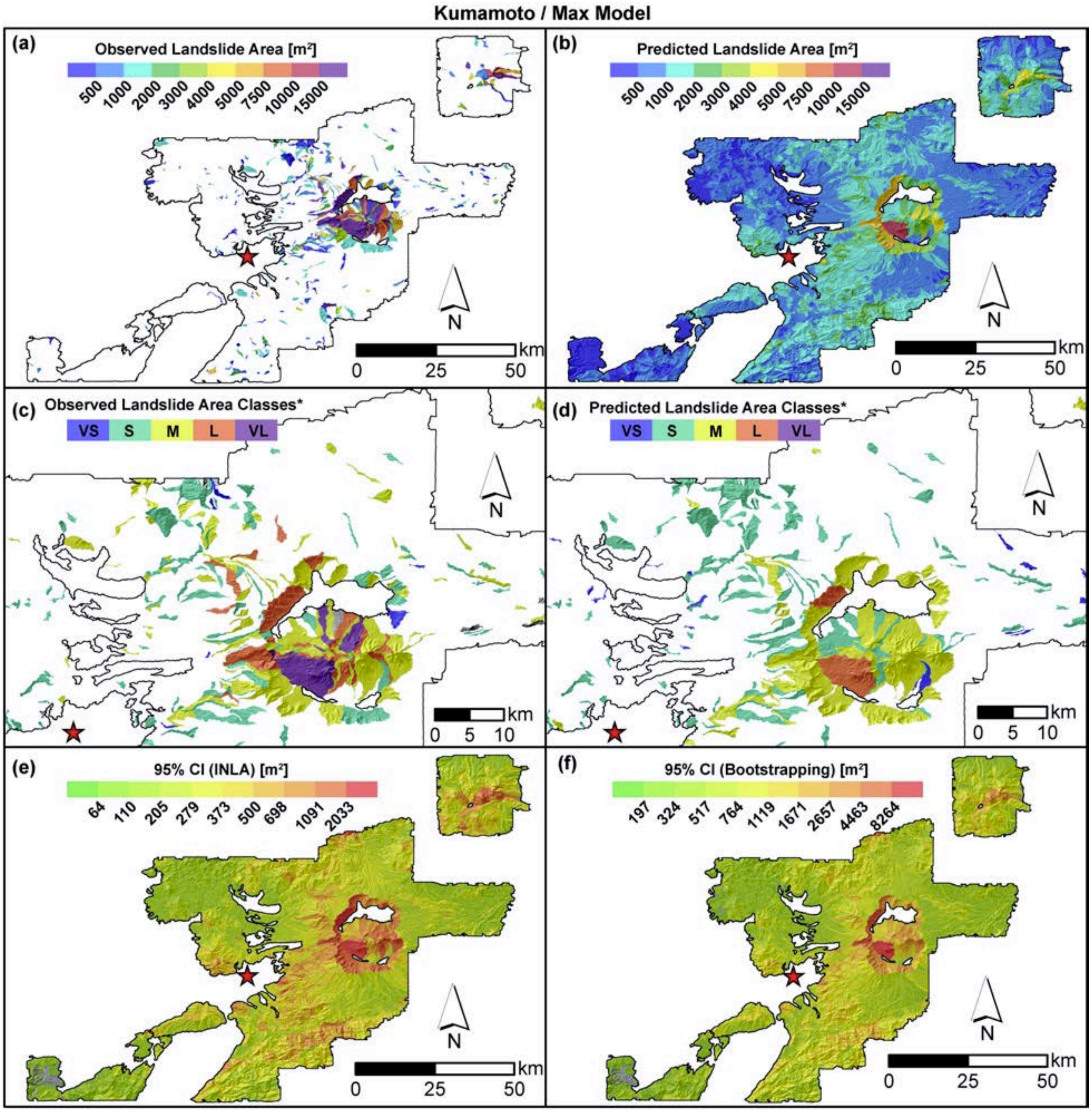

Figure SM19: Kumamoto max maps: (a) Observed maximum landslide area per SU. (b) Predicted maximum landslide area per SU. (c) Classified observed maximum landslide area per SU. (d) Classified predicted maximum landslide area per SU. (d) 95% credible interval estimated with INLA. (e) 95% credible interval estimated via bootstrap.

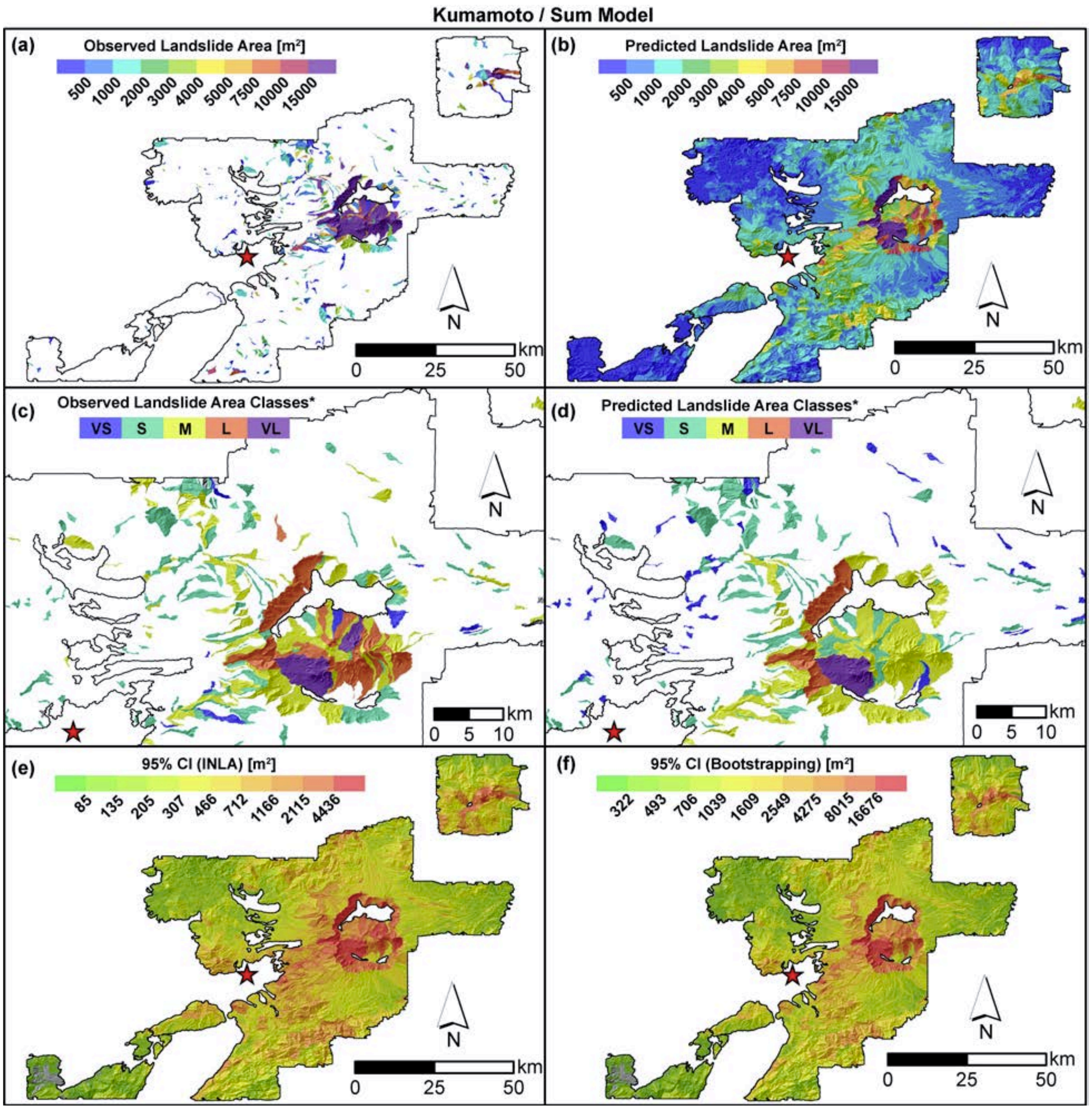

Figure SM20: Kumamoto sum maps: (a) Observed maximum landslide area per SU. (b) Predicted maximum landslide area per SU. (c) Classified observed maximum landslide area per SU. (d) Classified predicted maximum landslide area per SU. (d) 95% credible interval estimated with INLA. (e) 95% credible interval estimated via bootstrap.

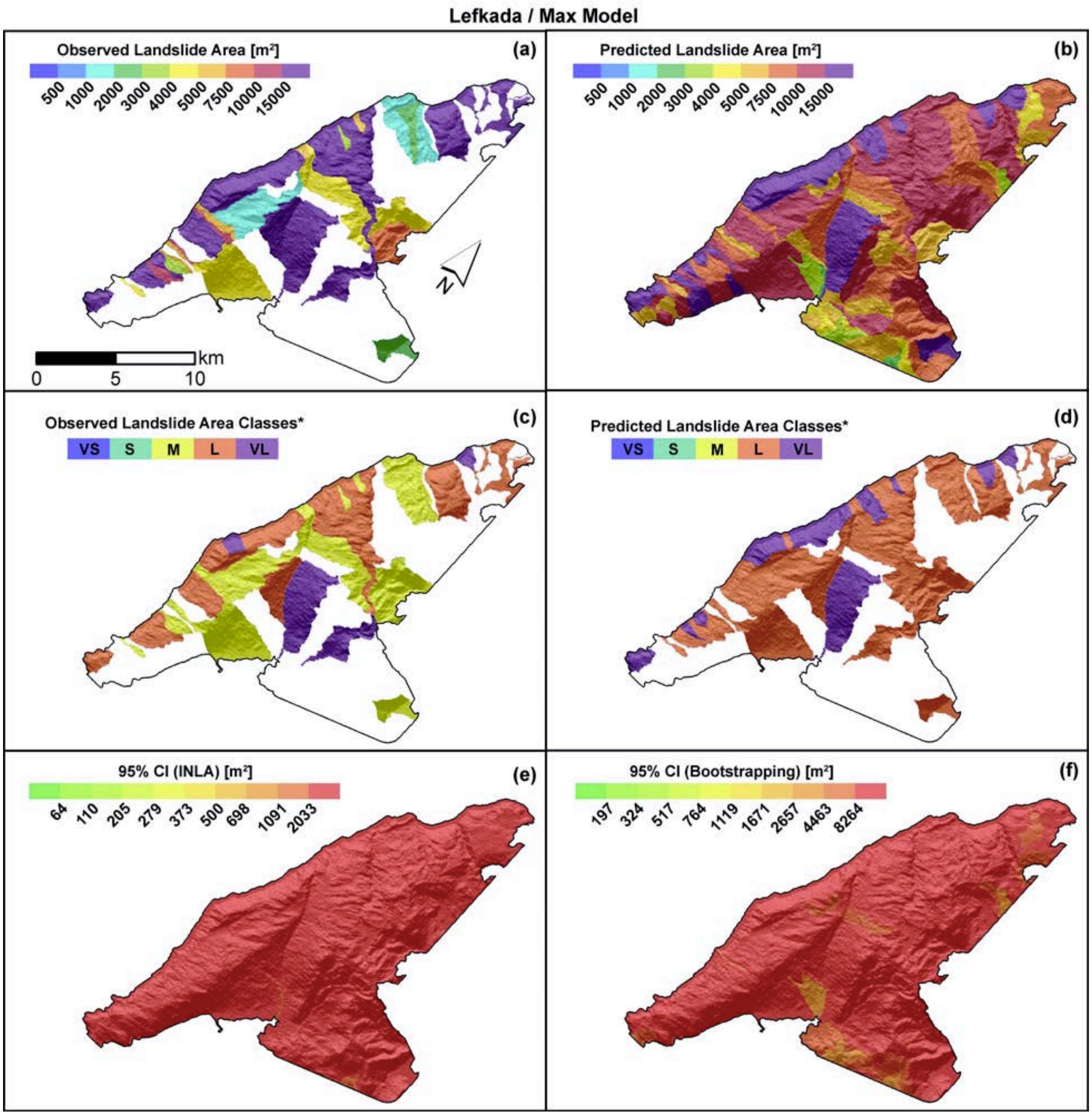

Figure SM21: Lefkada max maps: (a) Observed maximum landslide area per SU. (b) Predicted maximum landslide area per SU. (c) Classified observed maximum landslide area per SU. (d) Classified predicted maximum landslide area per SU. (d) 95% credible interval estimated with INLA. (e) 95% credible interval estimated via bootstrap.

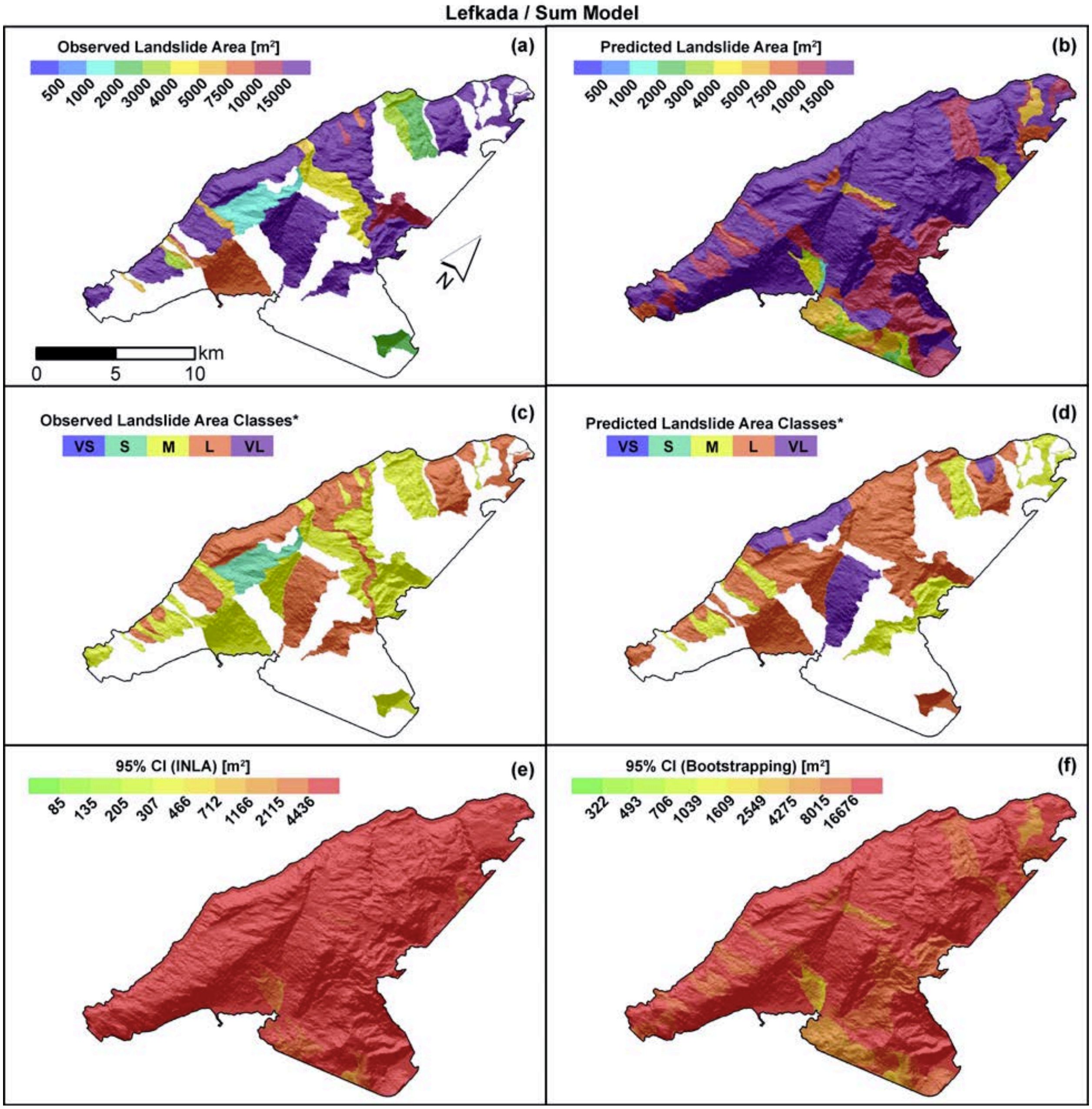

Figure SM22: Lefkada sum maps: (a) Observed maximum landslide area per SU. (b) Predicted maximum landslide area per SU. (c) Classified observed maximum landslide area per SU. (d) Classified predicted maximum landslide area per SU. (d) 95% credible interval estimated with INLA. (e) 95% credible interval estimated via bootstrap.

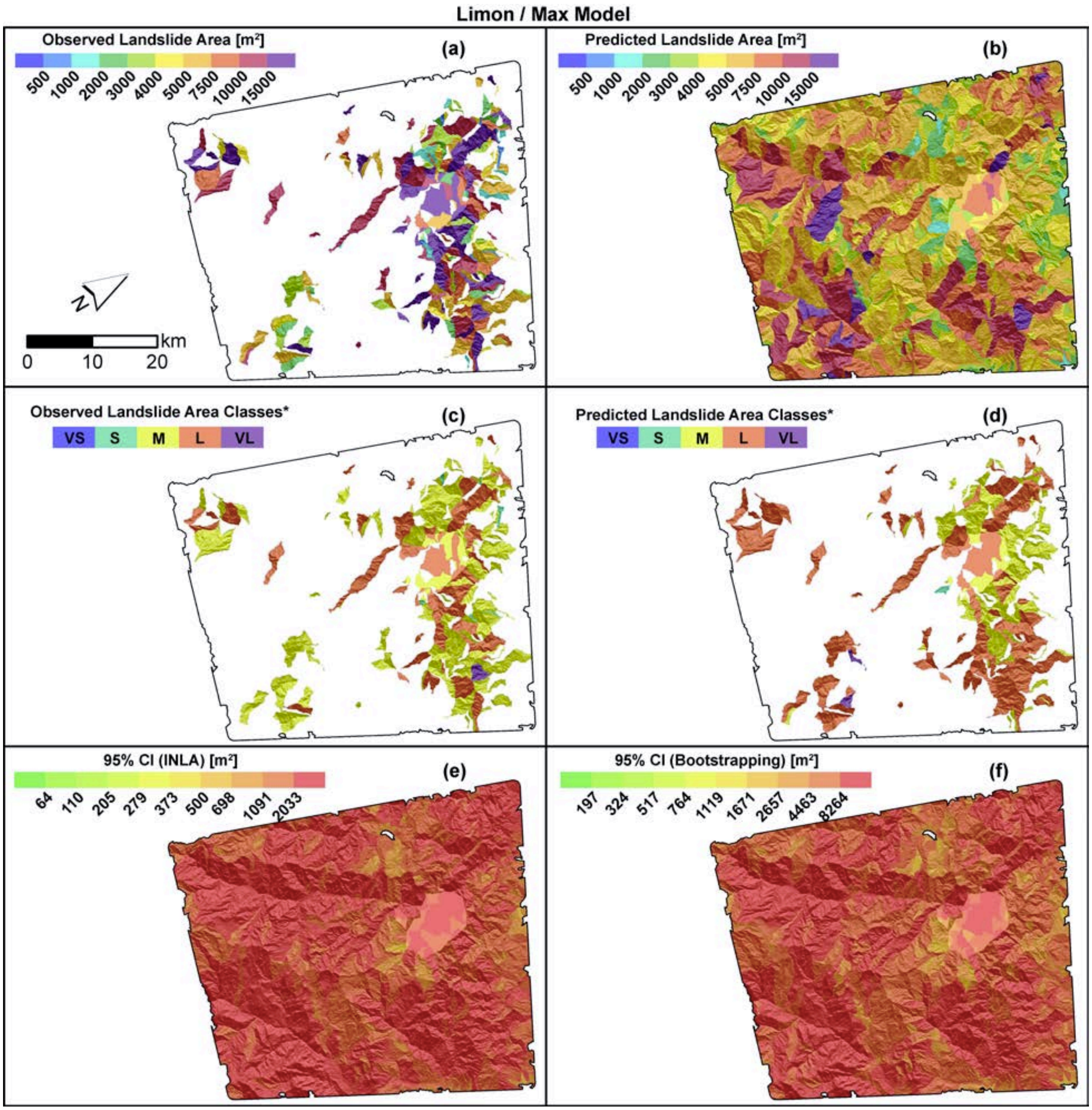

Figure SM23: Limon max maps: (a) Observed maximum landslide area per SU. (b) Predicted maximum landslide area per SU. (c) Classified observed maximum landslide area per SU. (d) Classified predicted maximum landslide area per SU. (d) 95% credible interval estimated with INLA. (e) 95% credible interval estimated via bootstrap.

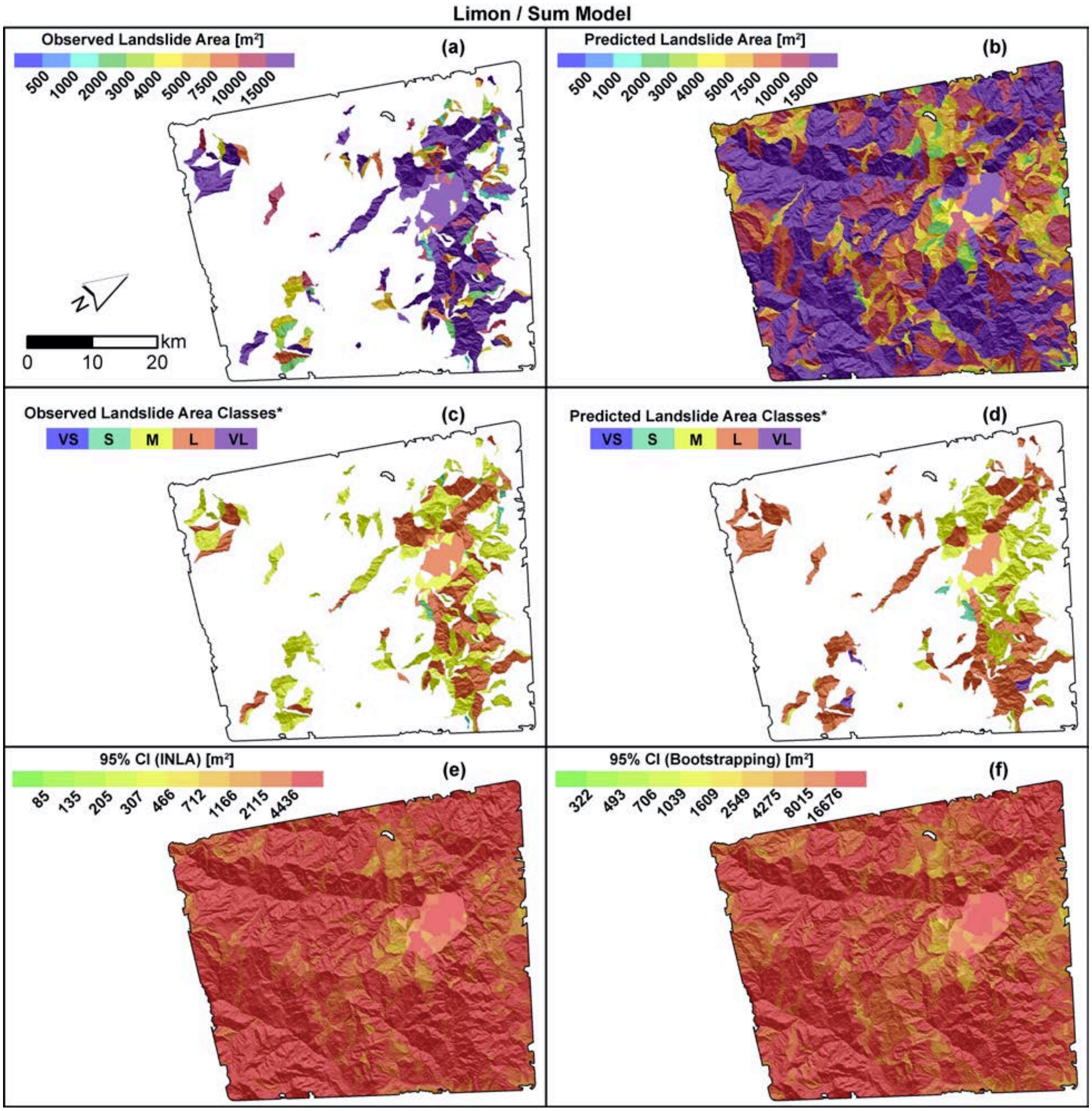

Figure SM24: Limon sum maps: (a) Observed maximum landslide area per SU. (b) Predicted maximum landslide area per SU. (c) Classified observed maximum landslide area per SU. (d) Classified predicted maximum landslide area per SU. (d) 95% credible interval estimated with INLA. (e) 95% credible interval estimated via bootstrap.

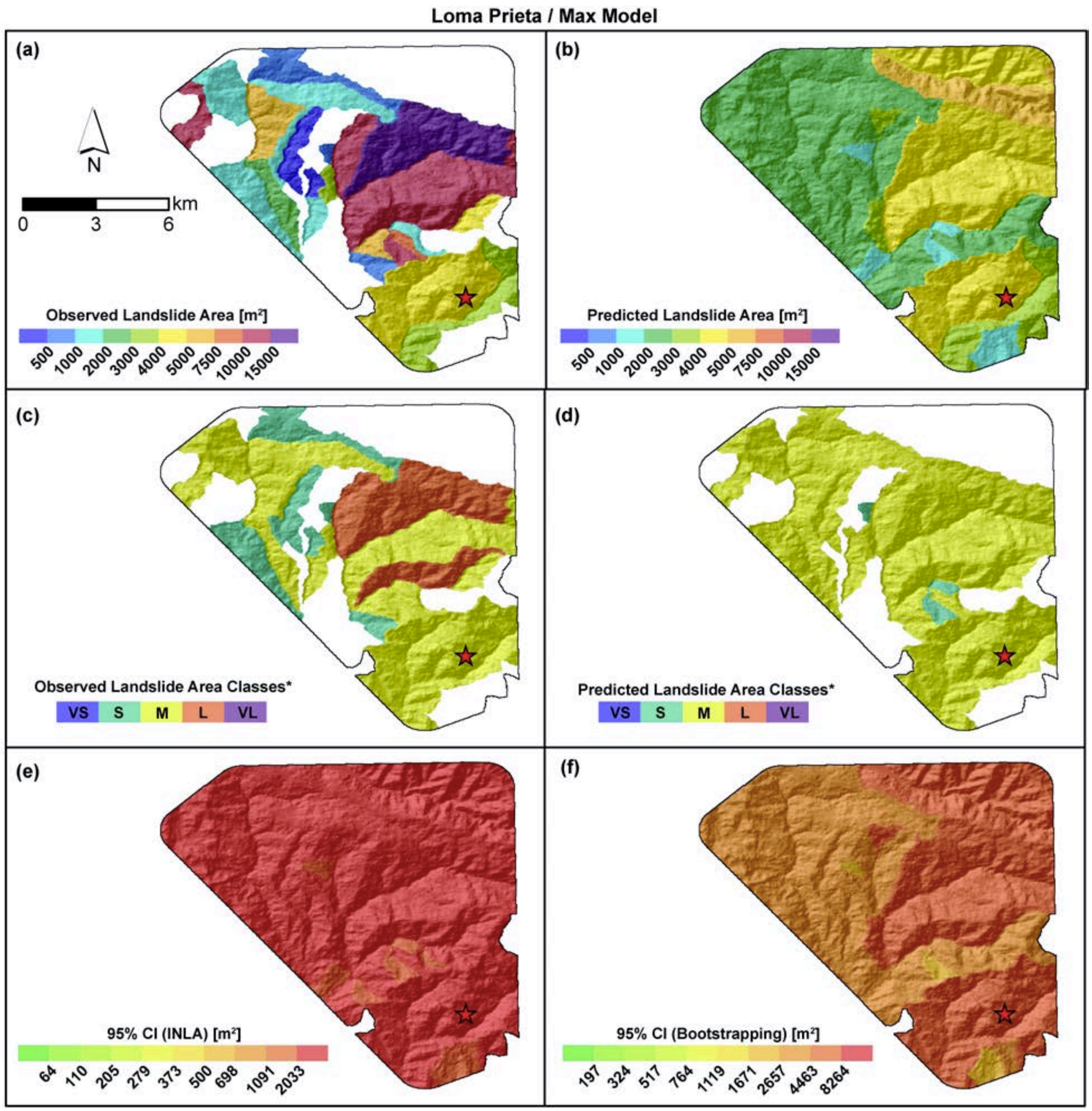

Figure SM25: Loma Prieta max maps: (a) Observed maximum landslide area per SU. (b) Predicted maximum landslide area per SU. (c) Classified observed maximum landslide area per SU. (d) Classified predicted maximum landslide area per SU. (d) 95% credible interval estimated with INLA. (e) 95% credible interval estimated via bootstrap.

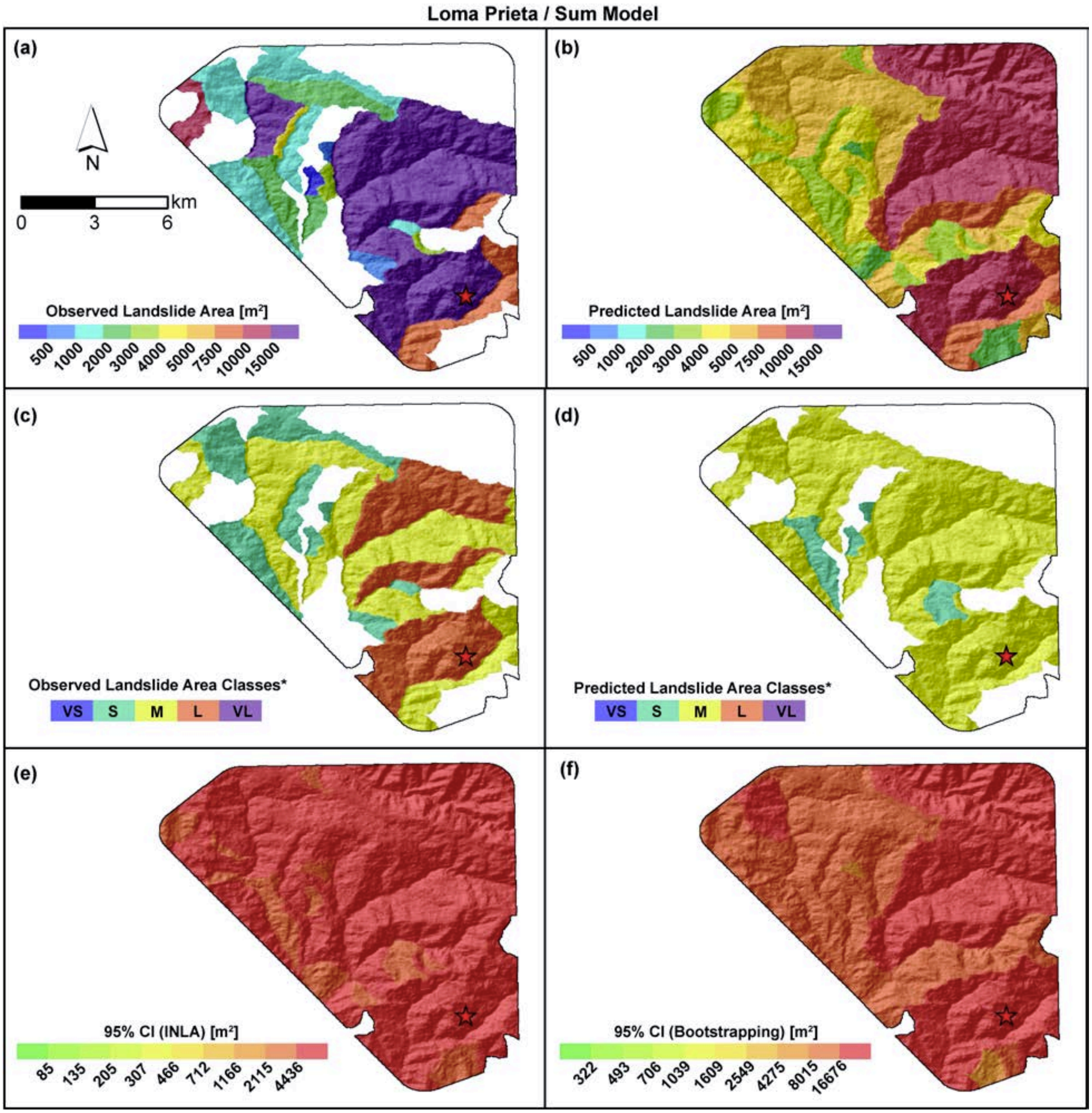

Figure SM26: Loma Prieta sum maps: (a) Observed maximum landslide area per SU. (b) Predicted maximum landslide area per SU. (c) Classified observed maximum landslide area per SU. (d) Classified predicted maximum landslide area per SU. (d) 95% credible interval estimated with INLA. (e) 95% credible interval estimated via bootstrap.

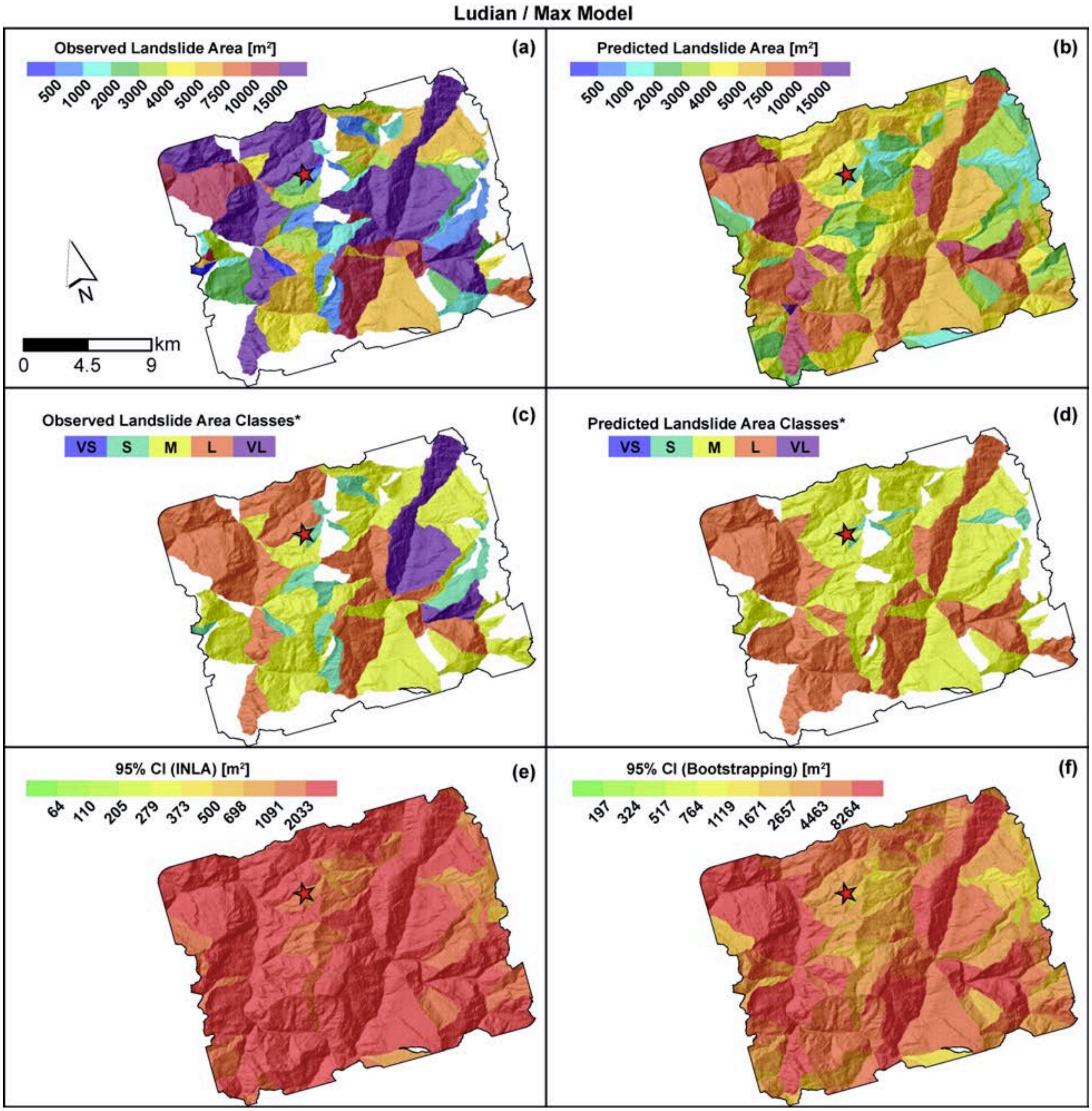

Figure SM27: Ludian max maps: (a) Observed maximum landslide area per SU. (b) Predicted maximum landslide area per SU. (c) Classified observed maximum landslide area per SU. (d) Classified predicted maximum landslide area per SU. (d) 95% credible interval estimated with INLA. (e) 95% credible interval estimated via bootstrap.

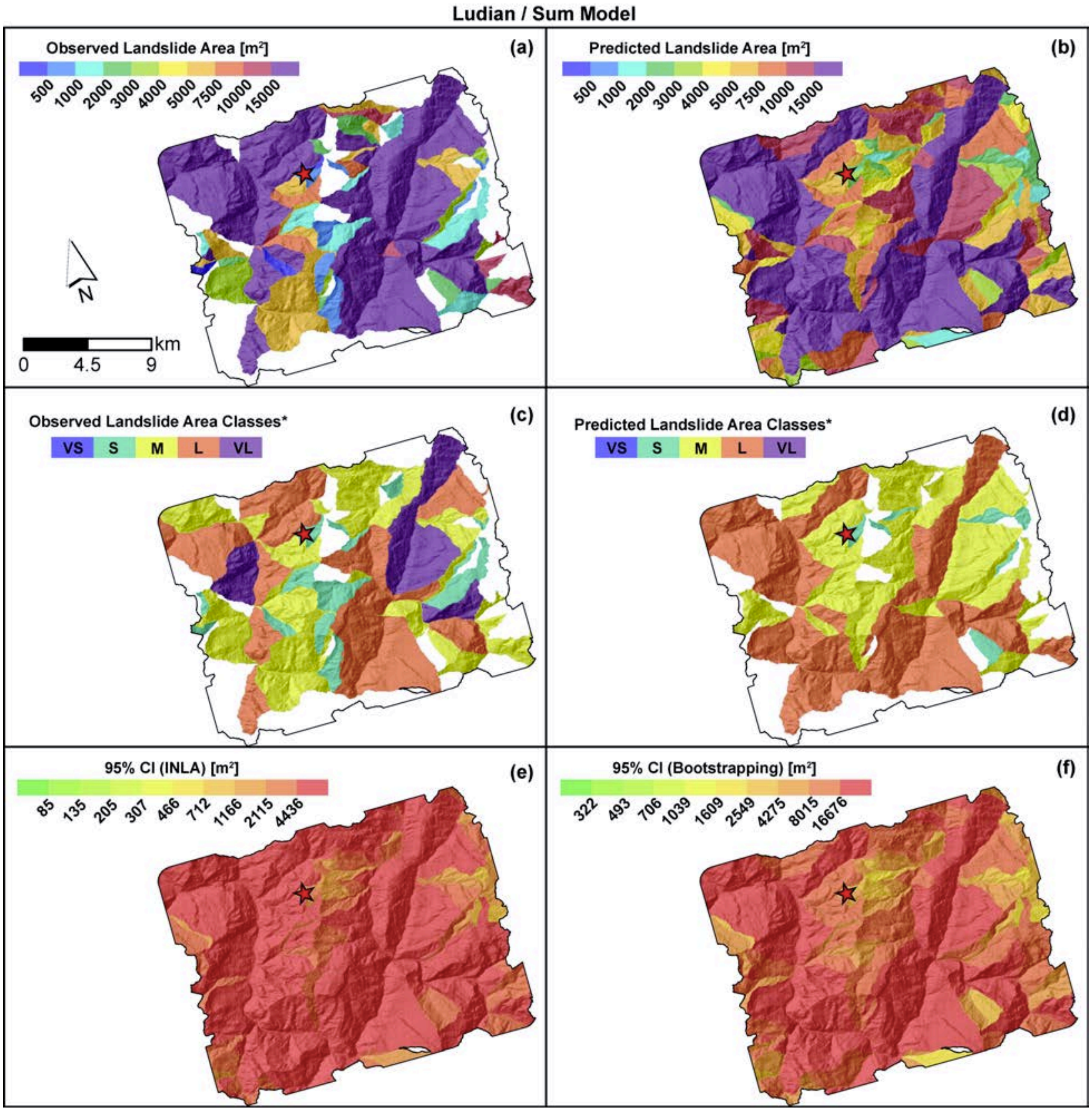

Figure SM28: Ludian sum maps: (a) Observed maximum landslide area per SU. (b) Predicted maximum landslide area per SU. (c) Classified observed maximum landslide area per SU. (d) Classified predicted maximum landslide area per SU. (d) 95% credible interval estimated with INLA. (e) 95% credible interval estimated via bootstrap.

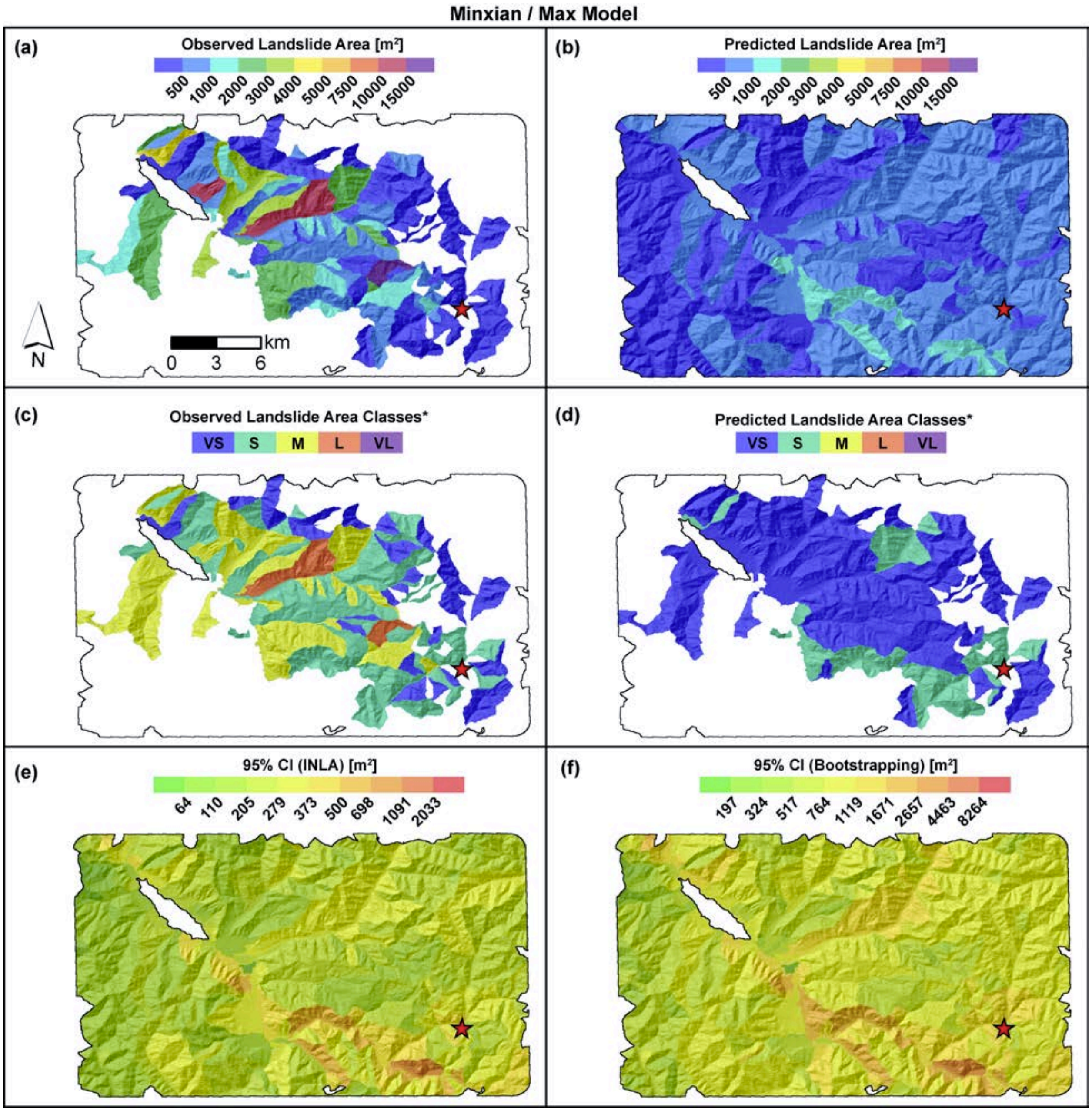

Figure SM 29: Minxian max maps: (a) Observed maximum landslide area per SU. (b) Predicted maximum landslide area per SU. (c) Classified observed maximum landslide area per SU. (d) Classified predicted maximum landslide area per SU. (d) 95% credible interval estimated with INLA. (e) 95% credible interval estimated via bootstrap.

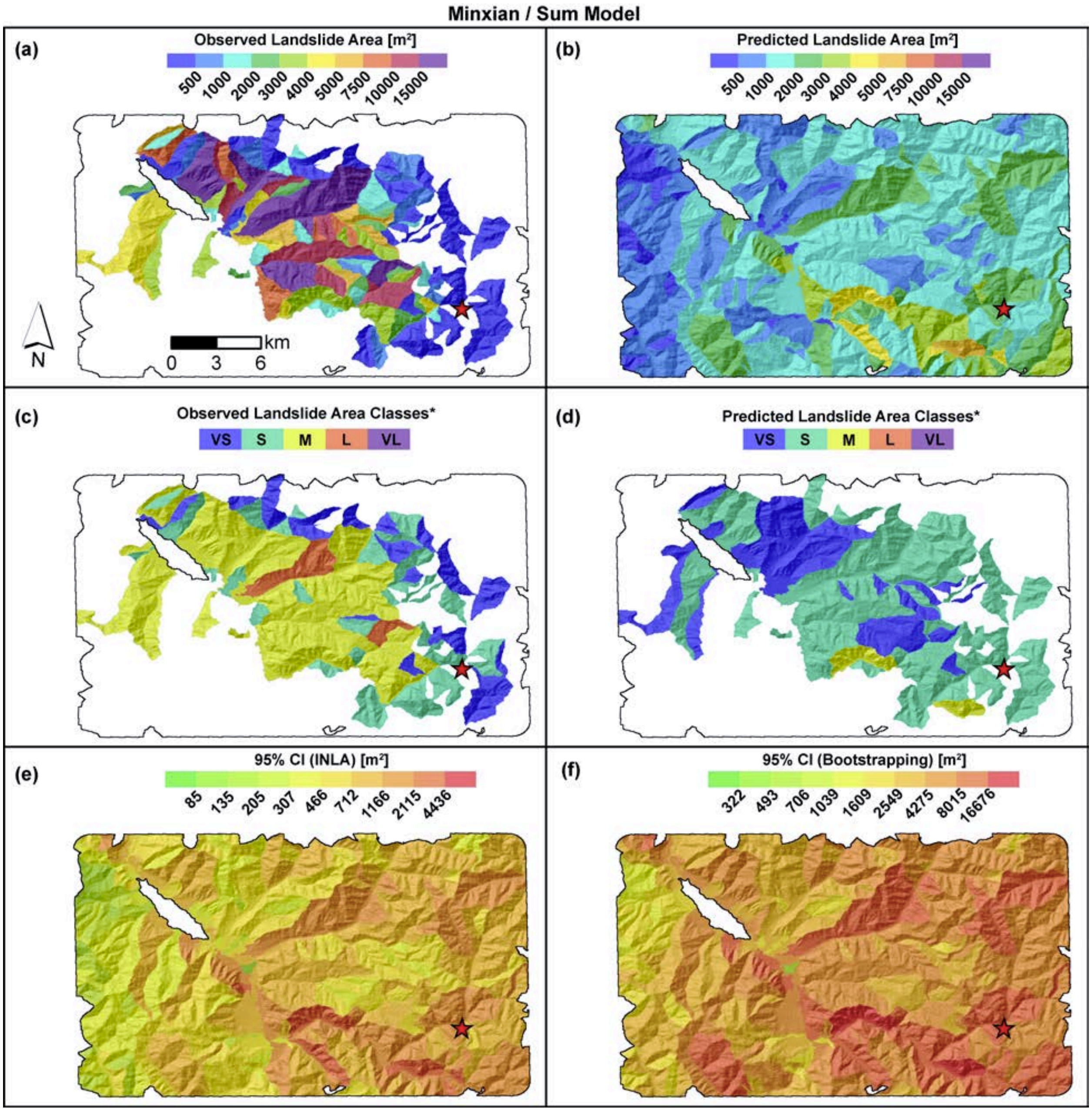

Figure SM30: Minxian sum maps: (a) Observed maximum landslide area per SU. (b) Predicted maximum landslide area per SU. (c) Classified observed maximum landslide area per SU. (d) Classified predicted maximum landslide area per SU. (d) 95% credible interval estimated with INLA. (e) 95% credible interval estimated via bootstrap.

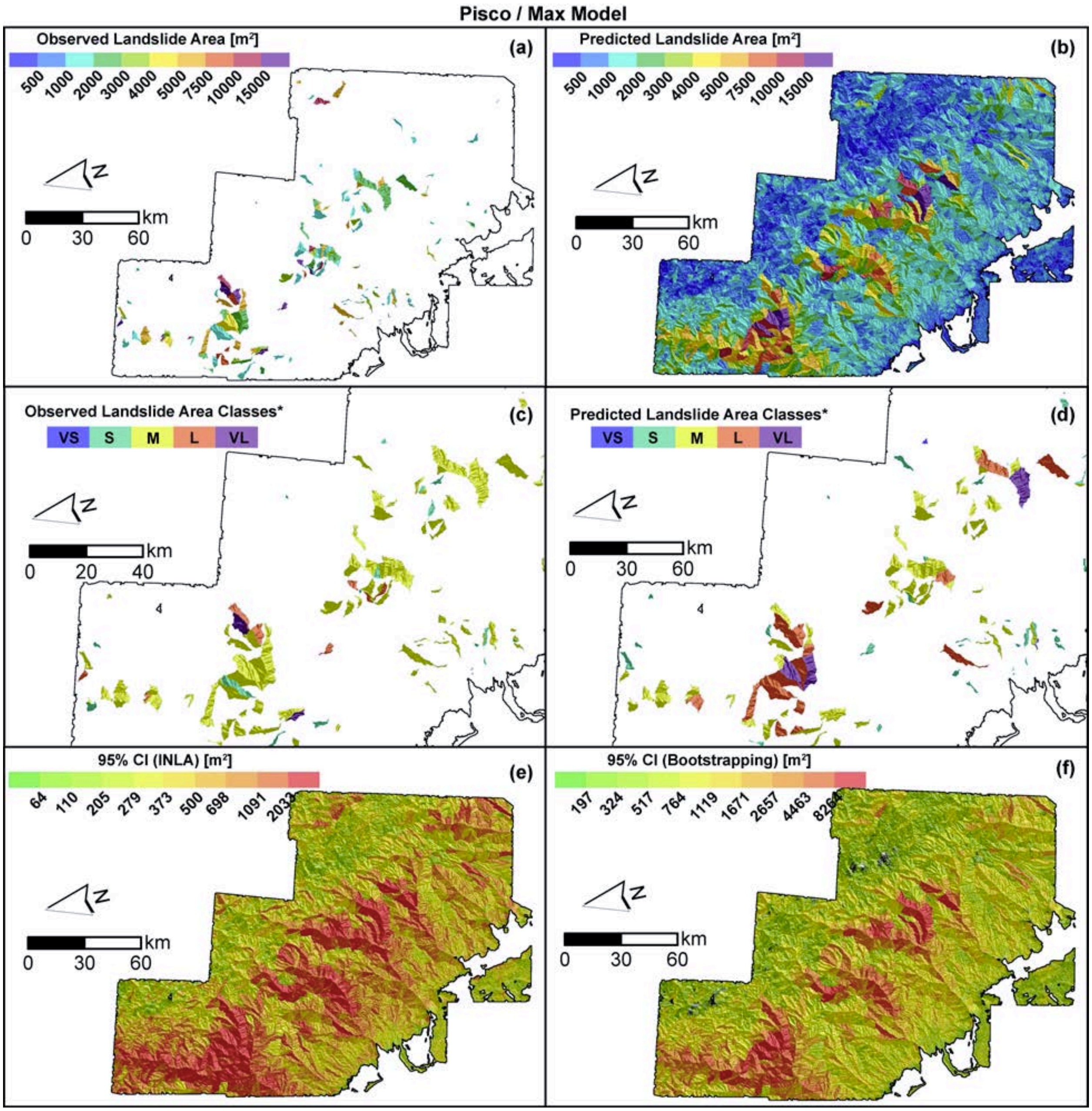

Figure SM31: Pisco max maps: (a) Observed maximum landslide area per SU. (b) Predicted maximum landslide area per SU. (c) Classified observed maximum landslide area per SU. (d) Classified predicted maximum landslide area per SU. (d) 95% credible interval estimated with INLA. (e) 95% credible interval estimated via bootstrap.

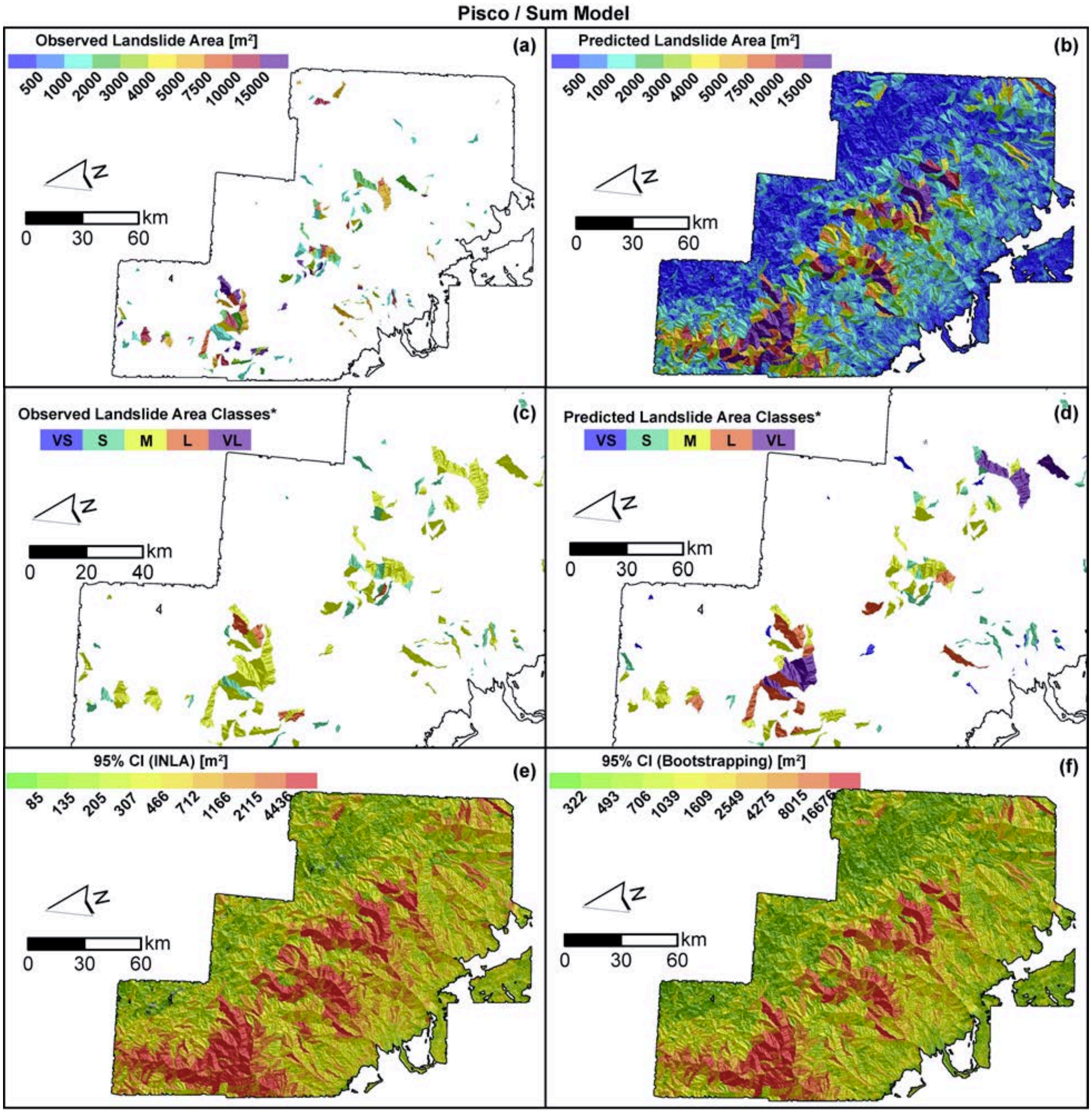

Figure SM32: Pisco sum maps: (a) Observed maximum landslide area per SU. (b) Predicted maximum landslide area per SU. (c) Classified observed maximum landslide area per SU. (d) Classified predicted maximum landslide area per SU. (d) 95% credible interval estimated with INLA. (e) 95% credible interval estimated via bootstrap.

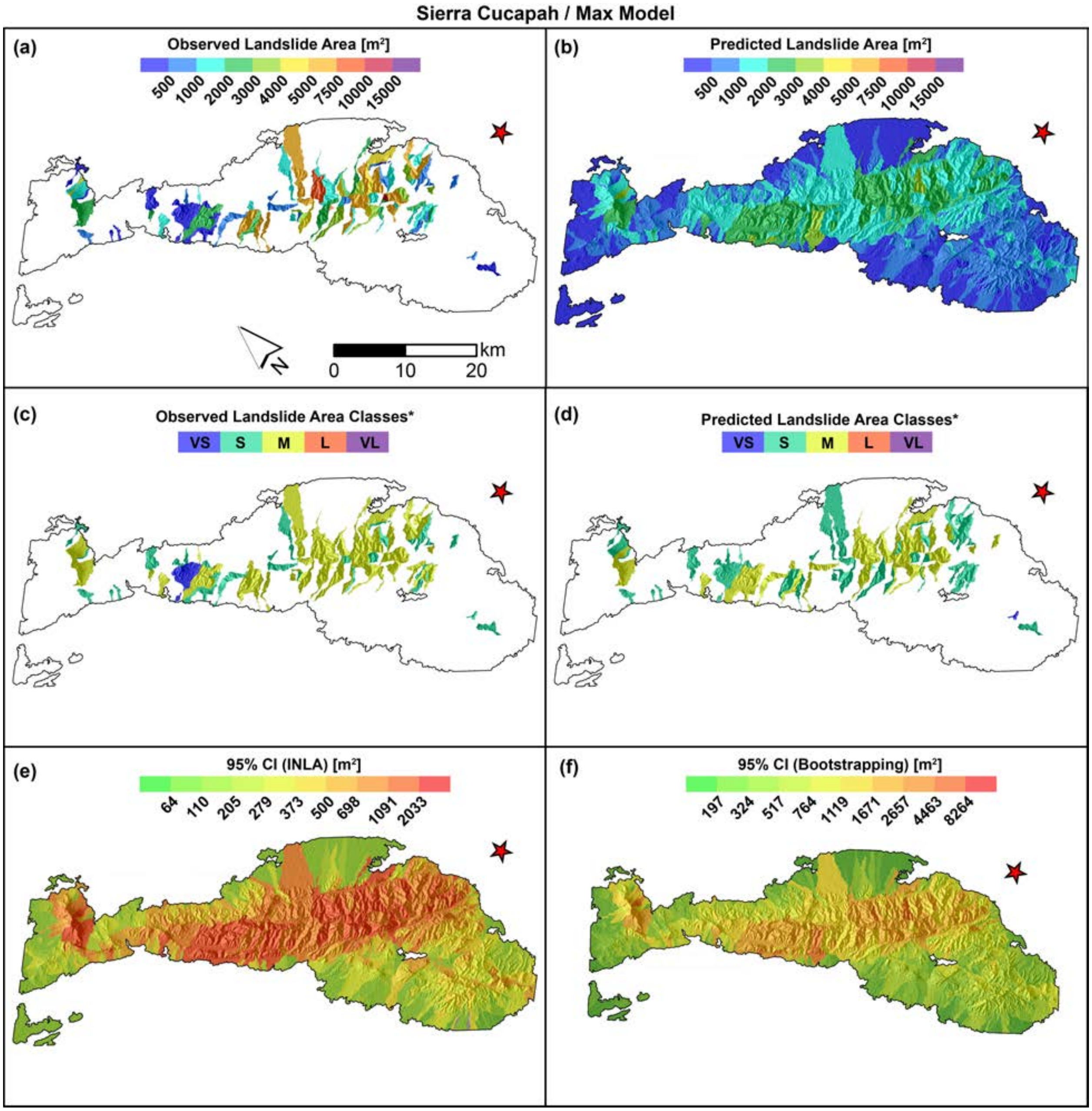

Figure SM33: Sierra Cucapah max maps: (a) Observed maximum landslide area per SU. (b) Predicted maximum landslide area per SU. (c) Classified observed maximum landslide area per SU. (d) Classified predicted maximum landslide area per SU. (d) 95% credible interval estimated with INLA. (e) 95% credible interval estimated via bootstrap.

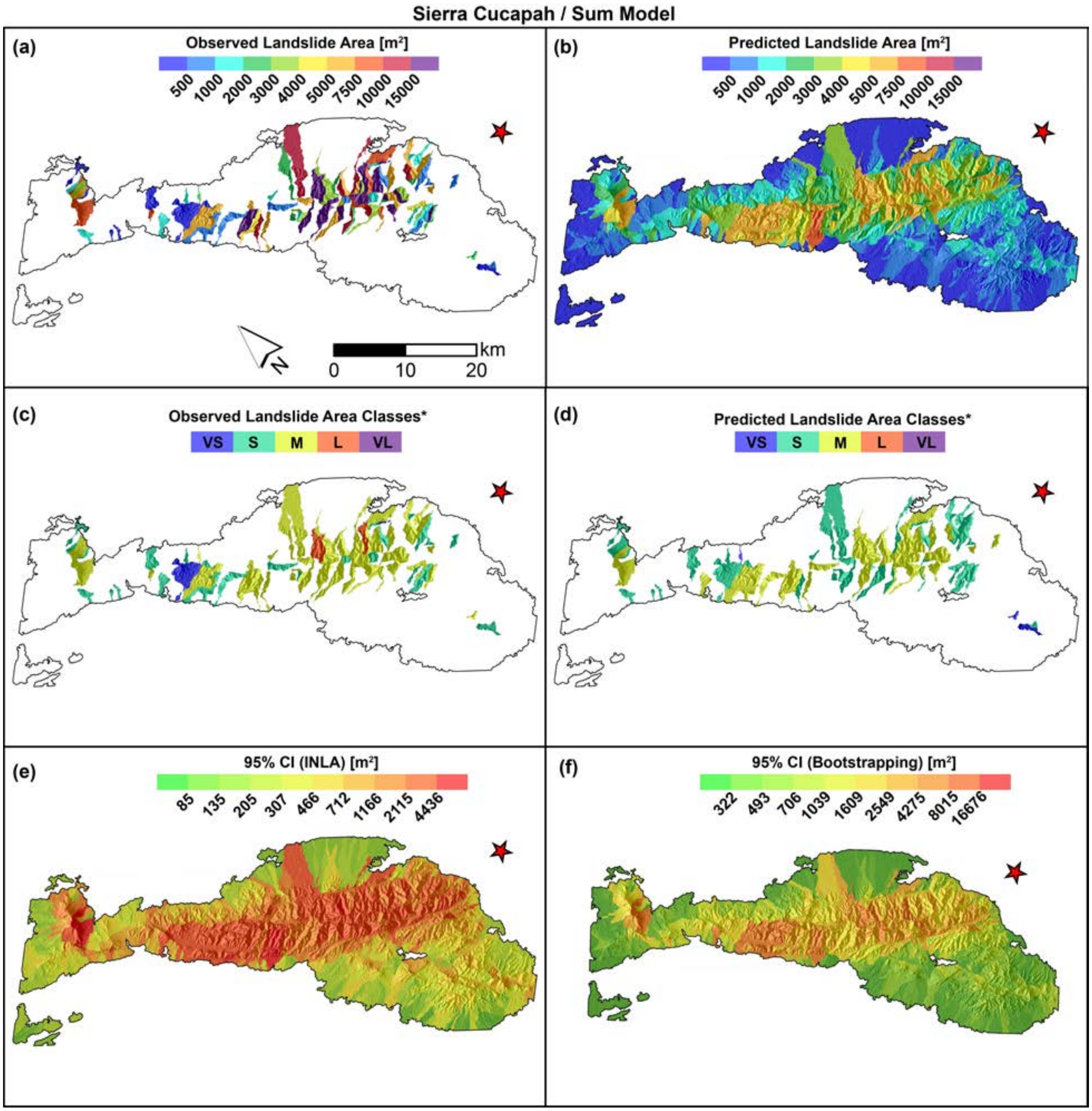

Figure SM34: Sierra Cucapah sum maps: (a) Observed maximum landslide area per SU. (b) Predicted maximum landslide area per SU. (c) Classified observed maximum landslide area per SU. (d) Classified predicted maximum landslide area per SU. (d) 95% credible interval estimated with INLA. (e) 95% credible interval estimated via bootstrap.

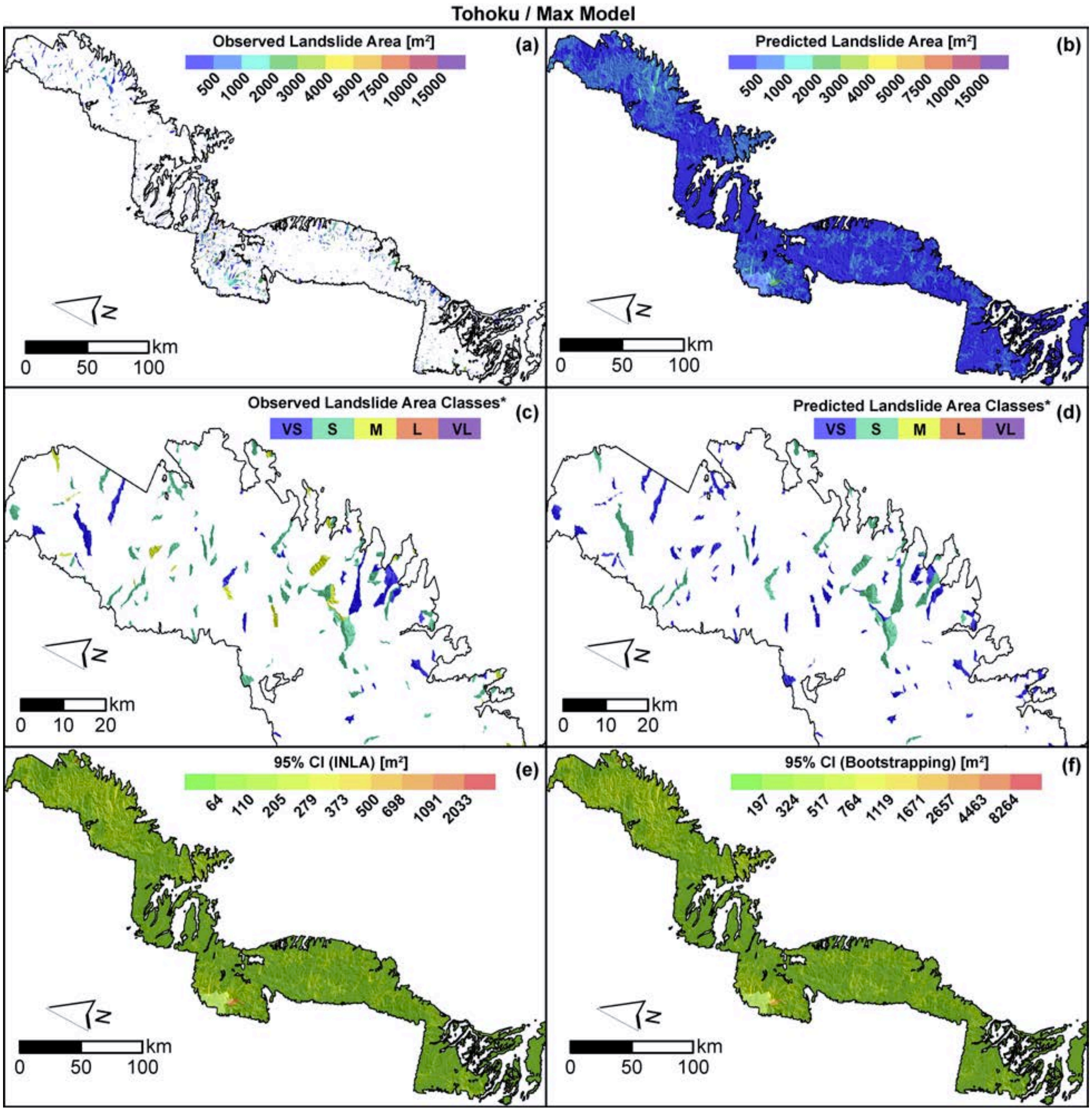

Figure SM35: Tohoku max maps: (a) Observed maximum landslide area per SU. (b) Predicted maximum landslide area per SU. (c) Classified observed maximum landslide area per SU. (d) Classified predicted maximum landslide area per SU. (d) 95% credible interval estimated with INLA. (e) 95% credible interval estimated via bootstrap.

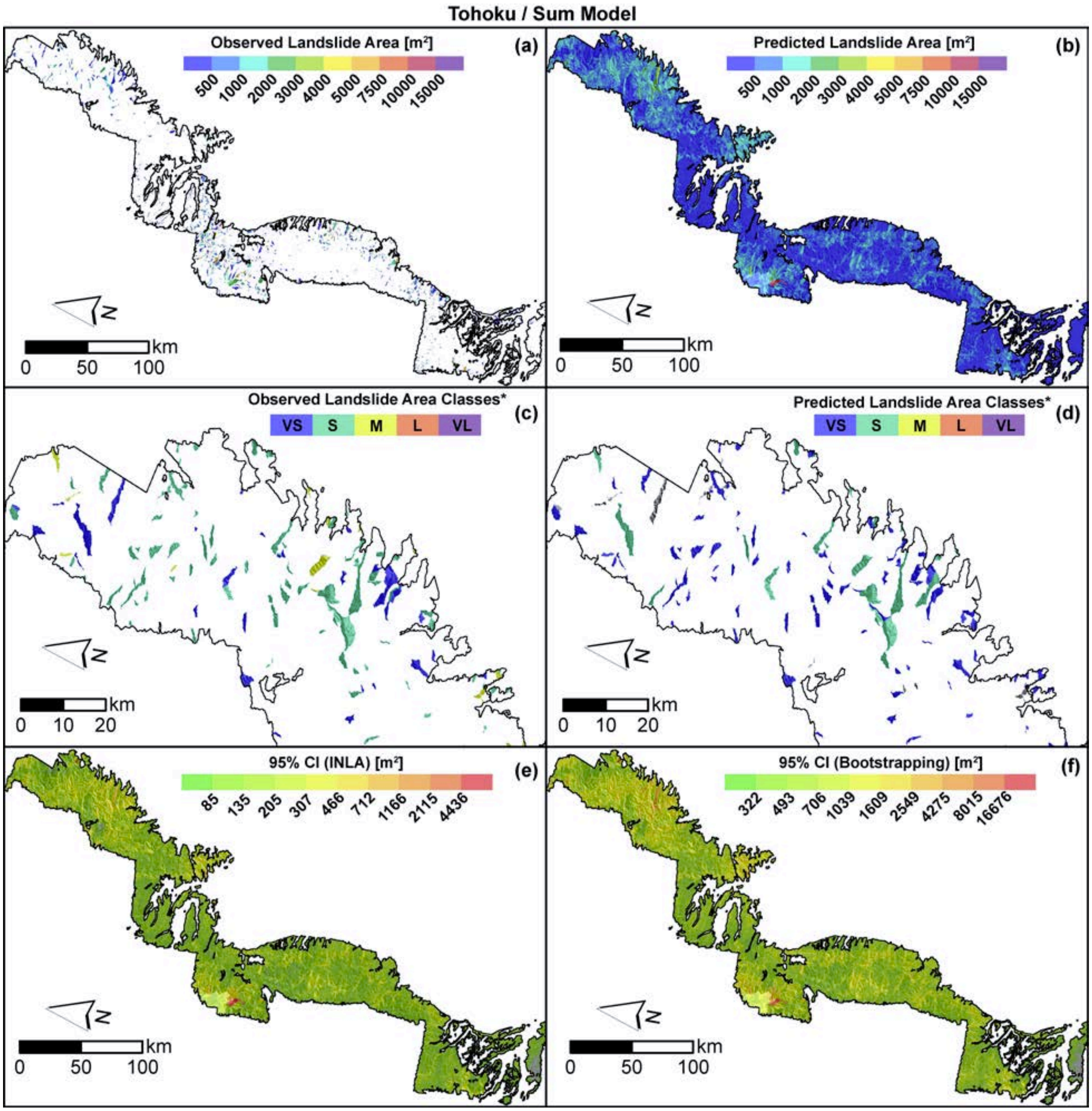

Figure SM36: Tohoku sum maps: (a) Observed maximum landslide area per SU. (b) Predicted maximum landslide area per SU. (c) Classified observed maximum landslide area per SU. (d) Classified predicted maximum landslide area per SU. (d) 95% credible interval estimated with INLA. (e) 95% credible interval estimated via bootstrap.

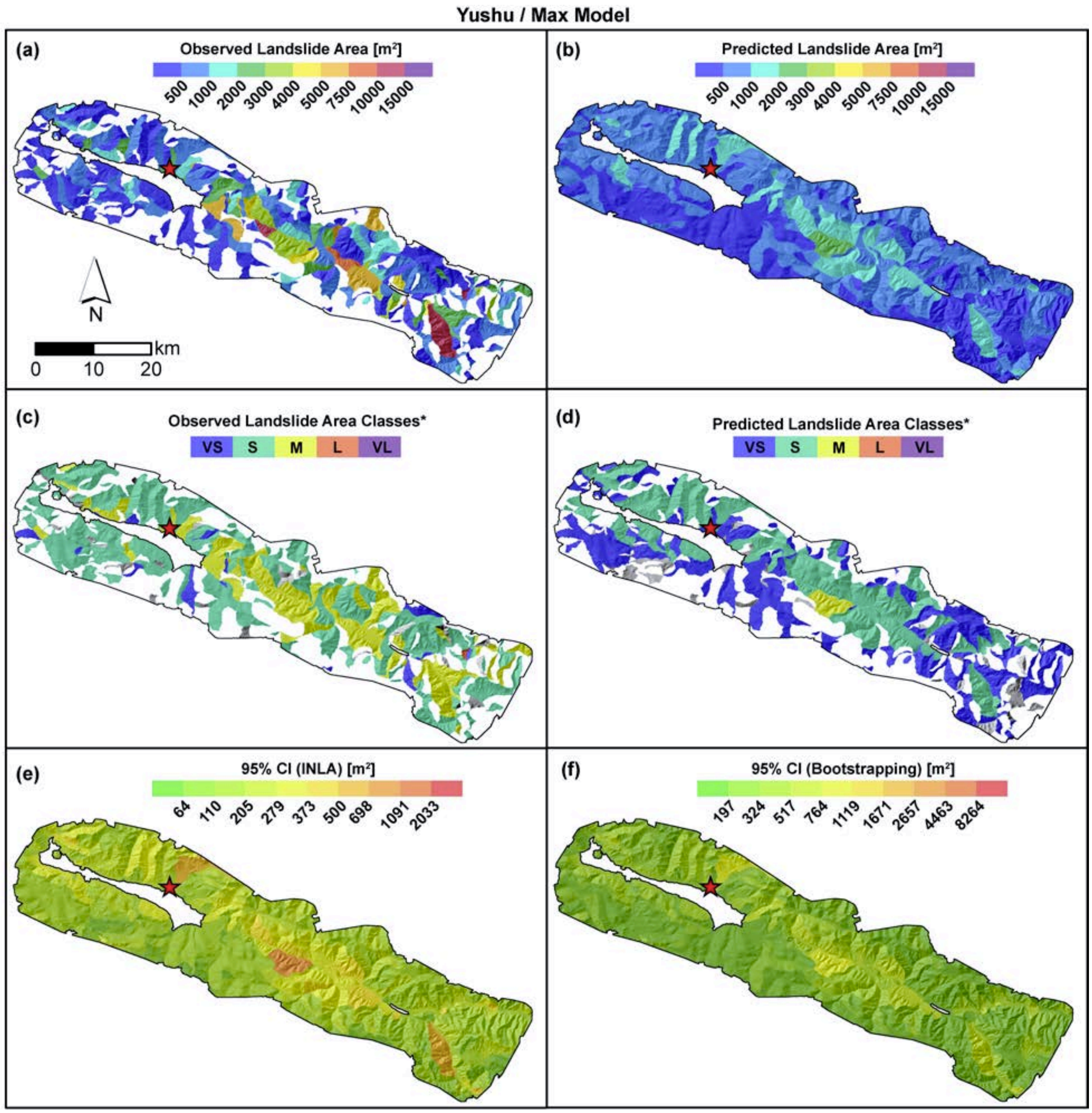

Figure SM37: Yushu max maps: (a) Observed maximum landslide area per SU. (b) Predicted maximum landslide area per SU. (c) Classified observed maximum landslide area per SU. (d) Classified predicted maximum landslide area per SU. (d) 95% credible interval estimated with INLA. (e) 95% credible interval estimated via bootstrap.

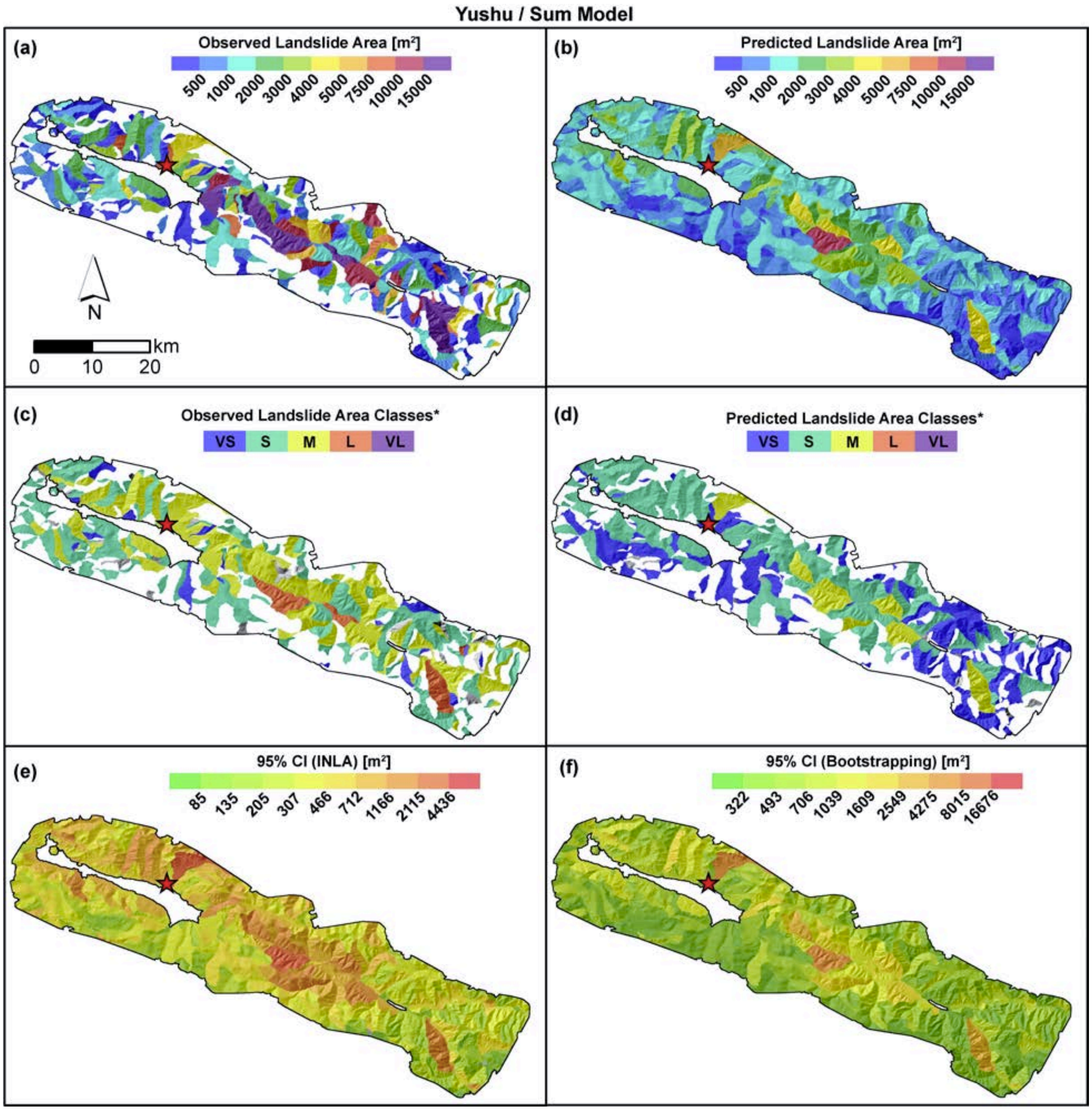

Figure SM38: Yushu sum maps: (a) Observed maximum landslide area per SU. (b) Predicted maximum landslide area per SU. (c) Classified observed maximum landslide area per SU. (d) Classified predicted maximum landslide area per SU. (d) 95% credible interval estimated with INLA. (e) 95% credible interval estimated via bootstrap.